POLITECNICO DI MILANO
Dottorato di Ricerca in Bioingegneria
Ph.D. in Bioengineering

Susanna Migliori

Patient-specific modelling of stented coronary bifurcations: a validated, OCT-based reconstruction methodology for CFD analyses

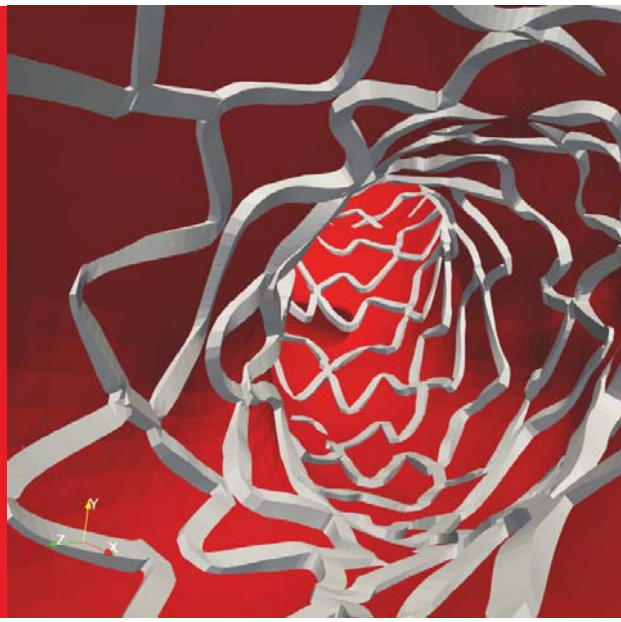

POLITECNICO DI MILANO
Dottorato di Ricerca in Bioingegneria
Ph.D. in Bioengineering

Patient-specific modelling of stented coronary bifurcations: a validated, OCT-based reconstruction methodology for CFD analyses

Susanna Migliori

Supervisor:
Prof. Gabriele Angelo Dubini
Prof. Francesco Migliavacca
Advisor:
Dr. Claudio Chiastra

PhD Coordinator:
Prof. Andrea Aliverti
Tutor:
Prof. Pietro Cerveri

XXXI Cycle
2015-2018

Love is the origin, the source of illimitable energy.
This is for you, my precious life companion.

Susanna

"*Success is the ability to go from one failure to another with no loss of enthusiasm.*"

Winston Churchill

"*Strenuis ardua cedunt.*"

Acknowledgements

I would like to acknowledge my supervisors Francesco Migliavacca and Gabriele Angelo Dubini for supporting my research in these three years. A great thanks to Claudio Chiastra for his important advices. I would like to express my gratitude also to Silvia De Francesco, Marco Bologna, Eros Montin and Luca Mainardi for their supportive collaboration. I would like to acknowledge Caterina Credi, Marinella Levi and Roberto Fedele for their availability and important collaboration. A very special thanks is for Cristina Aurigemma, Lorenzo Genuardi and Francesco Burzotta for their crucial and passionate work.

I would like to express my appreciation for the inspiring collaborative work with Rajiv Rampat. The close collaboration with a cardiologist and the correlative research field was a fruitful experience.

My deepest gratitude is for the coordinators of the VPH-CaSE European project, Karen El-Arifi, Andew Narracott and John Fenner for their great job and endeavours in creating such a great experience during these three years. I would like to thank them also for hosting and supporting me during my secondment. A sincere acknowledge is for Julian Gunn and Paul Morris for their supportive collaboration.

I would like to thank Vanessa Diaz for hosting me during my secondment and for her inspiring words. I appreciate the time spent collaborating with Mirko Bonfanti, who seeks always the best solutions.

Susanna

Abstract

The clinical challenge of percutaneous coronary interventions (PCI) is highly dependent on the recognition of the coronary anatomy that features each individual. The classic imaging modality used for PCI is angiography, but advanced imaging techniques that are regularly performed during PCI, like optical coherence tomography (OCT), may provide detailed knowledge of the pre-intervention vessel anatomy as well as the post-procedural assessment of the specific stent-to-vessel interactions. Computational fluid dynamics (CFD) is an emerging investigation field in the setting of optimization of PCI results. In this study, an OCT-based reconstruction methodology of patient-specific coronary artery models, which include the actual geometry of the implanted stent, was developed for the execution of CFD simulations.

The method was developed and validated by means of a rigid phantom that resembled a segment of the left anterior descending coronary artery where a stent was deployed. The methodology comprised the processing of OCT images to retrieve the lumen contour and the stent, then the three-dimensional (3D) reconstruction was achieved by means of a computer-aided design software. The 3D reconstruction of the stented phantom was assessed with the geometry that was obtained from X-ray computed micro tomography scan, used as ground truth. Results reported twist and distortions that were due to the catheter-based imaging technique, these were reduced with the centreline of one side branch that was chosen as reference for the error angle estimation. The 3D reconstruction was successfully used to perform CFD analyses, demonstrating a great potential for patient-specific investigations.

The developed methodology was employed to perform CFD simulations of blood flow across patient-specific coronary arteries with bifurcations after stent deployment. The developed framework was employed to study the post-operative hemodynamics of sixteen patients. Among those a subset of twelve cases underwent OCT acquisitions after 9-months from the intervention. Such images were used to compute the percentage of restenosis area at the scaffolded segment, which was then compared with the distribution of superficial hemodynamics quantities. The superficial distribution of relative residence time showed similarities with the 2D map of the distance between lumen contours at follow-up and baseline. Such findings were in agreement with the literature, which supported the potential application in cardiovascular intervention. Objectives for future work can be a punctual comparison between fluid dynamics superficial quantities and neointima thickening, enabling for a quantitative study.

Glossary of Acronyms

0D	Zero-dimensional
3D	Three-dimensional
AV	Atrio-ventricular
BMS	Bare metal stents
BRS	Bioresorbable scaffolds
CABP	Coronary artery bypass
CAC	Coronary artery calcifications
CAD	Computer-aided design
CAU	Caudal angle
CFD	Computational fluid dynamics
CHD	Coronary heart disease
CRA	Cranial angle
DES	Drug-eluting stents
DICOM	Digital Imaging and Communications in Medicine
EBC	European Bifurcation Club
EC	Endothelial cell
ECG	Electrocardiography
FD	Frequency domain
FN	False negative
FP	False positives
HK	Huo-Kassab
KISSS	Keep it simple, swift and safe
ISR	In-stent restenosis
IVUS	Intravascular ultrasound
IVUS-VH	Intravascular ultrasound-virtual histology
IVOCT	Intravascular OCT
IWG-IVOCT	International Working Group IVOCT
LAD	Left anterior descending
LAO	Left anterior oblique angle

LCA	Left coronary artery
LCx	Left circumflex
LDL	Low density lipoprotein
LMCA	Left main coronary artery
LOA	Length of apposition
μCT	Micro Computed Tomography
MADS	Main, Across, Distal, Side
MBD	Main branch distal
NIH	Neointima hyperplasia
NIT	Neointima thickening
MBP	Main branch proximal
OCT	Optical coherence tomography
OSI	Oscillatory shear index
PCI	Percutaneous coronary intervention
PLLA	Polylactic acid
POT	Proximal optimisation technique
QCA	Quantitative coronary angiography
RAO	Right anterior oblique angle
RCA	Right coronary artery
RRT	Relative residence time
SB	Side branch
STL	Stereo-lithography
TAWSS	Time-averaged wall shear stress
TD	Time domain
TN	True negatives
TP	True positives
WSS	Wall shear stress

Contents

Chapter 1

Prelude

This chapter provides an opening to the dissertation by presenting the motivation of the research work and the contribution to the state-of-the-art in cardiovascular simulations. The context of the work is introduced through a brief description of the pathology of the coronary arteries and some of the most applied treatment techniques. Therefore, the research question is declared with a focus on the contribution provided to the state-of-the-art. Finally, the content of the dissertation is presented with a summary of each chapter.

This chapter is partially reported in the paper Chiastra C., **Migliori S.**, et al. (Chiastra et al., 2017a) that was published in the Journal of Cardiovascular Translations of Research.

1.1 Introduction and motivation of the study

THE incidence rate of death related to coronary heart disease (CHD) motivates the leadership as the major cause of death in Western Countries (Mozaffarian et al., 2016; Puddu and Menotti, 2016). Principal source of CHD is the narrowing of vessel lumen due to atherosclerotic plaque development. The most widely performed CHD surgical treatment is percutaneous coronary intervention (PCI) due to the reduced hospitalisation, recovery time and costs (Mozaffarian et al., 2016).

The significant anatomic variability observed among individuals has led to an increased interest in the application of intravascular imaging techniques for the characterisation of each specific clinical case. The works of Mintz and colleagues (Mintz, 2015) and Madhavan and co-authors (Madhavan et al., 2014) reported that intravascular images studies are crucial in the understanding of plaque composition and extension, as well as adverse events including in-stent restenosis (ISR) and stent thrombosis.

PCI procedures are mainly guided by X-ray angiography and intravascular imaging. Essentially, the former enables an interventionist to monitor the procedure. It employs X-rays to obtain gray-scale images of the blood vessels where a radio-opaque liquid flows. Whereas, intravascular imaging modalities involve the delivery of a probe in the cardiovascular circulation to the treated vessel and, then, the vessel lumen is imaged. The most spread catheter based imaging modalities during PCI are intravascular ultrasound (IVUS) and optical coherence tomography (OCT). The former employs ultrasound waves to distinguish the arterial wall layers, whereas the latter ensures higher image resolution by using light with a bandwidth within the near-infrared spectrum. OCT axial resolution ranges from 12 to 18 μm (against 150 to 200 μm of IVUS) and lateral resolution ranges from 20 to 90 μm (against 150 to 300 μm of IVUS) (Bezerra et al., 2009).

Therefore, the introduction of OCT in intervention cardiology procedures allows for the emulation of the actual anatomic environment of the blood vessel inside with the implanted scaffold. Several works in the literature have proposed methods that use intravascular imaging techniques to automatically reconstruct the lumen inside with the implanted scaffold (Brezinski et al., 1996; Tearney et al., 1997; Tenekecioglu et al., 2017a). The motivation and context of the accomplished research work are declared to the reader by citing the main remarks of selected journal papers.

Intravascular OCT was introduced in 1997 (Tearney et al., 1997) and immediately proved great potentiality to become the most applied imaging modality

in cardiovascular intervention and diagnostics. Indeed, Prati and co-authors in (Prati et al., 2011) reported that the first ex-vivo studies showed that such intra-vascular imaging technique enabled to visualise the internal arterial micro structure by means of a probe (Brezinski et al., 1996). These results built the way for the application of OCT to human patients (Jang et al., 2002, 2001).
Tenekecioglu and co-workers (Tenekecioglu et al., 2017a) reviewed the application of available OCT image processing strategies in clinical practice and in the scientific research. Due to the achievable near histological resolution, OCT enabled the characterisation of the vessel wall and plaque composition. Thus, fibrous component and calcifications are recognisable in the images obtained during the acquisition as a result of the different optical properties of such media. Furthermore, the excellent image quality enabled to evaluate the intervention outcomes after stent insertion. For instance, the residual stenosis area could be computed as a percentage of the lumen area out of the scaffold. The interaction between the stent struts and the vessel wall could be evaluated through the embedment analysis. Essentially, the degree of embedment was estimated from the distance between the midpoint of the innermost strut surface and the lumen contour. An additional relevant aspect was the tissue prolapse, tissue protrusion between adjacent struts, common in case of lipids rich plaques. Evidences that has been reported in the literature, support the connection between lesion induced by stent implantation and wall shear stress (WSS) with neointimal proliferation. The development of automatic and robust image segmentation algorithms and computational models for the simulation of blood flow, had extended the application of OCT to the assembling of detailed 3D geometries for the study of local hemodynamics. A limitation of this intravascular imaging modality was the low penetration depth, 2-3 mm, respect to IVUS 8-10 mm. This last was also applied as IVUS-virtual histology (IVUS-VH), that relies on the elaboration of the signal to build tissue maps and plaque classification. An advanced diagnostic technique comprises the co-registration between IVUS-VH and OCT, taking the advantage of the strength of both technologies.
Zaromytidou and co-authors (Zaromytidou et al., 2016) presented an overview of the implication of the available techniques for the assembling of patient-specific coronary artery geometries in the study of hemodynamics. The co-registration of IVUS or OCT and X-ray angiography was implemented by imaging the same coronary segment. Therefore, the centerline method, that was the definition of a 3D vessel centerline from two angiography projections, led to a vessel 3D reconstruction. The following step was the evaluation of WSS along a lesion. With this purpose, the coronary blood flow was calculated from

the time required by the contrast liquid to overpass the vessel or through the usage of Doppler velocity measurements. Alternatively, the reconstruction might be achieved only by the biplane angiography, that was the 3D quantitative coronary angiography (QCA). Toutouzas and colleagues (Toutouzas et al., 2015) described a methodology to achieve geometrically correct lumen geometries that employed OCT image set with biplane angiography, that was named 3D OCT. Results were compared with 3D IVUS, performed with IVUSAngioTool (IVUSAngioTool 2.1, Thessaloniki, Greece, http:// mklab.iti.gr/ivus), and 3D QCA, applied by means of QAngio XA 3D RE (Medis Specials bv, Leiden, the Netherlands), both via morphologic and hemodynamics metrics, to quantify the intra- and inter-observer agreement values. Overall, 3D OCT exhibited the highest consistency among the lumen reconstructions, supporting the robustness of the methodology and by providing a clear picture of the plaque composition.

In the last years the work of many research groups has been focused on the development of anatomically correct and accurate reconstruction methodologies for the simulation of blood flow in treated coronary arteries. Highly performing algorithms for the processing of OCT images provide lumen contour and stent struts. The works of Wang and colleagues (Wang et al., 2013, 2014) are commonly used as reference for the definition of image segmentation approaches that seek to automatically identify the lumen contour and the stent, both as metallic and polymeric designs. Briefly, the pixel intensity is considered for the classification in either background or candidate for lumen and stent. Besides, particular image features are taken into account to gradually refine the previous classification. Although the high reliability of such algorithms, in some cases a manual correction of the identified components is necessary because of artefacts during the acquisition, such as light reflections at blood cells. The coupling between OCT, as well as IVUS, and angiography leads to the creation of anatomically correct vessel reconstructions. Indeed, angiography images picture the coronary arteries at different projections and, then, they can be applied to achieve the vessel three-dimensional shape. Bourantas and colleagues (Bourantas et al., 2013) have proposed a methodology to elaborate angiography projections to obtain the vessel 3D centerline. Since coronary arteries deform during the heart beating cycle and respiratory movements, the centerline methodology implies end-diastolic angiograms, selected at each of the two projections. Hence, the two in-plane centerlines are combined to create a unique 3D vessel centerline along which lumen contour and stent are aligned (Çimen et al., 2016). Ellwein and co-authors (Ellwein et al., 2011) have described a technique to achieve the 3D OCT catheter pull-back

pathway. Essentially, the problem is addressed as an optimisation approach by minimising the bending energy of the possible pathways in the lumen area. Such strategy enables to resemble the actual acquisition procedure by aligning lumen contour and stent on the catheter, indeed the vessel inside is imaged perpendicularly to the OCT probe. Finally, such vessel 3D geometries can be used to perform computational fluid dynamic (CFD) simulations, as mentioned by Tenekecioglu and co-workers in (Tenekecioglu et al., 2017a) and by Toutouzas and colleagues in (Toutouzas et al., 2015).
The interest within the research community in this topic is increasing, however, the literature lacks of exhaustive analyses about coherence with actual lumen and stent geometries. This dissertation, as well as in the studies by Chiastra et al. (Chiastra et al., 2013a) and OBrien et al. (OBrien et al., 2016), propose a framework for the reconstruction of 3D artery geometries including the implanted stent starting from OCT images for the execution of CFD simulations. Specifically, in this thesis the stent geometry was preserved through the usage of the implanted device skeleton for a morphing procedure, enabling for the definition of the stent configuration where the position of stent struts was unknown due to light reflection on the OCT guide-wire. The described methodology is featured by a quantitative validation that proved satisfactory accuracy. Therefore, the accomplished research work represents an important contribution for the development of a reliable reconstruction tool for the evaluation of altered hemodynamics following stent deployment.

1.2 Aims and objectives

This dissertation presents a framework for the execution of CFD simulations on patient-specific coronary artery models, which includes the actual geometry of the implanted stent. This involves the application of an OCT-based reconstruction methodology that was developed and validated by means of a rigid phantom which resembled a representative geometry of a human left anterior descending (LAD) coronary artery with bifurcations. In particular, this last was imaged with OCT, angiography and micro-computed tomography (μCT). The acquired OCT images were segmented to identify lumen contour and stent struts. These components were aligned and orientated with the centerline of the phantom 3D reconstruction that was built from X-ray μCT scan. The accuracy of the reconstruction method was evaluated in both the image segmentation and the alignment/orientation processes. The former was validated against manual segmentation of OCT images where two image

readers identified the region of interest for the lumen and the stent. The latter was assessed by comparing the outcomes obtained for the lumen and the stent respectively with the reconstruction from μCT scan. The achieved high fidelity 3D geometry was used to perform a proof-of-concept CFD simulation fulfilled with a commercial software.
Therefore, the developed methodology was employed to perform CFD simulations of the blood flow across patient-specific coronary arteries with bifurcations after stent deployment. Such studies were performed in collaboration with academic and clinical Institutions, as partners of the VPH-Cardiovascular Simulation and Experimentation (VPH-CaSE) MSCA-ITN-2014 European Training Network. In particular, the elaborated OCT and angiography images were provided by the Institute of Cardiology, Catholic University of the Sacred Heart (Rome, Italy), by Brighton and Sussex University Hospitals (Brighton, UK) and by Northern General Hospital, Sheffield Teaching Hospitals NHS Foundation Trust.

The main objectives of the study were:

- Improve an algorithm for the segmentation of in-vivo OCT images and for the developed framework;
- Implement a strategy for the creation of the vessel and the stent 3D geometries from the segmentation outputs;
- Validate the accuracy of the developed reconstruction methodology;
- Process in-vivo medical images, angiograms and OCT images, that were acquired by the collaborating cardiologists to obtain patient-specific coronary 3D reconstructions;
- Simulate patients' hemodynamics in the reconstructed coronary artery segments with bifurcations by means of a computational fluid dynamic software;
- Process the results to analyse the effects of the implanted stent on the local blood flow distribution.

1.3 Summary

Chapter 2 introduces the clinical motivation of the fulfilled research work by providing to the reader an overview of the coronary tree anatomy, with atherosclerotic pathology genesis and the main consequences. As the work here reported has an application to coronary bifurcations, a brief insight of the classification accepted by the European Bifurcation Club for the different bifurcation lesions and treatment strategies are described. Additional information about single stent coronary interventions is provided, as these are the resembled scenarios. The second part of the Chapter moves the reader closer to the topic of the dissertation. The information reported seeks to present the challenges of this research field, the novelty of the developed methodology and the implications to intervention cardiology. This Chapter describes the imaging modalities that are mostly employed during the interventions, focusing on angiography and OCT. The fluid dynamic mathematical formulations implemented for simulating the blood flow are described, alongside the quantities that are commonly considered as descriptors for hemodynamic conditions. Finally, the state-of-the-art in patient-specific modelling is briefly introduced.

Chapter 3 presents the developed OCT-based reconstruction methodology and the validation procedure. A typical geometry of a human coronary segment with bifurcations was resembled as a rigid phantom. A metallic stent was deployed in the phantom, then it was imaged with OCT and μCT. This latter provided a reference geometry for validation purposes. A proof-of-concept CFD simulation was performed using the achieved reconstruction.

Chapter 4 reports the application of the validated OCT-based methodology to in-vivo medical images that were acquired at the Institute of Cardiology, Catholic University of the Sacred Heart of Rome (Italy). Three patients' angiograms and OCT images were processed to achieve high fidelity 3D geometries of the stented coronary artery segments with bifurcations. Patient-specific CFD simulations were carried out and results were processed for the characterisation of the disrupted hemodynamics after stent implantation. An uncertainty study on CFD boundary conditions was performed on one case and the results were processed to quantify the effects on the distribution of wall shear stress along the geometry. Moreover, the chapter describes the collaborative work that was performed with partners from the University of Sheffield as part of the European Marie-Skłodowska Curie Innovative Training Network, Virtual Physiological Human-Cardiovascular Simulation and Experimentation (VPH-CaSE). A patient was found with an occlusion at the left main coronary artery bifurcation and underwent PCI procedure with

the implantation of one stent. The resultant hemodynamics was analysed with a CFD simulation.

Chapter 5 includes the elaboration of pre-operative OCT images for the simulation of highly disrupted blood flow in a coronary artery with spontaneous dissection. This last resulted in the generation of an empty chamber into the vessel wall. The developed reconstruction methodology was employed to achieve the geometry of a right coronary artery segment with bifurcations where an ulcerated plaque was found. Patient-specific CFD simulation revealed heavy flow recirculation in the empty plaque and at the interface with the normal lumen.

Chapter 6 presents the application of the validated OCT-based reconstruction method for patients treated with a polymeric bioresorbable scaffold at the Sussex Cardiac Centre, Brighton and Sussex University Hospitals, Brighton, UK. The elaborated data were acquired during a clinical trial whose objectives were the evaluation of Absorb BVS stent (Abbott Vascular, Abbott Park, IL, USA) at coronary bifurcations. It included the acquisition of intravascular OCT images at baseline, after 9 and 18 months from the intervention. Patient-specific CFD simulations were carried out and the blood flow was characterised in terms of wall shear stress. The OCT images at 9-months follow-up were elaborated to evaluate the neointima thickening which was presented in terms of restenosis area percentages. These last were compared with results from CFD simulations seeking to investigate any relationship between blood flow and vessel remodelling.

Chapter 2

Coronary artery diseases and medical imaging techniques for patient-specific CFD simulations

This Chapter introduces the clinical motivation of the fulfilled research work by providing to the reader an overview of the coronary tree anatomy, with atherosclerotic pathology genesis and the main consequences. Moreover, this Chapter introduces the imaging modalities that are mostly employed during percutaneous coronary intervention, focusing on angiography and OCT. The implemented fluid dynamic mathematical formulations for simulating the blood flow are here described, as well as the quantities that are commonly considered as descriptors for hemodynamic conditions. Finally, the state-of-the-art in patient-specific modelling is presented.

This chapter is partially reported in the paper Montin E., **Migliori S.**, et al. (Montin et al., 2016) that was published in the Proceedings of the Annual International Conference of the IEEE Engineering in Medicine and Biology Society, Scopus.

2.1 The cardiovascular circulation and the coronary artery tree

THE cardiovascular system is a network of blood vessels that delivers oxygen, nutrients, hormones and other substances to the body tissues and removes waste products. The heart is composed of two main pumps, left and right, that move the blood through two separate circulatory systems. In particular, the right heart pumps the blood to the lungs, whereas the left heart moves the blood to the systemic circulation. Such circulations are connected to form a continuous flow, the output of one pump becomes the input of the other one. The heart pushes the blood into the arteries that branch into arterioles and smaller vessels until they become capillaries, which size enables for the exchange of substances between the blood and the cellular interstitial space. Then, veins deliver the blood from the capillaries back to the heart. The heart is located between the lungs and above the diaphragm (mediastium) and its structures can be classified according to their function. The heart wall and fibrous skeleton represent a structural support; valves and great vessels enable the circulation of blood throughout the pulmonary and systemic networks; the coronary circulation is responsible for the maintenance of heart cells; lastly, nerves and specialised muscle cells regulate the stimulation and control of heart action, that is the contraction of the cardiac muscle (myocardium). The heart is comprised of four chambers (i.e right and left atria, right and left ventricles) that are coupled to form two pumps in series, which work at different pressure levels. The right heart pumps the blood into the pulmonary circulation and works at low pressure (i.e. low-pressure system), peak pressure about 25 mmHg (Feher, 2017), whereas the left heart is a high-pressure system as it pumps blood into the systemic circulation, peak pressure about 120 mmHg (Feher, 2017).
The atria are smaller than the ventricles and store the blood until they are emptied into the ventricles. On the other hand, these last have a thicker myocardial layer that propel blood into the pulmonary or systemic circulation. The blood is pumped from the heart by means of a cyclic alternation of ventricular contraction (i.e. systole) and relaxation (i.e. diastole), called cardiac cycle. The main phases of the cardiac cycle are: *i)* ventricular diastole or atrial systole, the mitral and tricuspid valves open in order to fill the ventricle; *ii)* isovolumetric ventricular systole, both the atrio-ventricular (AV) and semilunar valves are closed, that result in an increase of the intra-ventricular pressure; *iii)* blood ejection from the ventricles, the semilunar valves open as the ventricular pressure slightly exceeds the pulmonary artery and aortic pressure; *iv)* isovolumetric ventricular diastole, the ventricles relax while both the AV and semilunar

valves are closed; *v)* passive ventricular filling, the AV valves passively open as the intra-ventricular pressure falls below the atrial pressure (McCance and Huether, 2015). The coronary circulation (Fig. 2.1) belongs to the systemic circulation and its main role is the myocardium perfusion. The coronary arteries receive blood from the aorta by the coronary ostia, whereas the coronary veins empty into the right atrium through the coronary sinus. An optimal distribution of blood is fundamental to guarantee that oxygen and nutrients reach the heart muscle at proper concentrations to satisfy the regular requirements of the cardiac tissue.

The coronary artery tree comprises two main branches: the right coronary artery (RCA) and the left coronary artery (LCA). Both of those derive from the aortic root, respectively from the right and the left auricular appendix, and vascularise the cardiac tissue that belong to the two main chambers of the heart. The former perfuses also the electric conduction system of the heart and a portion of the left ventricle by means of several side branches. Whereas, the latter bifurcates in left anterior descending (LAD) and left circumflex (LCx) arteries. These last, through successive bifurcations, provide blood also to the interventricular septum (Drake et al., 2012).

The collateral arteries are connections between branches of the same coronary artery or between RCA and LCA. The collateral circulation is important to protect the heart from ischemia when the major coronary arteries are partially occluded and limited amount of blood reaches the downstream cardiac tissue. In general, two processes trigger the growth of new collateral vessels: arteriogenesis, when new vessels generate from pre-existing arteries; angiogenesis, when new capillaries grow within a tissue. The partial occlusion of blood vessels result in an increase of blood flow velocity, therefore of shear stress. This represents a stimulus to collateral growth by the activation of the endothelium and by the production of growth factors (McCance and Huether, 2015). The wall of blood vessels is composed of three main layers: tunica intima (the innermost layer), tunica media (medial layer) and tunica adventitia (the outermost layer). The tunica intima includes a cellular layer, endothelium, that accomplishes several functions through the release of vasoactive chemicals and actively responds to blood flow. The tunica media presents a layer of smooth muscles and elastic fibres. Lastly, the tunica adventitia is an active layer of connective tissue with nerves and lymphatic vessels. The thickness and absence of one or more of those layers features the total thickness of the blood vessel wall.

In general, geometrical features of the coronary arteries vary between individuals. Dodge Jr. and co-workers (Dodge et al., 1992) measured the lumen diameters at specific points in the coronary tree of patients with no evidence of

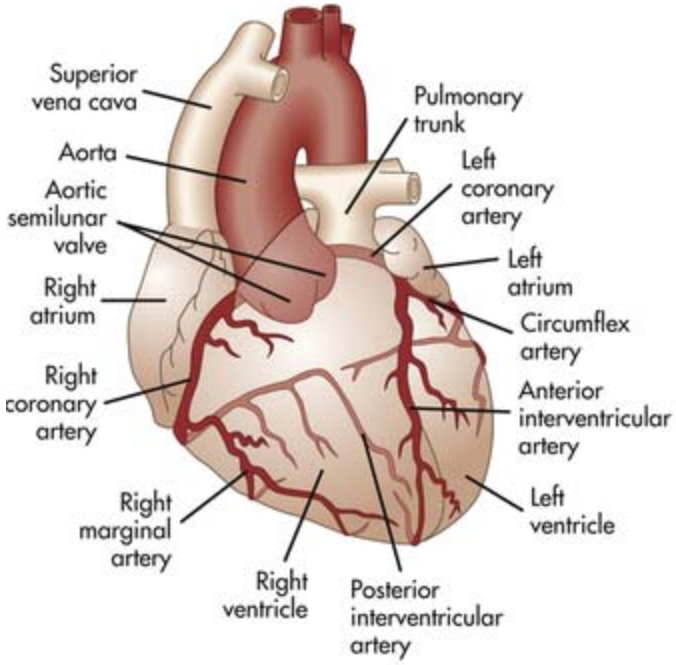

Figure 2.1 Coronary circulation (McCance and Huether, 2015). *Reprinted from Pathophysiology-E-Book: The Biologic Basis for Disease in Adults and Children, 7th edition.* © *2015 Elsevier Elsevier Health Sciences.*

atherosclerotic disease. The obtained values for the diameters of RCA, left main coronary artery (LMCA), LAD and LCx respectively were 3.0±0.5 mm, 4.4± 0.4 mm, 3.0± 0.4 mm and 3.4±0.5 mm.

The blood flow at rest is about 225 ml min^{-1}, that corresponds to 4%-5% of the overall cardiac output (Hall, 2015). Coronary arteries branch in gradually smaller vessels until they penetrate the epicardium (the outermost layer of the cardiac wall) to perfuse the myocardium. Such strong connection between the coronary arteries and the cardiac tissue induces the blockage of coronary blood flow during systole, as the arteries are compressed and twisted by the ventricular muscles. Therefore, the perfusion occurs mainly during the diastole, namely diastolic flow. The phase changes during the cardiac cycle are more relevant for the left ventricle than the right ventricle, which is correlated to the degree of muscular contraction. Davies and co-workers (Davies et al., 2006) modelled the propagation of blood in the coronary circulation by means of wave intensity analysis. Fig. 2.2 shows the pressure and flow velocity measurements that were performed simultaneously with two catheters inserted at proximal LCx of 20 subjects. The obtained values were used to compute the intensity of waves

originating from the proximal end (positive semiplane) and distal end (negative semiplane) of the artery. The same wave pattern was found, that included six predominant waves, whereas differing in intensity and timing between subjects. This study succeeded to quantify the pressure-velocity wave. Moreover, it revealed that the ”suction” wave, that originates from ventricular relaxation and propagates backwards, is the leading wave for the generation of coronary blood flow.

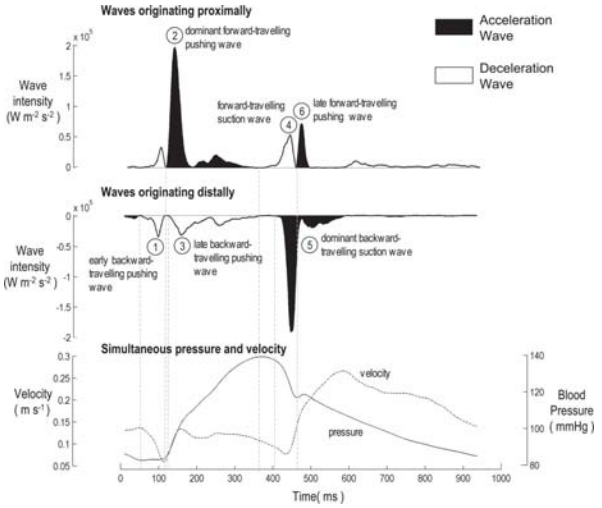

Figure 2.2 Intensity waves of the coronary blood flow. *Adapted with permission from Circulation, Vol.113(4): 1768-1778. J.E Davies et al., Evidence of a dominant backward-propagating ”suction” wave responsible for diastolic coronary filling in humans, attenuated in left ventricular hypertrophy © 2006 American Heart Association, Inc.*

2.2 Coronary artery disease as a reaction to intravascular hemodynamics

Coronary artery disease (CAD) is the predominant cause of death in Western Countries (Mozaffarian et al., 2016; Puddu and Menotti, 2016) and atherosclerosis is one of the major source of CAD. This last is an inflammatory disease that develops and progresses with large concentration of plasma cholesterol. The lesions are triggered by injury of the endothelium, which dysfunction and inflammation lead to pathological events that cause the generation of a plaque. In particular, low density lipoprotein (LDL) penetrates into the subintima of arterial walls, where it is trapped by proteoglycans. Inflammation, oxida-

tive stress, and activation of macrophages induce the oxidation of aggregated LDL. Since the oxidised LDL is toxic to endothelial cells, it is engulfed by macrophages and the resultant cell is called foam cell. Fatty streak results from the accumulation of foam cells in the walls of arteries and trigger inflammation changes towards progressive damage of the vessel wall. Then, smooth muscle cells proliferate and form a fibrous plaque. Unstable and high-risk plaques are prone to rupture and can initiate clotting (Tabas, 2010).

The endothelial response to intracoronary hemodynamics towards pathological events, like atherosclerosis, is well established in the literature through results from both in-vitro and in-vivo studies. Blood flows within the arteries, which anatomical geometry induces complex hemodynamic pattern with variable spatio-temporal features. Among the resultant forces (Fig.2.3a), wall shear stress (WSS) is a tangential force that is due to the friction of the flowing blood on the endothelial surface. The shear stress is proportional to blood viscosity, μ, and the spatial gradient of blood velocity:

$$\tau = \mu \times \frac{dv}{dy} \tag{2.1}$$

where τ is the shear stress, v is the blood velocity and y is the radial axis that is directed perpendicularly to the endothelial surface. In the literature it is argued that the vascular haemostasis is ensured when the WSS values are maintained within certain limits. In general, it is not possible to define a unique range since it varies between individuals and along the cardiovascular circulation itself. Moreover, CAD affects the vascular mechanical responses which might reflect on the mean WSS values (Cheng et al., 2007).

WSS distribution is highly influenced by arterial geometry, such as vessel curvature and bifurcations, that lead modified flow pattern. Wentzel and colleagues (Wentzel et al., 2012) reported that moderate values of WSS (between 1.5 Pa and 3 Pa) can be mainly found in straight arterial segments, with unidirectional flow. High WSS values are larger than 3 Pa, that are generally found at stenotic site with narrowed lumen area. Low WSS, with values below 1 Pa - 1.5 Pa and featured by unidirectional flow, is typical of internal areas of curvatures and downstream of stenotic plaque.

In general, the cut-off points for the WSS intervals listed above vary among species and vascular beds across the cardiovascular system. Velocity measurements, that were acquired in animals, suggested that smaller mean values of WSS are located downstream the artery tree, whereas highest average values are observed in the LAD coronary artery (Cheng et al., 2007). Moreover, values of WSS at one site can oscillate between systole and diastole. Commonly, low time-averaged magnitudes occur downstream the occlusion, whereas high

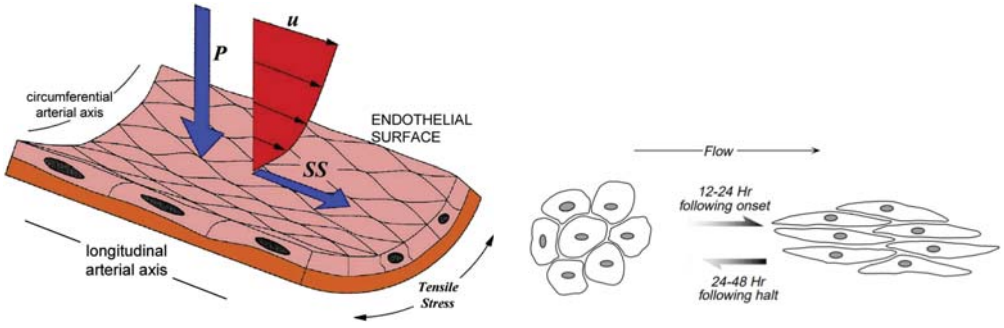

(a) (b)

Figure 2.3 Schematic description of (a) the forces that are generated by the blood flow. Where, *u* is the velocity of the blood, P is pressure on the arterial wall and SS is the shear stress that is applied on the wall. *Adapted with permission from Elsevier B.V., Vol.57(6):389-400. Zaromytidou, M. et al., Intravascular hemodynamics and coronary artery disease: new insights and clinical implications.* © *2016 Hellenic Society of Cardiology. This is an open access article under the CC BY-NC-ND license (http://creativecommons.org/licenses/by- nc-nd/4.0/1. No changes were made to the picture.* (b) of the morphological alteration under an equivalent shear stress of 0.8-1 Pa *Adapted with permission from Jama, Vol. 282(21):2035-2042. Malek, A. M. et al. Hemodynamic shear stress and its role in atherosclerosis.* © *1996 Jama. No changes were made to the picture.*

oscillatory time-averaged WSS (TAWSS) can be found upstream the stenosis. Low and/or oscillatory WSS is commonly associated to the development of atherosclerosis, it is observed at the ostia of branches and downstream of stenotic plaques.

Endothelial cells (ECs) respond to external stimuli that are induced by the hemodynamics (Fig. 2.3b). These cells are arranged to allow for the control of molecules transportation between the vessel lumen and tunica intima. WSS stimuli activate the physical deformation of ECs that under high WSS elongate and align with the flow representing a barrier for molecules, whereas under low WSS the ECs change their structure from fusiform to polygonal shapes facilitating the migration of molecules Fig.2.3b (Zaromytidou et al., 2016). Furthermore, evidences from in-vitro and in-vivo animal studies proved that the mechano-receptors on the surface of ECs are sensitive to the local low WSS and can activate an intracellular cascade that leads to an inflammatory reaction, atherosclerosis (Wentzel et al., 2012). Consequently, the effects of low WSS lead to the remodelling of the arterial wall.

2.3 Treatment for coronary artery disease

As mentioned in the previous section, atherosclerosis may cause stenotic lesions that consist in restriction of the arterial lumen. This results in a reduced blood perfusion to the tissues located downstream, which might lead either to tissue loss, for the systemic circulation, or acute heart failure, for coronary circulation. Atherosclerotic lesions can be treated pharmaceutically when the disease is at an initial status, beside a change in more healthy daily habits. This can significantly slow the progress of the pathology and may reduce the risk of surgical intervention (Mann and Truswell, 2017). In general, the main intervention procedures for coronary revascularisation are coronary artery bypass graft (CABG) and percutaneous coronary intervention (PCI). The former implies the use of blood vessel segments from different locations, such as segments of mammary artery or saphenous vein, to build an alternative path for the blood to reach the downstream tissue. The latter is a non-surgical approach, comprising the widening of the lumen area via the inflation of a balloon (i.e. balloon angioplasty), Fig.2.4, that is often followed by the deployment of a rigid metallic scaffold that maintain the lumen opening. Both the balloon and the stent are delivered to the lesion by a catheter from the femoral artery. The stent is positioned at the lesion and expanded with a balloon that is then deflated and removed, Fig.2.4

PCI procedures have seen remarkable progress since the first successful coronary angioplasty, that was performed in 1977 as reported by Byrne and coauthors in (Byrne et al., 2017). The principle of this technique is the compression and dissection of the atherosclerotic plaque by the inflation of a balloon. The main limitations are caused by acute vessel recoil, constrictive remodelling of the arterial wall and neointima hyperplasia toward the re-narrowing of the arterial lumen. Stent implantation was performed for the first time after PCI in 1986 (Byrne et al., 2017; Sigwart et al., 1987), immediately showing its potentiality as alternative to CABG. The procedure is performed under local anaesthesia as it is non-surgical minimally invasive and the patient recovery time is minimal respect to bypass surgery, thence, the overall costs are reduced to a minimum (Cohen et al., 2014; Magnuson et al., 2012). The main function of an endovascular prosthesis (stent) is the widening of the vessel lumen in order to recover the blood flow. In general, different types of stents and stenting procedures are available. These devices are designed as tubular support structures that can be inserted in percutaneous or transluminal modality through a body passageway. Typically, stents are made from a structure that wraps around at least a portion of a circumference and are adapted to compress and expand be-

tween a smaller and larger diameter. Stents can be self-expandable, so that

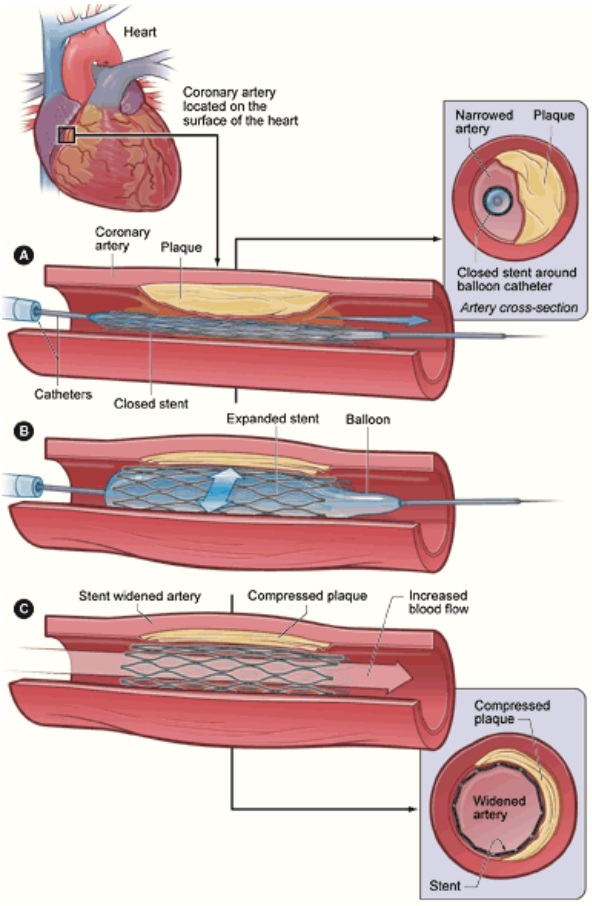

Figure 2.4 Diagram of coronary angioplasty and stent placement. *This image is in a public domain because it contains materials that originally came from the National Institutes of Health.*

they elastically expand out to a present larger diameter, and can be balloon-expandable, in which the stent is deployed by applying a high pressure to the stent inner surface by inflating a balloon. Typically, stents are implanted within an artery or other passageway by positioning the devices within the lumen to be treated and then expanding it from a compressed diameter to an expanded one. Self-expandable stents are one of the most common type of vascular prostheses used in medical procedures, they are increasingly being used because of their adaptability to a variety of different conditions and procedures. These are usually made of shape memory materials that are capable of recovering shape after inelastic deformations. The alloys that are commonly used to manufacture such devices include Nickel-Titanium Alloy (Nitinol) and 304 stainless steel,

as described in Doran et al. (2000). Traditionally, self-expanding stents have been used in areas where the vessel experiences a variety of motion, trauma and tortuosity. Thus, they are commonly applied for peripheral arteries of the vascular system, so that trauma from external sources do not permanently deform the implanted device. It is reported in the literature that the application of such devices for PCI is not the recommended choice because of several drawbacks such as the registered high tendency for neointima hyperplasia.
Balloon-expandable stents are often used to treat stenosis of coronary arteries. Usually, these are made from ductile materials that plastically deform. The most used alloys for metallic stent manufacturing are 316L stainless steel and CoCr. Balloon-expandable stents are more commonly implanted in coronary vessels than in peripheral ones because of their deformable nature and their tendency to be precisely sized to a particular vessel diameter and shape.
Stents may also be used in combination with other components to treat a number of medical conditions. For example, stent-graft assemblies are often used in the treatment of aneurysms, among which popliteal artery aneurysms, by sealing the wall of the blood vessel with impermeable graft material Doran et al. (2000).
Therefore, the material choice for stent manufacturing is important both for the mechanical properties that are provided and for the restenosis rate derived from the stent insertion. In addition, the stent strut surface may be treated with electropolishing and passive coating in order to improve the biocompatibility of the device. In particular, the superficial coating aims to reduce the incidence of neointimal hyperplasia, which is the growing of smooth cells on the stent struts and lumen re-narrowing, named in-stent restenosis (ISR) (Kim and Dean, 2011). That category of devices is called drug-eluting stents (DES), where the surfaces are treated with active pharmaceutical ingredients to reduce the neointima growth. On the other hand, metallic stents that do not receive such superficial treatment are named bare metal stents (BMS).
Moreover, a recent development in stent manufacturing has led to the introduction of bioresorbable scaffolds (BRS) that dissolve in the vessel wall after recovering the lumen passageway. These are manufactured in magnesium alloys or in poly-L-lactic acid (PLLA) and are expected to overcome the limitations of BMS and DES. The devices that have received approval for marketing by the European Commission since January 2017 are Absorb BVS (Abbott Vascular, Abbott Park, IL, USA), DESolve (Elixir medical corporation), ART Pure Bioresorbable Scaffold and Magmaris (Biotronik) (Sotomi et al., 2017). The degradation rate of BRS allows for the remodelling of the arterial wall on the scaffold during the first year of vessel remodelling period, while recovering the elastic-

ity and mechanical properties of the vessel wall once the scaffold is absorbed during the two years following the implantation. Therefore, the incidence of adverse events, such as ISR, that are induced by inflammation is significantly reduced. The limitations of BRS are mainly due to the mechanical properties of the manufacturing material, that result in thicker struts compared to DES and BMS to achieve an adequate radial strength, and limited radio-opacity, that reduces the visibility with X-rays. Moreover, the largest randomised trial with BRS, ABSORB III, reported long term failures due to late thrombosis events that were found to be twice that of the metallic scaffolds. The causes are not completely known, however, it is argued that they can be related to lower radial strength, bigger struts and non-uniform scaffold integrity during the polymer degradation period. As a consequence, Absorb BVS devices have been removed from the market and are currently used only for clinical trial (Sotomi et al., 2017).

2.3.1 PCI techniques for coronary bifurcations.

As mentioned in Chapter 1, successive bifurcations enable the coronary arteries to reach the entire surface of the myocardium. Generally speaking, the flow of a fluid in a pipe is affected by its geometry, such as curvature and change of cross section area (White and Frangos, 2007). For instance, the separation of a tube into two daughter branches induces regions of disturbed flow pattern, featured by recirculation and stagnation of the fluid at the tube wall, and discontinuous flow velocity. For this phenomenon, the endothelium is subjected to disturbed WSS and it is prone to plaque formation in such zones, that can appear in the parent branch as well as in the side branches, and the treatment approach is chosen according to the extension of the lesion.
A classification was introduced in 2006 by Medina and colleagues ((Medina et al., 2006)) and it is traditionally used to describe coronary bifurcation pathologies. In particular, the classification is based on the extension of a lesion that is indicated with a binary value, the presence of the lesion is reported with a 1 whereas a branch that is free from plaque is depicted with a 0. The lesions considered in the classification are stenoses that occlude the passageway for minimum the 50% of the lumen area and the codification is done by three digits, one for each branch, separated by a comma. In Fig.2.5 are reported the seven possible classifications of a bifurcation comprising three components, respectively, the parent branch, or proximal main branch (PMB), the daughter branch with the larger diameter, or distal main branch (DMB), and the second daughter branch, or side branch (SB). This is a schematic and simple way to distinguish

bifurcation diseases, however, it fails to classify more complex plaque distribution and composition, for instance, a branch with a lesion below 50% is classified as lesion-free and calcifications are not considered (Louvard et al., 2010). The large variety of coronary bifurcation anatomy and disease distribution jus-

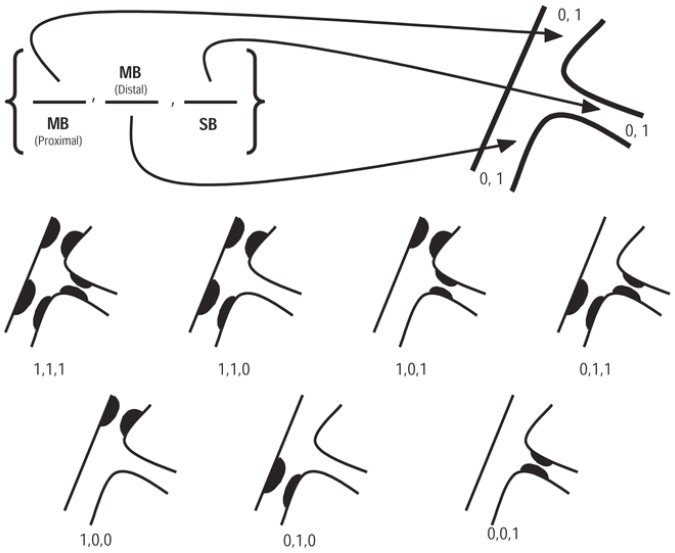

Figure 2.5 Medina classification of bifurcation diseases. *Reprinted with permission from EuroIntervention, Vol. 6 (Suppl J): J31-J35. Y. Louvard et al. Definition and classification of bifurcation lesions and treatments.* © *2010 Europa Digital & Publishing.*

tifies the absence of a unique strategy to treat atherosclerotic lesions. Scientists that are actively interested in the clinical and technical aspects of such pathology created an independent organisation in 2004, named European Bifurcation Club (EBC), which aims to encourage the exchange of ideas and experiences. EBC hosts an annual meeting with the participation of physicians, engineers, biologists, epidemiologists and statisticians for detailed discussions about the management of coronary bifurcation lesions. The main remarks are recorded in a consensus statement, for instance, the document produced by Lassen and coauthors (Lassen et al., 2016) summarises the activity fulfilled in the first decade of EBC. The Medina classification described above (Fig.2.5) was accepted by the EBC alongside an accurate classification of the intervention techniques applied in bifurcation stenting that are divided in classes according to common features, as displayed in Fig.2.6, at the first biennium of the organisation. In particular, each group is defined by the number of implanted stents and the order of implantation.

Based on the clinical experience, EBC consensi also propose guidelines that

support the Main, Across, Distal, Side classification (MADS) that groups the stenting procedures in four classes based on the order of stent implantation: Main proximal first, main Across side first, Distal first and Side branch first.
As an example, it is argued that the dimension of SB should be considered as an indication of the advantages in bifurcation stenting. As a general rule, the formula proposed by Murray (Murray, 1926), Finet (Finet et al., 2008) and Huo-Kassab (HK) (Huo et al., 2009) are recommended as references to evaluate the branch size relation for planning the intervention. These are mathematical formulations of the relationship between diameters that optimise the energy required for the blood to flow across the coronary and represent an application of the fractal theory. Therefore, from experimental evidences, such formula are:

- Murray's law: $D_m^3 = D_{d1}^3 + D_{d2}^3$
- HK model: $D_m^{7/3} = D_{d1}^{7/3} + D_{d2}^{7/3}$
- Finet's relation: $D_m = 0.678(D_{d1} + D_{d2})$

where, D_m is the diameter of the parent vessel, D_{d1} is the diameter of the larger daughter vessel and D_{d2} is the diameter of the smaller daughter vessel.
Furthermore, an effective principle to decide the number of stents to include that has been proposed by EBC is named KISSS, which stands for "Keep it simple, swift and safe".
The provisional technique is a procedure for the insertion of one stent in the main branch at the bifurcation, across the side branch. This procedure is highly recommended for the majority of cases and it is stated that it should be considered as the standard approach for bifurcation stenting. The proposed guidelines suggest to wire the SB if the flow is significantly reduced and its lost can significantly compromise the downstream tissue (Lassen et al., 2016). The proximal optimisation technique (POT) includes the dilatation of the proximal part of the stent by a oversized balloon and it often follows a provisional stenting procedure. In Fig.2.7 the main steps of POT and SB dilatation are displayed. In particular, the main vessel is wired with a scaffold sized according to the distal vessel diameter, then followed by a POT to optimise the intervention outcomes. When the SB is severely compromised, it can be enlarged by inflating two balloon simultaneously, as described in Fig.2.7, so that the achieved main branch dilatation is preserved. This last is called kissing balloon inflation and it was historically considered to restore the bifurcation anatomy when the main branch lumen area is reduced by ballooning the side branch. Nowadays, stents used in clinical practice are mainly classified by their material and design, that have direct impact on the mechanical performances of the device to be used in the

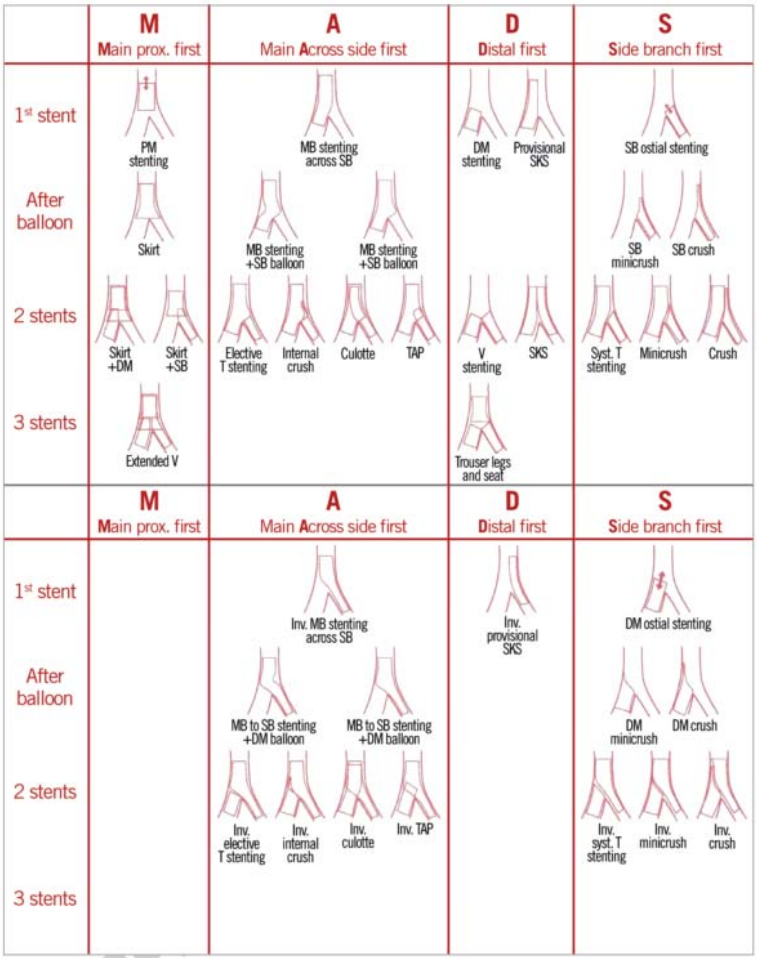

Figure 2.6 MADS classification. *Reprinted with permission from EuroIntervention, Vol. 7(1): 160-163. Y. Louvard and T. Lefvre. Tools and Techniques: PCI in coronary bifurcations lesions.*© *2010 Europa Digital & Publishing.*

chosen intervention technique. For the present dissertation the developed 3D OCT methodology was adopted for the reconstruction of coronary bifurcations that were treated with provisional stenting, eventually followed by POT.
In the following subsection are reported some samples of stents commercially available for the treatment of CHD and with series of Z-shaped structural elements (called ”struts”) joined by connecting elements (called ”bridges”). Among this category are several designs characterised by different struts, bridge shapes and distribution of connecting points. In particular, the bridges either are applied at each inflection point (closed-cell design) or are periodically distributed among the struts (open-cell design), for more details see (Stoeckel et al., 2002). The literature comprehends many works, such as the work of Rieu and

colleagues (Rieu et al., 1999) and the work of Isayama and co-authors (Isayama et al., 2009), where the influence of the cell geometrical features on the device mechanical behaviour is reported. In particular, higher flexibility is associated to open-cell design, whereas closed-cell design provides optimal scaffolding.

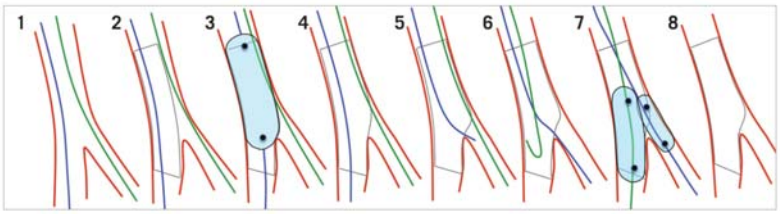

Figure 2.7 Provisional stenting and POT. *Reprinted with permission from EuroIntervention, Vol. 7(1): 160-163. Y. Louvard and T. Lefvre. Tools and Techniques: PCI in coronary bifurcations lesions.* © *2010 Europa Digital & Publishing.*

2.3.2 Designs for metallic and polymeric scaffolds

There is a large variety of stent designs that are currently available in the market, in Fig.2.8 are reported four scaffold families, distinctive for both the device material and geometry. In particular, the first three are pictures of metallic stents and the last device is a polymeric bioresorbable scaffold.

- **Multi-Link 8 and XIENCE**. They are manufactured with cobalt chromium alloy and the design is featured by a sequence of sinusoidal rings that are connected at three points by shaped bridges (Fig.2.8I). The strut has a square cross-section with side length of 81μm, XIENCE solutions have an additional durable polymer-coated layer of 2μm (Byrne et al., 2017) (*www.abbottvascular.com*).

- **SYNERGY**. This type of stenting solution is made of platinum chromium alloy and it is featured by sinusoidal rings with two straight connecting bridges (Fig.2.8II). The strut has a rectangular cross-section with a thickness of 75μm and an additional biodegradable polymer-coated layer.

- **Resolute**. This category is composed of cobalt chromium alloy stents Resolute Integrity and Resolute Onyx, featured by a continuous sinu-

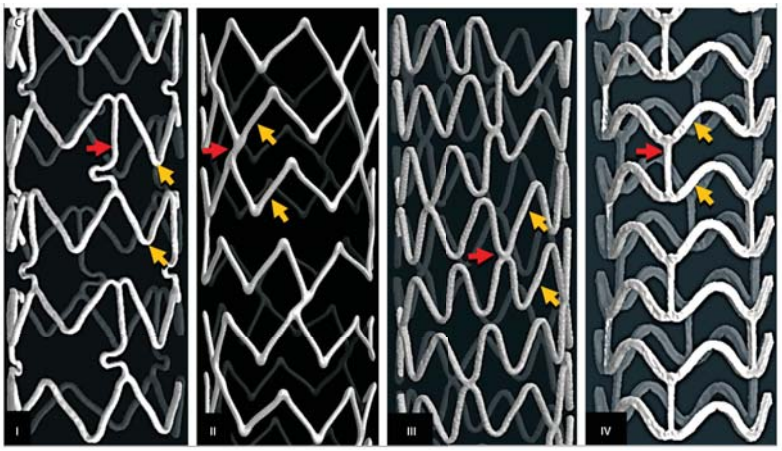

Figure 2.8 Pictures of the main stent design families, respectively metallic (I-III) and polymeric scaffolds (IV). The yellow arrows point the stent rings or helical wire, whereas the red arrows point the connections. (I) Multi-Link 8 (Abbott Vascular) is a cobalt chromium stent, comprising rings that are linked by three bridges. This design is employed for the XIENCE™ family of stents, with additional superficial treatment. (II) The SYNERGY™ (Boston Scientific) is a platinum chromium stent that has sinusoidal rings with two connecting straight struts. (III) Resolute Integrity™ (Medtronic) is a stent made with cobalt chromium alloy and a continuous sinusoidal wire that follows a helical pattern with two or three connection points. (IV) Absorb BVS (Abbott Vascular) is a bioresorbable scaffold made of polylactic acid (PLLA). The design comprises sinusoidal rings that are linked by three straight bridges. *Reprinted with permission from The Lancet, Vol. 90(10096):781-792. Byrne R., et al. Coronary balloon angioplasty, stents, and scaffolds. ©2010 Europa Digital & Publishing.*

soidal wire that follows a helical pattern with two or three connection points (Fig.2.8III). This solution enhances the flexibility of the device without compromising the radial and longitudinal strength. They have a circular cross-section with a diameter if 91μm and a durable polymer-coated layer that limits the incidence of ISR.

- **Absorb BVS**. This is a PLLA bioresorbable scaffold and it includes sinusoidal shaped rings that are connected in three points by straight bridges. The cross-section is rectangular with thickness length of 157μm, which ensures good radial strength for a polymeric device. Results from the study ABSORB III reported long term failures due to late thrombosis events that were found to be twice that of the metallic scaffolds. As a consequence, Absorb BVS devices have been removed from the market

and are currently used only for clinical trial (Sotomi et al., 2017).

2.4 Medical imaging in percutaneous coronary intervention.

Medical imaging modalities are increasingly used to assess the presence and extension of coronary artery disease (CAD) as well as in cardiovascular intervention as they present pictures of the actual anatomy that features each individual (Çimen et al., 2016). The most employed techniques during PCI are X-ray coronary angiography and optical coherence tomography (OCT). The former provides bi-dimensional gray-scale pictures of the coronary tree, therefore, it presents projections of objects that have complex configurations, including different degree of tortuosity and vessel overlapping. Moreover, heart contraction and respiration movements result in time-dependent deformations of the coronary tree. On the other hand, OCT is an intravascular imaging techniques that is used to analyse the blood vessel inside and it provides high resolute pictures of the lumen cross sections. In particular, the high spatial resolution ensures an exhaustive picture of vessel inside both before and after stent deployment (Chatzizisis et al., 2014; Wang et al., 2013). However, OCT outputs do not carry any information about the three dimensional shape of the coronary tree. Thus, angiography images are commonly used in the literature to extract the vessel centreline (Brost et al., 2009; Wang et al., 2013) along which the OCT slices are ideally aligned to reconstruct the coronary 3D geometry.

2.4.1 X-ray coronary angiography: working principles and application

X-ray coronary angiography is a standard imaging modality for the evaluation of atherosclerosis lesions (Brown et al., 2016) and for PCI procedure guidance. The main working principles are in other medical fields and applications. For the purpose of coronary imaging, a X-ray is an electromagnetic radiation that is absorbed by the material it come across, then, it diffuses to the intensifier with a residual energy. The imaging catheter is delivered to the target vessel via either the femoral, radial or brachial artery (Nieman et al., 2001). The coronary tree is visible by means of the injection of a radio-opaque contrast liquid that flows with the blood and gradually dissolves. Therefore, the angiography output is a sequence of gray-scale images where the target blood vessel

appears darker than the surrounding tissue, as reported in Fig.2.9. In Fig.2.10 is a picture of an angiography equipment that comprises a C-shaped arm with a X-ray emitter and an intensifier at its opposite extremities. At the middle way of the C-arm is positioned the patient and the screens display the sequence of the acquired images. Several projections of the treated blood vessel are obtained by moving the C-arm, so that a exhaustive picture of the pathology and treated lesion is provided. The orientations of the acquisition system are defined by the left anterior oblique (LAO), right anterior oblique (RAO) angle, named primary angle, and the cranial (CRA), caudal (CAU) angle, named secondary angle. The primary angle (α), spans from patient's right to left (RAO/LAO) while the secondary angle (β) toward patient's head to feet (CRA/CAU), as reported in Fig.2.11.

A widely confirmed application of the movable C-arm angiography is the acquisition of multiple projections of the same coronary segment, so that an accurate three-dimensional reconstruction can be achieved with a dedicated algorithm that estimates the position of points in the 3D space by correlating planar projections. Heart beating and respiratory movements introduce variability in time and uncertainties in the accuracy of the outcomes. Seeking to neglect the variability due to the heart contraction, acquisitions gated by electrocardiography (ECG) signal are suggested to identify frames that correspond to the same point in the cardiac cycle. Nevertheless, the reconstruction of a 3D point from C-arm images remains an ambiguous problem and it requires accurate information of the projected object in the perspective views (Brost et al., 2009). As a consequence, it is common practice to select a specific angiogram for each image set that corresponds to the peak of diastole (i.e. at the maximum dilatation of the ventricles), when the coronaries are dilated and well visible.

A widely accepted standard diagnostic application of angiography is three-dimensional quantitative coronary analysis (3D QCA). This is performed by the reconstruction of the true geometric shape in space and the creation of an interactive virtual object for the computation of the geometrical quantities of interest. In general, several algorithms have been proposed in the literature to obtain a point in the 3D space from its projections in acquired images (Brost et al., 2009; Dvir et al., 2008; Garcia et al., 2009) and many of them have been implemented in commercial software. In this dissertation the 3D vessel centerlines were extracted with CAAS from PIE Medical. This software reconstructs user defined vessel sub-segments from two angiography projections and is used to perform 3D QCA. It estimates the vessel lumen size across its length (i.e. diameter and area) and, then, reports the occlusion severity and extension. Furthermore, these evaluations can be performed at bifurcations (Fig.2.12), with

the additional information about the relative angle between branches. The limitation of the achieved reconstructions is due to the low resolution of angiography, especially compared with OCT, and the non-physiological lumen area since the coronaries eventually experience either constriction as a reaction to the flowing contrast liquid or enlargement that is pharmacologically induced during PCI.

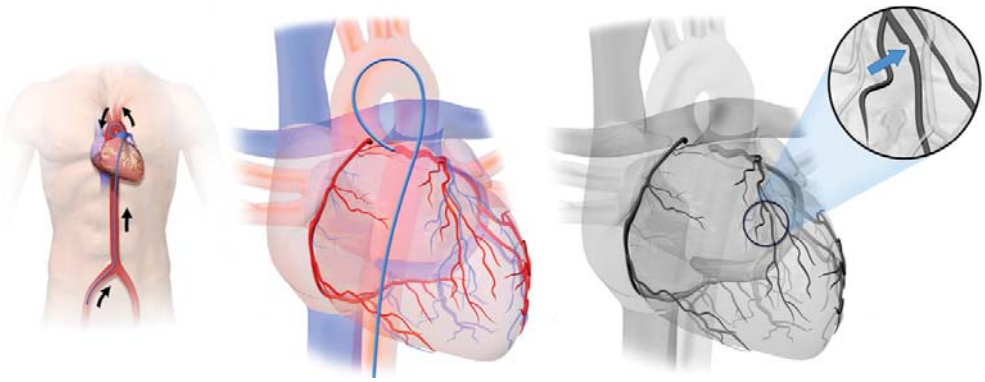

Figure 2.9 Coronary angiography. © Picture by Bruce Blaus. No changes were made to the picture, CC BY-SA 4.0, License: https://creativecommons.org/licenses/by-sa/4.0/deed.en, File:Coronary Angiography.png

Figure 2.10 Picture of an angiography equipment. © *Picture by Neoflash. No changes were made to the picture, CC BY-SA 3.0, License: https://commons.wikimedia.org/w/index.php-curid=11370462; File: Herzkatheterlabor modern.jpeg*

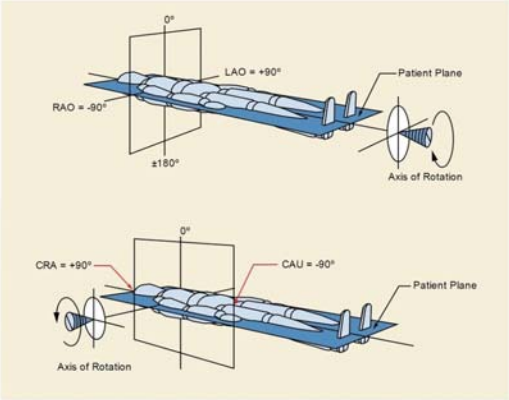

Figure 2.11 Schematic representation of reconstruction system orientation (courtesy www.dicom.nema.org).

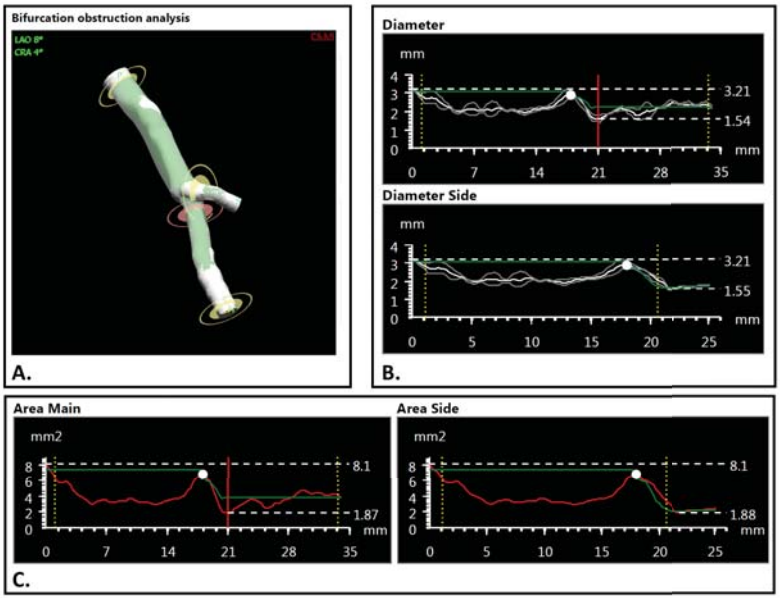

Figure 2.12 Results of the three-dimensional quantitative coronary analysis that were obtained with CAAS (PIE Medical). A: 3D visualisation of the analysed coronary bifurcation. B: Diamenter values of the parent and daughter branches. C: Area values of cross-sections along parent and daughter branches.

2.4.2 Optical coherence tomography: working principles and application

Optical coherence tomography (OCT) is an intravascular imaging technique, known also as intravascular OCT (IV-OCT), that was introduced for the

first time for coronary intervention in 1991 (Prati et al., 2011). Nowadays, it is largely performed both during diagnostic phase and surgical treatment, as reported by Toutouzas and collegues in (Toutouzas et al., 2015), Wahle and colleagues (Wahle et al., 1999) and Cimen and co-authors in (Çimen et al., 2016). This strategy enables to increase the pull-back speed, since the detector receives simultaneously reflections with all echo time delays. This imaging modality ensures higher image resolution compared to those ultrasound based (i.e. intravascular ultrasound, IVUS) with axial resolution ranging from 12 to 18 μm (against 150 to 200 μm of IVUS) and lateral resolution ranging from 20 to 90 μm (against 150 to 300 μm of IVUS) (Bezerra et al., 2009).
OCT is a catheter based imaging intravascular technique that uses light with a bandwidth within the near-infrared spectrum (Bezerra et al., 2009). The working principle is based on the light interference phenomenon and the measurement of the resultant backscattered signal. In general, an interferometer splits the light into a sample arm, that goes to the tissue, and a reference arm, that carries known signal delays. These two signals merge in a unique light beam that reaches a photo-detector. The aim of the reference light arm is essentially the creation of signals with controllable features to be compared with the backscattered sample signal. In a time-domain OCT (TD-OCT) device known echo signals are generated by a moving mirror, therefore, the acquisition speed is limited by the feasibility of specific seed delays. Whilst, frequency-domain OCT (FD-OCT) employs a variable frequency light to carry known information, then, the reference arm is reflected by a fixed mirror before recombining with the sample arm.
In Fig.2.13 the outputs of a OCT acquisition are shown (Prati et al., 2011). In particular, the vessel inside is imaged by multiple axial scans, named A-scans, that are performed in a spiral-like manner by the OCT probe and their combination produce planar slices, called B-scan, during catheter pull-back. Finally, the whole acquisition can be represented as a 3D image, volume scan.
OCT is more and more used to guide PCI by providing information on atherosclerotic plaque extension and composition, and by monitoring stent implantation (Nammas et al., 2013; Regar et al., 2011). A drawback of light-based imaging modalities is the fact that infrared light cannot penetrate blood, then they require the interruption or clearance of the blood flow. FD-OCT is the recommended imaging technique because the high acquisition speed does not require a prolonged flow blockage. Once the blood is cleared by the contrast agent, the pull-back can be automatically started in order to improve the acquisition quality. The C7-XR Fourier-Domain OCT system (St. Jude Medical, St. Paul, MN, USA) with a C7 Dragonfly catheter (St. Jude Medical) is capable of

imaging a segment of 54 mm with a pull-back speed of 18 mm s^{-1}, resulting in a data frame rate of 180 frames per second.
The entire OCT image set is composed of high resolute images that can be processed off-line by dedicated software for diagnostics and intervention monitoring purposes. It is largely confirmed in the literature that the near histological resolution of OCT allows for the characterisation of the vessel wall and plaque composition (Tenekecioglu et al., 2017a). For instance, fibrous component and calcifications are recognisable in the images that are obtained during the acquisition as a result of the different optical properties of such media. Furthermore, the excellent image quality enables detailed assessment of the intervention outcomes after stent insertion. Because of the opacity of metallic materials to light, the stent struts appear in OCT images as high reflecting area, which corresponds to the internal surface of the scaffold, that is followed by a tailing black shadow. In general, the assessment of stent position is performed by means of the distance of the stent to the lumen boundary. Strut malapposition is reported when the distance between the center of the bright reflection region and the arterial wall is larger than the strut thickness (Tearney et al., 2012). The interaction between the stent struts and the vessel wall can be evaluated through the embedment analysis. Essentially, the degree of embedment is estimated from the distance between the midpoint of the innermost strut surface and the lumen contour. An additional relevant aspect is the tissue prolapse, tissue protrusion between adjacent struts, common in case of lipids rich plaques (Tenekecioglu et al., 2017a). Moreover, the residual stenosis area can be computed as a percentage of the lumen area out of the scaffold. The BRS degradation can be detected by the residual backscattering from the struts and the vessel wall.
Evidences that has been reported in the literature, support the connection between lesion induced by stent implantation and wall shear stress (WSS) with neointimal proliferation. The development of automatic and robust image segmentation algorithms and computational models for the simulation of blood flow, have extended the application of OCT to the assembling of detailed 3D geometries for the study of local hemodynamics. A limitation of this intravascular imaging modality is the low penetration depth, 2-3 mm, respect to IVUS, 8-10 mm. This last is also applied as IVUS-virtual histology (IVUS-VH), that relies on the elaboration of the signal to build tissue maps and plaque classification. An advanced diagnostic technique comprises the co-registration between IVUS-VH and OCT, taking the advantage of the strength of both technologies (Tearney et al., 2012).
The International Working Group for Intravascular OCT Standardization and Validation (IWG-IVOCT), founded in 2008, sees experts from both academy

and industry that are prone to facilitate an uniform use of the OCT technology. For instance, IWG-IVOCT proposes standard nomenclature, procedure and image interpretation guidelines and measurement methodology. A consensus document that was produced in the 2012 by the IWG-IVOCT (Tearney et al., 2012) was focused on the description of guidelines for the interpretation of OCT images for CAD diagnostics and assessments after stenting.
In Fig.2.14 is an OCT image of a normal coronary artery wall. This last appears composed of three layers (i.e. tunica intima, tunica media and tunica adventitia) that are separated by elastic brighter membranes, respectively internal (IEM) and external (EEM). An atheroma appears as local thickening or erosion of the layered vessel wall (Fig. 2.15A), eventually fibrous components induce high light backscattering (Fig. 2.15A-B), with heterogeneous region where calcium is located (Fig. 2.15C-D).
Unstable plaques can rapture and erode, eventually leading to plaque ulceration that is defined as a recess in the plaque at the interface between lumina and intima (Fig. 2.16). The presence of a thrombus is visible in OCT images as a mass attached to the innermost wall surface or as a floating object within the lumen (Fig.2.17).
In conclusion, the near histological resolution of OCT explains its wide application in cardiovascular intervention and provides enough information for the creation of detailed patient-specific models. The co-registration with angiography images completes the view by providing the three dimensional shape of the treated blood vessel. Thus, the effort of many research groups is focused on the definition of reliable methodologies that elaborate medical images to build 3D geometries of the scaffolded coronary artery, so that the hemodynamics of each patient can be simulated.

2.5 Evaluation of hemodynamics in stented coronary arteries

Computational fluid dynamics (CFD) is a well established approach to simulate the blood flow and to compute parameters that are used as surrogates for the prediction of negative vessel remodelling due to the presence of the stent, such as neointima hyperplasia (NIH) that is the the thickening of arterial walls due to the proliferation and migration of vascular smooth muscle cells in the tunica intima. In this context, the application of medical images, such as angiograms and OCT, enables to investigate the local hemodynamics at a high

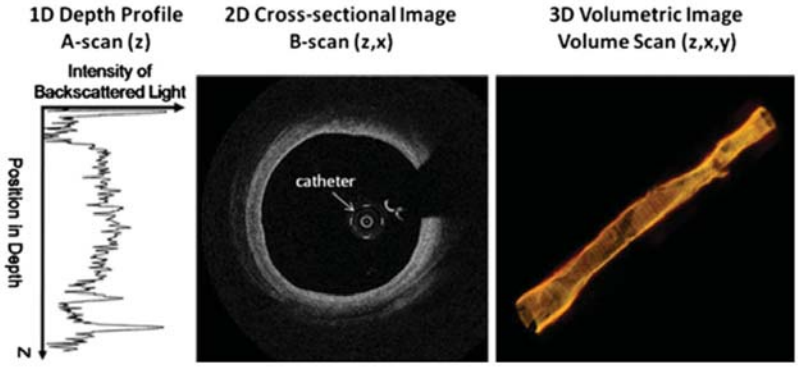

Figure 2.13 Optical coherence tomography (OCT) outputs schemes: intensity profile, A-scan (left), cross-section image, B-scan (center), and volume scan (right). *Reprinted with permission from The international journal of cardiovascular imaging, Vol. 27(2):251-258. Prati F., et al. Intracoronary optical coherence tomography, basic theory and image acquisition techniques.* © *2011.*

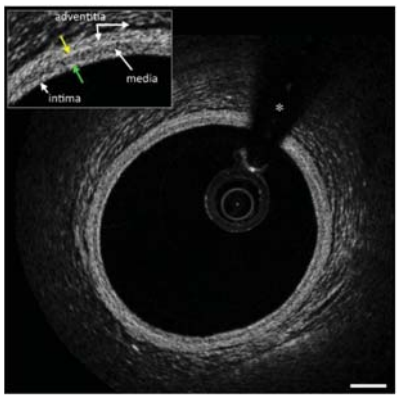

Figure 2.14 OCT image of a normal healthy coronary artery wall. The three layers are distinguishable separated by the internal elastic membrane (IEM) and the external elastic membrane (EEM), lighter than the tunicae intima, media and adventitia. *Reprinted with permission from Journal of the American College of Cardiology, Vol. 59(12):1058-1072. Tearney, G. J., et al. Intracoronary optical coherence tomography: a comprehensive review: clinical and research applications.* © *2012 American College of Cardiology Foundation. Published by Elsevier Inc. This is an open access article under the CC BY-NC-ND license (http://creativecommons.org/licenses/by- nc-nd/4.0/1.*

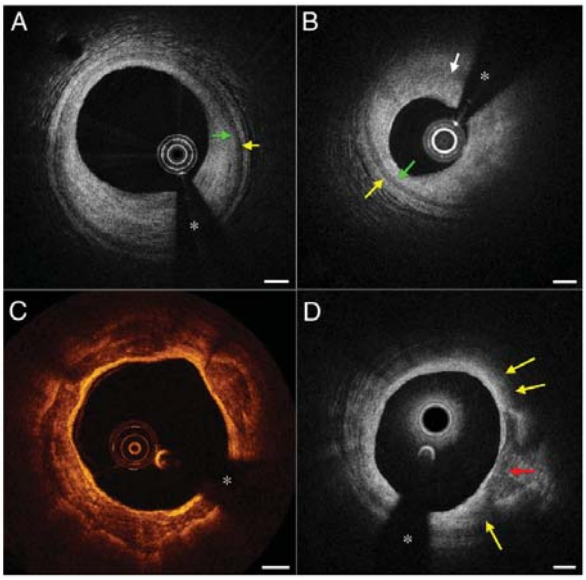

Figure 2.15 OCT image of a diseased coronary artery wall. A: Fibrous plaque with internal (green arrow) and external (yellow arrow) membranes. B: Plaque without elastic membranes (white arrow). The external (yellow arrow) and internal (green arrow) elastic membranes are opposite the plaque. C: Fibrocalcific plaque with circumferential heterogeneous region and clearly pictured contours. D: Plaque with calcific deposit and regions with delineated boundaries, including calcium (red arrow), and areas with lipid composition (yellow arrows). Scale bars represent 500 μm. *Reprinted with permission from Journal of the American College of Cardiology, Vol. 59(12):1058-1072. Tearney, G. J., et al. Intracoronary optical coherence tomography: a comprehensive review: clinical and research applications.*

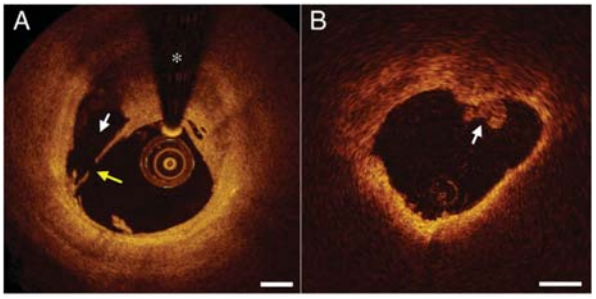

Figure 2.16 OCT image of an ulcerated plaque. A: Plaque with a fractured fibrous cap (arrows) and the resultant cavity (white arrow). B: Plaque erosion with a thrombus (white arrow) on a lumen surface. *Reprinted with permission from Journal of the American College of Cardiology, Vol. 59(12):1058-1072. Tearney, G. J., et al. Intracoronary optical coherence tomography: a comprehensive review: clinical and research applications.* © *2012 American College of Cardiology Foundation. Published by Elsevier Inc. This is an open access article under the CC BY-NC-ND license (http://creativecommons.org/licenses/by- nc-nd/4.0/1.*

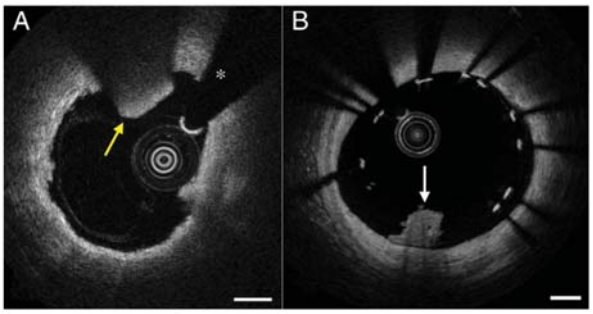

Figure 2.17 OCT image of a thrombus within a coronary lumen. A: Tissue prolapse (arrows). B: Malapposed stent struts. *Reprinted with permission from Journal of the American College of Cardiology, Vol. 59(12):1058-1072. Tearney, G. J., et al. Intracoronary optical coherence tomography: a comprehensive review: clinical and research applications.* © *2012 American College of Cardiology Foundation. Published by Elsevier Inc. This is an open access article under the CC BY-NC-ND license (http://creativecommons.org/licenses/by- nc-nd/4.0/1.*

level of detail thanks to the achievable patient-specific 3D geometries.

2.5.1 Basics of fluid dynamics

Before proceeding with the description of the computational models that were defined for the blood flow simulations, it is worth recalling some principles that make the discussion more clear and complete. In general, the investigation of the motion of a large number of particles is performed by assuming that the density of the fluid allows to approximate a small volume as a continuum. The dynamic behaviour of a single-phase fluid is driven by three conservation laws: the conservation of mass, that expresses the total mass is preserved in the volume; the conservation of momentum, which states that the rate of change of the fluid particle momentum equals the sum of the forces on that particle; the conservation of energy, which states that any change of the internal energy in the control volume is driven by the rate of work of the forces acting on it and by the overall heat flux in it. In general, the change of each of the above quantities in a control volume is defined by a convective component, which is due to the motion of the fluid and a diffusive flux that depends on the molecular movements, proportional to the spatial gradient of the considered quantity (Blazek, 2015).
For the performed computational simulations incompressibility, constant density and no wall slip condition were assumed. Hence, the continuity and the conservation of momentum equations are described by Eq.2.2:

$$\nabla \cdot \mathbf{v} = 0 \tag{2.2a}$$

$$\rho \frac{\partial \mathbf{v}}{\partial t} + \rho \left(\mathbf{v} \cdot \nabla \right) \mathbf{v} = -\nabla p + \nabla \cdot \mathbf{T} \tag{2.2b}$$

with $\mathbf{v}$ is the velocity vector, p is the pressure, $\mathbf{T}$ is the viscous stress tensor.

It is defined a control volume by a closed surface whose normal is directed outwards the volume. Hence, the components τ_{ij} of the stress tensor $\mathbf{T}$, result from the friction between the fluid particles at the element surface of the control volume. In particular, when $i = j$ the stress component is acting on the face perpendicular to the respective direction, whereas if $i \neq j$ that is the j-th component of the tensor acting on the phase perpendicular to the direction i.
The τ_{ij} are defined as:

$$\tau_{i,j} = \mu \left(\frac{\partial u_i}{\partial x_j} + \frac{\partial u_j}{\partial x_i} - \frac{1}{2} \delta_{i,j} \frac{\partial u_k}{\partial x_k} \right) \tag{2.3}$$

where $\delta_{i,j}$ neglects the term for $i \neq j$. The definition of the stress tensor depends on the dynamic properties of the fluid, introduced by μ. This last is constant for Newtonian fluids and depends on the shear rate for non-Newtonian fluids, several models have been proposed to resemble experimental observations on different fluids. Among the relations for the dynamic behaviour of blood in small vessels (i.e. coronary arteries) the most common is the Bird-Carreau model:

$$\mu = \mu_\infty + (\mu_0 - \mu_\infty) \left[1 + (k \cdot \tau_{ij})^2\right]^{\frac{(n-1)}{2}} \tag{2.4}$$

with μ_0 and μ_∞ are the zero-shear-rate and infinite-shear-rate viscosity, k is the inverse of a characteristic shear rate and n is the power-law exponent (Carreau, 1972; Shibeshi and Collins, 2005).

2.5.2 Surrogates for flow conditions

As mentioned in the previous chapter Section2.2, the endothelium cells mainly react to the blood flow pattern, especially to the forces that are induced by the shear stress at the wall. Therefore, the principle quantity to be investigated is the wall shear stress (WSS) defined as:

$$\vec{\tau}_w = \vec{n} \cdot \mathbf{T} \tag{2.5}$$

with $\mathbf{T}$ is the stress tensor, which components are defined in Eq.2.3, and $\vec{n}$ is the normal vector to the wall surface.
Since the blood flows in the coronary arteries driven by the cardiac activity, its velocity is a time-dependent quantity with periodic features. As a result the first surrogate for NIH evaluation is the time-averaged WSS (TAWSS), this quantity presents the history of WSS over a period of the cardiac cycle and is defined as:

$$TAWSS = \frac{1}{T} \int_0^T |\bar{\tau}_w| dt \tag{2.6}$$

where T is the period of the pulsatile flow-rate waveform.
There are evidences in the literature that demonstrate the influence of endothelium cell (EC) reaction to flow shear stress at the wall. In particular, values of TAWSS above 1 Pa were found to trigger a stretch effect on EC, whereas for TAWSS below 0.4 Pa or oscillatory values induce less ordered EC configurations. This last makes the endothelium a membrane as permeable to atherosclerotic agents. The oscillation of TAWSS values during a cardiac period has both

spacial- and time-dependent nature. It can be quantified via the oscillatory shear index (OSI), which is defined as (Ku et al., 1985):

$$OSI = \frac{1}{2}\left(1 - \frac{|\int_0^T \bar{\tau}_w dt|}{TAWSS}\right) \tag{2.7}$$

In case of a non-oscillatory flow the OSI equal to zero, whereas the maximum oscillation of TAWSS results in a OSI equal to 0.5.
Flow recirculation causes stagnation of particles and, consequently, atherogenesis and ISR. The prediction of the relative residence time (RRT) of a partical can be obtained by combining information from OSI and TAWSS:

$$RRT = \frac{1}{TAWSS(1 - 2 \cdot OSI)} \tag{2.8}$$

Therefore, lumen volume regions that are prone to flow recirculation and stagnation, such as at bifurcations and scaffolded segments, are investigated by post-processing results from computational simulations. The quantities introduced are known as surrogate parameters for the quantification of adverse events, such as NIH and ISR.

2.6 State-of-the-art in the modelling of patient-specific geometries from medical images for CFD simulations

Despite the achievable image high resolution, the main drawback of OCT is the fact that it lacks of information about the 3D shape of the analysed coronary segment. Consequently, different imaging modalities are needed to reconstruct the geometry of the treated blood vessel (Bourantas et al., 2005; Chiastra et al., 2016; Çimen et al., 2016; Ellwein et al., 2011). For instance, Ellwein and colleagues in (Ellwein et al., 2011) proposed a method to extract the guide-wire path from a 3D reconstruction of a post-operative blood vessel that was built with computerised tomography (CT). In particular, a minimum energy trajectory across the tortuous vessel was computed and was used to align the lumen contours from OCT. The deployed stent was drawn by taking into account the reconstructed vessel geometry. Whereas, Chiastra and co-authors (Chiastra et al., 2016) reconstructed a stented coronary artery segment by positioning the

lumen boundaries perpendicularly to the vessel centerline and the stent insertion was simulated with a finite element analysis.
The virtual stenting approach was used to be the only mean to resemble the expanded stent configuration, which was replaced by the rise of intravascular imaging technologies. The computational modelling of stenting procedure has reached strong accuracy (Morlacchi et al., 2014), but the outcomes depend on many parameters, such as the knowledge of the mechanical properties of both stent and balloon, alongside details about the steps followed during the intervention procedure. Therefore, the likelihood of achieving the actual final stent struts position, relative to the internal vessel wall, is challenging. Moreover, it is not possible to predict neither the position of the stent relative to the lesion nor its rotation respect to the vessel principle axis. This is a drawback of virtual stenting when it is aimed to hemodynamics studies because malapposed stent struts represent an obstacle to the flow stream and induce small flow recirculation. Such aspect is relevant especially when the stent is implanted at a bifurcation, as the struts interfere with the separating flow.
The recent introduction of OCT in cardiovascular intervention has opened the way for new strategies that enable the exact replication of the stent position in the vessel lumen. That is relevant because the WSS is strongly related to the local geometry, since it is the tangential force per unit area induced by the blood flow on the lumen surface. Several strategies proposed in the literature (Bourantas et al., 2014b; Papafaklis et al., 2015; Tenekecioglu et al., 2017b; Thondapu et al., 2018; Torii et al., 2017) implemented a method that comprised: the manual tracing of the internal lumen contour, accounting for the stent struts, at each OCT frame; the contours alignment on the angiogaphic 3D vessel centerline by superimposing the contour centroids, any side branch was used as landmark for contour twist error reduction; the interpolation of the resultant aligned contours with a non-uniform rotational B-spline surface. This resultant geometry resembled the actual stent implanted shape, although the surface was corrugate and presented discontinuities.
Improved algorithms were applied in the literature for the reconstruction of implanted Absorb BVS scaffolds, described by Gogas and co-authors in (Gogas et al., 2013). The approach takes the advantage of an expert operator for the classification of stent struts points, which were aligned with the angiographic 3D vessel centerline. A cubic spline interpolating the aligned points was a rail for rectangles that defined the scaffold cross-sections. In other works the stent was reconstructed from the knowledge of the stent design. In particular, O'Brien and colleagues (OBrien et al., 2016) aligned the strut point cloud with a straight centerline and placed surfaces on the voxels by means of an

enhanced marching cubes algorithm. Differently, the methodology described in this dissertation ((Migliori et al., 2017), (Migliori et al., 2018), (Chiastra et al., 2017a),(Chiastra et al., 2017b)) comprised the morphing of the actual stent skeleton on the corresponding 3D point cloud, that was obtained from the centerline method. Briefly, the stent skeleton at its free expanded configuration was extracted from a sample of the implanted stent design, then, it was morphed by minimising the distance between the line and the stent point cloud. Thus, the resultant deformed skeleton was a rail for cross-sectional curves and the final stent geometry was achieved by interpolating these with a surface. All the approaches described above provided good replication of the actual stent position, however, this last methodology has the advantage of emulating the degree of stent apposition.

2.6.1 Modelling of blood flow through computational simulations

The modelling of patient-specific hemodynamics is crucial to estimate the reaction of the vessel wall to the endovascular scaffold, which requires both an accurate geometric replication and the knowledge of the fluid dynamic conditions. This latter comprises the definition of patient-specific boundary conditions, that are values of pressure and flow rate at the boundary of the reconstructed vessel segment. Although the technology available allows in-vivo measurements, in real practise the high invasiveness and the heart contracting movements make the task a hard challenge, especially after stent implantation. Indeed, the flow stream forces the movements of the catheter in the vessel and the target acquisition point could be unreachable.
In order to overcome such limitation, patient's anatomic and flow features are commonly used to estimate the characteristic boundary conditions. The flow rate at the inlet can be estimated by the velocity of the radio-opaque liquid across the coronary artery during the angiography acquisition. In particular, the relation proposed by Sakamoto and colleagues in (Sakamoto et al., 2013) considered the number of frames required by the liquid to flow through the lumen volume of a coronary segment free from side branch. The low acquisition frequency of the available angiography equipments, that is about 15 frames s^{-1}, limits the accuracy of the resultant flow rates. However, the frame-count approach is a valid alternative to the definition proposed by van der Giessen and colleagues in (Van der Giessen et al., 2011) that estimates the inlet flow rate via the diameter of the cross-section:

$$q_{inlet} = 1.43 \cdot d_{inlet}^{2.55} \tag{2.9}$$

Such relation fitted the measurements of flow peak velocity that were recorded with a Doppler wire by Doriot and colleagues (Doriot et al., 2000) in the branches of normal coronary bifurcations of 21 patients. Moreover, the typical wave form of the flow velocity during the cardiac cycle was described by Davies and co-authors (Davies et al., 2006) (Section2.1) and can be implemented in the computational model to define the variation in time of the flow rate at the inlet, so that the variation of the WSS in time (i.e TAWSS) can be computed.
Concerning the conditions at the outlets of the physical domain, the relationships between diameters of bifurcation branches Murray's law (Murray, 1926) and HK model (Huo et al., 2009) (Section2.3.1) can be used to define the flow split at the outlets:

$$\frac{q_{D2}}{q_{D1}} = \left(\frac{d_{D2}}{d_{D1}}\right)^{\alpha} \tag{2.10}$$

where q_{D1} and q_{D2} are the flow rate at the branch with larger and smaller diameter, respectively d_{D1} and d_{D2}, whereas the value of α depends on the formula that is considered:

1. van der Giessen model: $\alpha = 2.27$
2. Murray model: $\alpha = 3$
3. HK model: $\alpha = 2.33$

Although the relationships introduced above seek to emulate experimental data that were acquired across the cardiovascular circulation, the variability among patients' physiological conditions and the lack of in-vivo validation tests limit the accuracy of the mathematical models, which provide limitations of the achievable CFD results (Van der Giessen et al., 2011).

Chapter 3

A validated OCT-based methodology for the reconstruction of coronary arteries with stent

This Chapter presents the developed OCT-based reconstruction methodology and the validation procedure. A typical geometry of a human coronary segment with bifurcations was resembled as a rigid phantom. A metallic stent was deployed in the phantom, then it was imaged with OCT and μCT. This latter provided a reference geometry for validation purposes. A proof-of-concept CFD simulation was performed using the achieved reconstruction.

The content of this chapter can be found in the works **Migliori S.**,et al. (Migliori et al., 2017) and Chiastra C., Montin E., Bologna M., **Migliori S.**, et al.(Chiastra et al., 2017b) that were published in the Journal of Medical Engineering and Physics, and in PloS ONE, respectively..

3.1 Introduction

THE clinical challenge of percutaneous coronary interventions (PCI) is highly dependent on the recognition of the coronary anatomy that features each individual. The classic imaging modality used for PCI is angiography, but advanced imaging techniques that are regularly performed during PCI, like optical coherence tomography (OCT), may provide detailed knowledge of the pre-intervention vessel anatomy as well as the post-procedural assessment of the specific stent-to-vessel interactions. Computational fluid dynamics (CFD) is an emerging investigational field in the setting of optimisation of PCI results.

This Chapter describes a framework for the performance of computational fluid dynamics simulations (CFD) on a patient-specific coronary artery geometry (Fig.3.1). Briefly, it includes the elaboration of OCT images that are acquired during PCI to segment the lumen contour and the implanted stent. These components are aligned with the centerline of the treated vessel, obtained from two angiography projections. Then, a computer-aided design (CAD) software is employed to reconstruct the three-dimensional geometry of both stent and vessel. Finally, the achieved geometry is discretised in tetrahedral elements and a proof-of-concept CFD simulation is fulfilled.

The accuracy of the reconstruction methodology was evaluated in both the image segmentation and the alignment/orientation processes. The former was validated against manual segmentation of OCT images where two image readers identified the region of interest for the lumen and the stent. The latter was assessed by comparing the outcomes obtained for the lumen and the stent respectively with the reconstruction from μCT scan. A strong correlation between automatic and manual segmentation of lumen in terms of area values was found. Similarity indices resulted $> 96\%$ for the lumen segmentation and $> 77\%$ for the stent strut segmentation. The 3D reconstruction achieved for the stented phantom was also assessed with the geometry provided by X-ray computed micro tomography scan, used as ground truth, showing the incidence of distortion from catheter-based imaging techniques. The 3D reconstruction was successfully used to perform CFD analyses, demonstrating a great potential for patient-specific investigations. In conclusion, OCT may represent a reliable source for patient-specific CFD analyses which may be optimised using dedicated automatic segmentation algorithms.

In Fig.3.2 is reported the workflow to extract data for the necessary elaborations, leading to the optimisation of the reconstruction methodology and its validation. In the following subsections each step is described in detail.

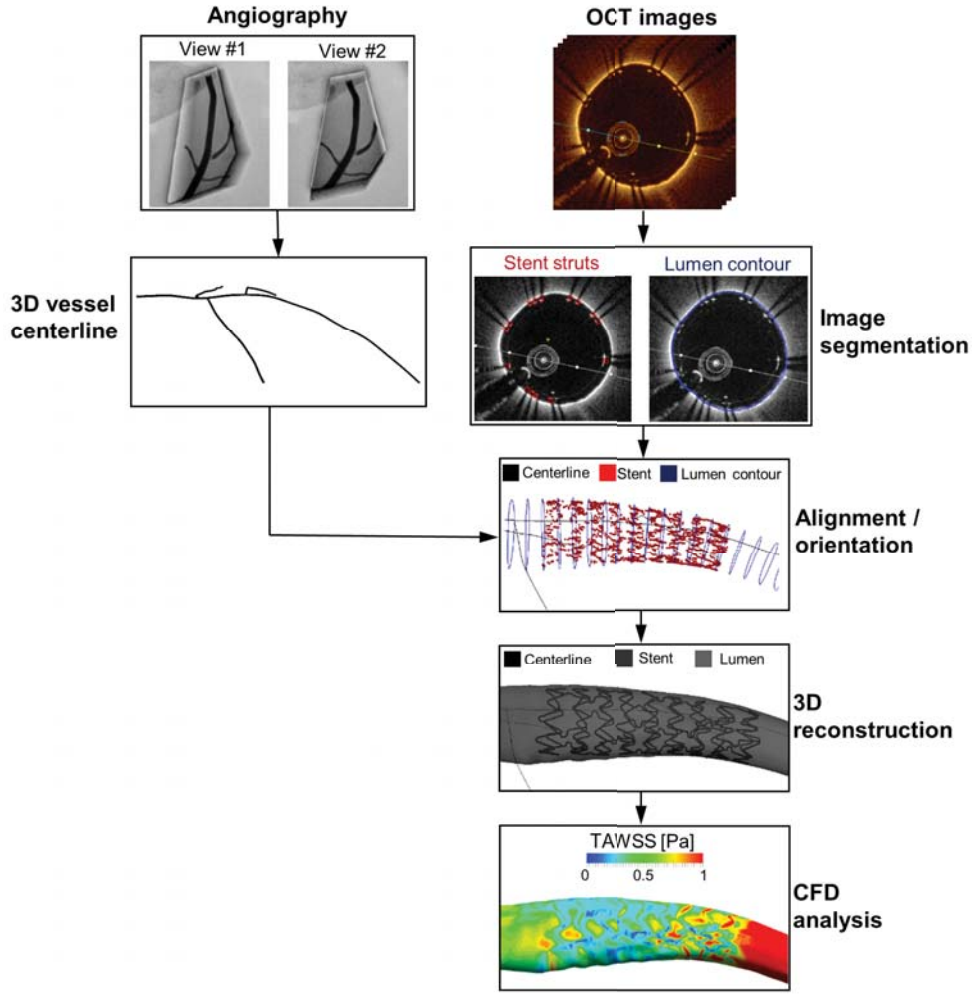

Figure 3.1 General work-flow of the proposed methodology, suitable for the 3D reconstruction of a stented coronary phantom from optical coherence tomography (OCT) images and the subsequent execution of computational fluid dynamics analyses. In the box on the right, the contour map of time-averaged wall shear stress (TAWSS) is shown.

3.2 Design of a human coronary artery phantom and data acquisition

A rigid phantom emulating a typical human LAD artery with multiple bifurcations was designed using the computer-aided design (CAD) software Rhinoceros v.5 (Robert McNeel and Associates, Seattle, WA, USA). In Fig.3.3

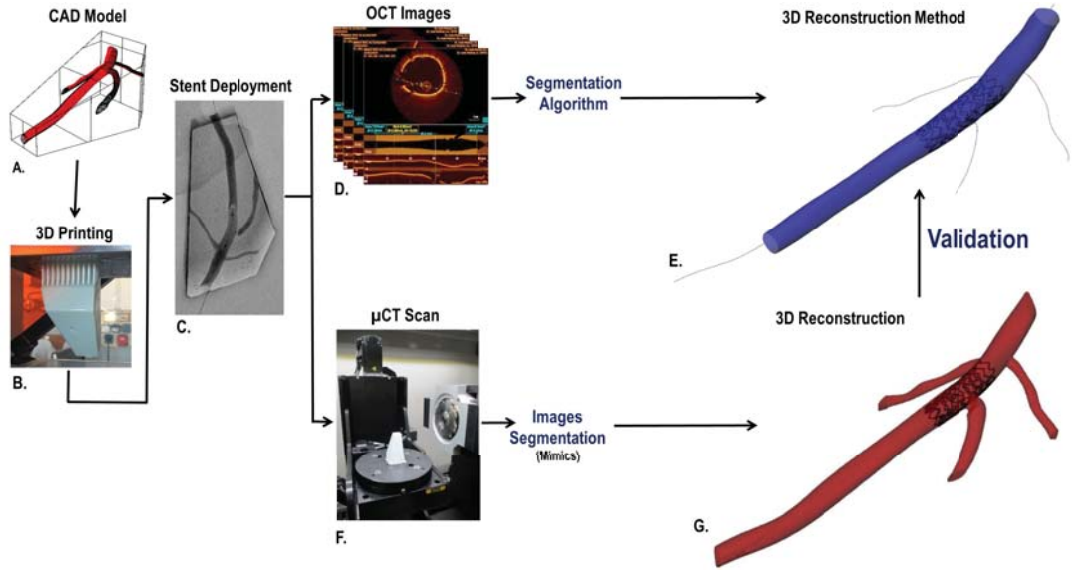

Figure 3.2 Workflow that was followed to obtain useful data to develop and validate the reconstruction methodology. A: 3D CAD model of the designed phantom, resembling a human typical coronary artery segment with bifurcations. B: The phantom was printed in a rigid block in which the cavity represented a patient-specific coronary artery geometry. C: A coronary stent was implanted in the phantom main branch. D: The phantom with the stent was imaged with OCT and the images were elaborated with the proposed segmentation algorithm. E: The 3D-OCT was used to reconstruct the phantom main branch with the stent. F: The rigid phantom with the implanted stent were imaged with μCT scan and the images were elaborated with a commercial software. G: The resultant geometry was used to validate the 3D-OCT method.

the CAD model of the solid block is displayed, where the cavity is highlighted in red and resembles the blood vessel lumen. This last comprises the main branch (MB) and the three side branches (SBs). The main sizes of the phantom were 37.4 mm, 53.8 mm, and 32.8 mm; the MB was 64 mm long with diameters at inlet and outlet of 3.5 mm and 2.8 mm, respectively. The phantom was printed through a stereo-lithography (STL) apparatus DWS028JPlus (DWS, Italy) at the +LAB of Politecnico di Milano (Montin et al., 2016) (Fig.3.4a). The STL apparatus is equipped with a monochromatic actinic laser source (Solid State Bluedge® BE-1500A/BE-1500AHR) with an emitting output power of 30 mW at λ= 405 nm and a 22 μm spot beam diameter. A commercially available STL resin DM220™ (DWS) was used for model printing. Prior to the printing step, the STL files were processed with dedicated 3D parametric software NAUTA+®(DWS) that enables to reorient the objects on the working platform and to support it. Cylindrical supports with a minimum diameter of 1.2

mm were necessary to withstand the weight of the model during the printing (Fig.3.4b). The resulting processed objects were subsequently sent to Fictor® (DWS) the software machine that directly controls the 3D printer and performs slicing operation according to the user-imposed building parameters. Particularly, the models were divided in three blocks corresponding to the base, the supports and the object, respectively. Optimized printing conditions for each block are listed in Table 3.1. At the end of the printing procedure, the object was washed twice with ethanol to remove unreacted resin and dried with air. To complete the polymer conversion, the printed model was further exposed to light for 30 minutes in a dedicated UV-curing unit (λ=405 nm, DWS).

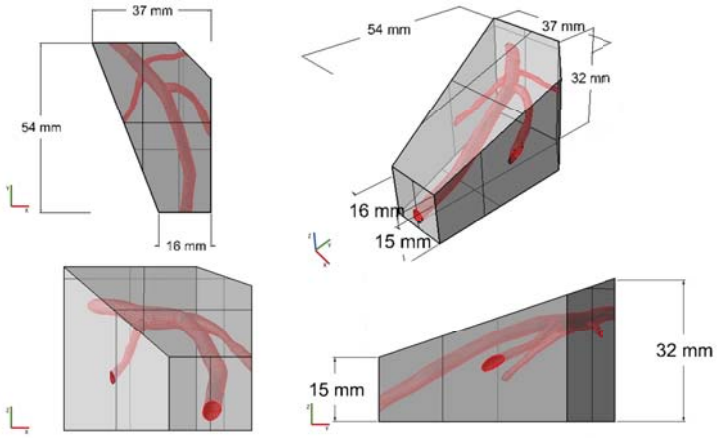

Figure 3.3 Projections of the computer-aided design (CAD) model of the phantom.

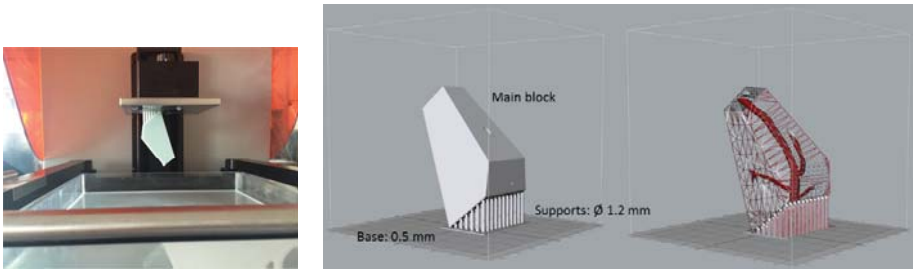

(a) (b)

Figure 3.4 a: Stereo-lithography (STL) apparatus DWS028JPlus with the printed phantom. b: Rendered, left, and wireframe, right, visualization of the 3D model implemented in Nauta+®. The orientation and the supports dimensions were optimized to withstand the weight of the object while printing proceeds.

Table 3.1 Optimized printing parameters values imposed for each of the three main blocks through Fictor

Block $[mm]$	**Layer height** $[mm]$	**Number of infill** $[mm]$	**Hatching** $[mm]$	**Laser speed** $[mm\ s^{-1}]$
1	0.03	2	0.02	258
2	0.03	2	0.02	2200
3	0.03	2	0.02	4300

The printed phantom was used to acquire angiography and OCT images at the Hemodynamic Lab of the Institute of Cardiology, Catholic University of the Sacred Heart, in Rome (Italy). A Multi-Link 8 stent (Abbott Laboratories, Abbott Park, IL, USA) (diameter = 3.5 mm, length = 12 mm) was deployed by an intervention cardiologist following a standard stenting procedure. In particular, the coronary stent was inserted in the MB by balloon inflation at 16 atm for 20 seconds. To limit stent malapposition, a balloon (diameter = 3.5 mm, length = 12 mm) was inflated at 16 atm. The phantom with the stent was imaged with a single-plane C-Arm angiography system (Allura FD10, Philips, Amsterdam, The Netherlands), as during cardiovascular intervention procedures. The output was a sequence of digital images, stored in Digital Imaging and Communications in Medicine (DICOM) format. Finally, OCT images were acquired in the MB using C7-XR Fourier-Domain OCT system (St. Jude Medical, St. Paul, MN, USA) with a C7 Dragonfly catheter (St. Jude Medical). Length of the acquired segment was 54 mm and the automated pull-back speed was 18 mm s^{-1} resulting in a data frame rate of 180 frames s^{-1}. The image set comprised 540 frames with relative distance of 100 μm and each OCT frame was recorded as DICOM.
With the aim of results validation the phantom was scanned with a X-ray μCT NSI X25 system (NSI Inc., Rogers, MN, USA), equipped with a Dexela detector with 75 μm pixel pitch allowing for the acquisition of 1536x1944 pixel radiographies at full-binning with 16 bit encoding (Montin et al., 2016) (Fig.3.5). Details on this imaging technique, recently enriched with in-situ loading apparata and image processing algorithms for in bulk strain assessment, can be found in the works of Fedele and co-authors (Fedele et al., 2014, 2013a,b). The obtained μCT slices were post-processed with Mimics software (Materialise, Leuven, Belgium) to extract the vessel and stent centerlines. This last was used in the reconstruction methodology, so that both the reference and the tested reconstructions were superimposed.

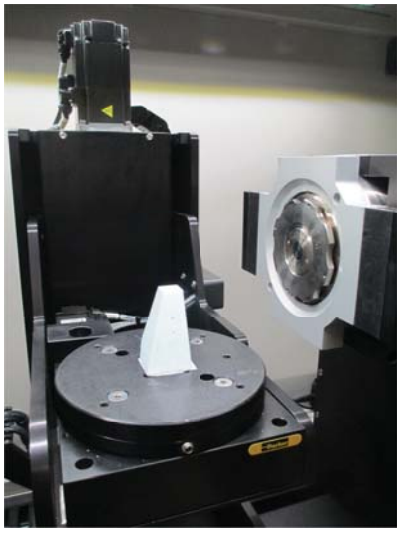

Figure 3.5 X-ray μCT NSI X25 system with the phantom.

3.3 Image segmentation algorithm

The proposed 3D reconstruction method entirely runs in a MATLAB environment (Mathworks, Natick, MA, USA) and consists of four stages: *i)* image pre-processing, *ii)* lumen contour detection, *iii)* stent struts detection, and *iv)* alignment and orientation of detected lumen contours and stent struts with the vessel centerline. The reconstruction method is described in the following subsections. Additional details about the first three stages can be found in the work of Chiastra and colleagues (Chiastra et al., 2017b). Finally, results from the segmentation algorithm were validated against manual segmentation of the OCT image set.

3.3.1 Image pre-processing

First, each OCT frame (Figs.3.6A and 3.7A) is converted from RGB color mode to greyscale and the line dividing the two vessel visualization modalities (i.e. cross-sectional and longitudinal views) is used to isolate the vessel cross-section. Second, pixels belonging to the OCT visualisation tools (i.e. calibration bar, scale, and other information related to the image) are removed. The implemented approach is founded on the fact that such pixels have both same

intensity and position across frames. Consequently, their greyscale intensity is forced to zero.
The processed images are converted in polar coordinates for further elaborations (Figs. 3.6B-3.6E and 3.7B-3.7E). This procedure aims to express the position of each pixel in an image through radial and angular coordinates that are centered on the OCT catheter. Indeed, a dataset generated from OCT pull-back is coaxial to the catheter and the infrared light is radially emitted from the OCT probe (A-scan). Therefore, the catheter covers a region at the top of the image in polar coordinates and it is deleted by image global thresholding at a selected image portion. That region is defined taking into account the catheter radius, image resolution, and the highest values of average intensity. The border of the catheter region, ρ_{lim}, is estimated as the last line of pixels with an intensity higher than an imposed threshold (i.e. quantile 95%) on the average intensity. Consequently, the catheter is considered a circle with a radius of $\rho_{cat} = \rho_{lim} + 10$, which includes a tolerance of 10 pixels. Once the OCT catheter region is identified in each image, a first rough removal is performed by forcing to zero all pixels with intensity above the imposed threshold. A finer catheter removal is performed through the search for background pixels (intensity below the quantile 75% in the histogram) across image columns (A-scans) within the filtered region. Thus, when a background pixel is found, all the previous image lines are forced to zero, so that the lumen contour is preserved where it is in contact with the catheter during OCT pull-back.

3.3.2 Detection of lumen contour

Regions with higher intensity pixels are isolated in order to remove noise and to depict the lumen contour portion. The salt-and-pepper noise is removed from each image by applying an intensity thresholding followed by other morphological operations (Gonzalez et al., 2009), including area thresholding and opening. The obtained binary mask is convolved over the greyscale image (Fig. 3.6C). A first edge detection is performed by means of a Sobel operator (Gonzalez et al., 2009). Particularly, this operator computes the gradient of a function and identifies borders within an image. Thus, the first non-zero element found in each column of the filtered image in polar coordinates is accepted as a valid point for the lumen border.
Since the resultant images might have been affected by either residual noise or bifurcation regions, a post-processing phase is included for error correction. The implemented strategy is based on the assumption that the lumen maintains its shape between consecutive frames. Therefore, in the current image a confi-

dence region is defined from the contour pixels found in the previous one with a tolerance of 5 pixels (Fig. 3.6D). Points outside that range are deleted and the image is then filtered to remove small objects.
Resultant gaps along the lumen edge are filled either by linear interpolation or by replicating contour pixels from previous OCT frames. In particular, the strategy is chosen depending on the gap amplitude in terms of number of columns with only zero elements. The detected lumen contours are smoothed with a moving average filter (Fig. 3.6E). Finally, images are converted back in Cartesian coordinates and lumen contours are recorded as points in the 2D plane (Fig. 3.6F).

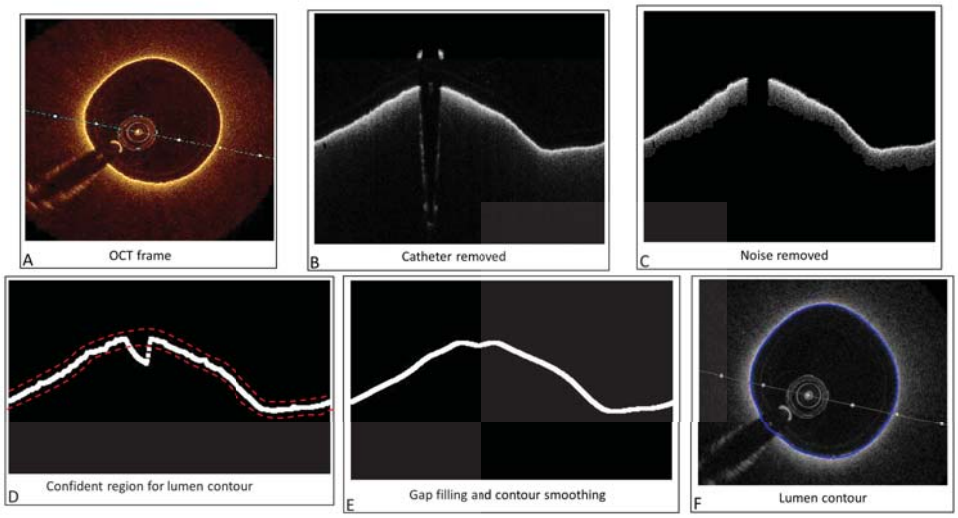

Figure 3.6 Lumen contour detection based on segmented images from optical coherence tomography (OCT). A: Cross-sectional visualization of an OCT frame. B: Grayscale image in polar coordinates after removal of the OCT catheter. C: Masked image after noise removal. D: Binary image in polar coordinates with the identified lumen contour (a dilatation of 2 pixels has been applied to enable the edge visualization) and schematic representation of the confidence region (red dashed line). E: Binary image in polar coordinates of the lumen contour (a dilatation of 2 pixels has been applied to enable the edge visualization) after gap filling and contour smoothing. F: Grayscale image of the cross-sectional visualization with the identified lumen contour (blue).

3.3.3 Detection of stent struts

The detection of metallic stent struts is achieved through the peculiar characteristic of OCT images, where stent struts appear as high reflecting elements (i.e. high intensity region) followed by a trailing shadow (i.e. low intensity region) Fig.3.7A (Wang et al., 2013). Therefore, the intensity profile of each A-scan in the OCT frame is considered in order to estimate struts position. The slope of a line connecting each peak in the intensity profile with the thirtieth consecutive low intensity pixel is computed and pixels that result in higher slope values are considered part of a strut (Bourantas et al., 2003). Columns corresponding to the A-scans that do not cross a candidate stent strut are set to zero. Then, the obtained greyscale images are processed to isolate regions with higher intensity pixels and whose extension is below a certain number of rows, according to the strut thickness (i.e. 10 rows). Lastly, the first sets of high intensity pixels are considered for the following processes.
A fuzzy logic approach is applied to identify strut pixel and delete false positives (Fig.3.7D). In particular, a mask is created to reflect the probability that a pixel in the image belongs to a strut. The mask is a greyscale image with intensity values from 0 to 1 moving from the lumen center towards the lumen contour and 0 below it.
The obtained images are elaborated with a confidence region that is defined by merging information provided by previous and successive 5 images in order to build a smooth curve. Points that are above a tolerance of 5 pixels are deleted (Fig.3.7E).
At the end of the procedure, each image is converted back to Cartesian coordinates. The centroids of regions with white pixels provide the position of stent struts (Fig.3.7F), recorded as points in the 2D plane.

3.3.4 Validation

Results from the segmentation algorithm were assessed through a manual segmentation, which was considered as the reference. This last was performed with the open-source software MRIcro (http://www.mccauslandcenter.sc.edu) by two independent expert image readers. The region-of-interest (ROI) for the lumen was manually traced on 1 OCT frame out of 5, for a total of 95 frames, whereas stent struts were manually identified on the entire OCT dataset of the stented vessel portion, which included 122 frames.
The selected ROI for the lumen was used to compute area values. The correlation between data sets was verified through the Kruskal-Wallis test, Bland-

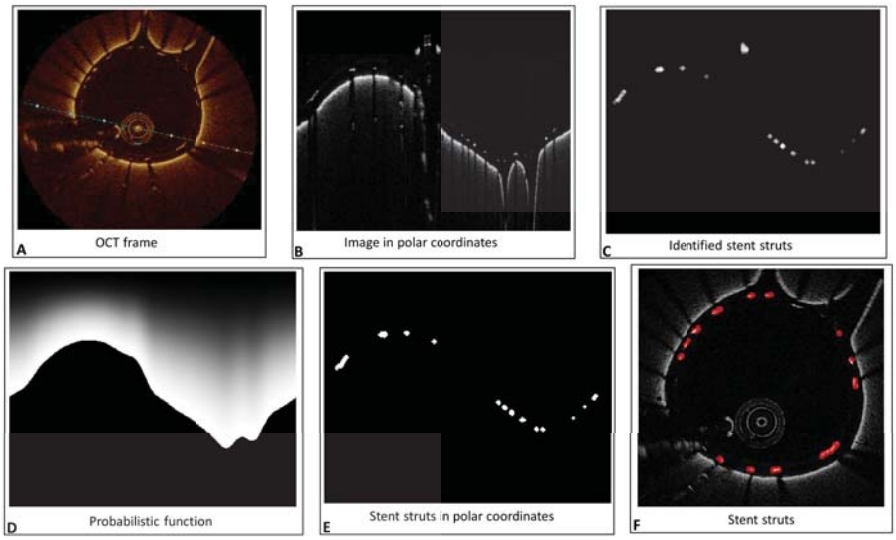

Figure 3.7 Stent struts detection through optical coherence tomography (OCT) segmented images. A: Cross-sectional visualization of an OCT frame with stent struts. B: Grayscale image in polar coordinates after removal of the OCT catheter. C: Masked image after noise removal. D: Grayscale image of the probabilistic function defined for removal of false positives. E: Binary image in polar coordinates of the stent struts (a dilatation of 2 pixels has been applied to better the visualization). F: Grayscale image of the cross-sectional visualization with the identified stent struts (red).(Migliori et al., 2017)

Altman analysis (Bland and Altman, 2010), and linear regression. Discrepancies between the automatic and manual segmentation methods were assessed by means of the computation of similarity indexes (Macedo et al., 2016). These indexes were defined by calculating the number of pixels that exhibited specific features, constituting the following subsets: true positives (TP), pixels that were labelled as lumen by both the segmentation methods, false positives (FP), those depicted only by the automatic segmentation, false negatives (FN), those identified by the manual segmentation, and true negatives (TN), pixels labelled as

background by both the methods. Then, the selected similarity indexes were:

$$Jaccard\ index = \frac{TP}{TP + FP + FN} \tag{3.1a}$$

$$Dice\ index = \frac{2 \cdot TP}{2 \cdot TP + FP + FN} \tag{3.1b}$$

$$Sensitivity\ index = \frac{TP}{TP + FN} \tag{3.1c}$$

$$Specificity\ index_{lumen} = \frac{TN}{FP + TN} \tag{3.1d}$$

The similarity indexes computed for the stent were defined by evaluating the accuracy of the automatic segmentation for the correct number of detected stent struts at each OCT frame. The Jaccard index, Dice index and Sensitivity index were computed using Eq.3.1a, Eq. 3.1b, and Eq. 3.1. The specificity index was defined for stent as follows:

$$Specificity\ intex_{stent} = \left(1 - \frac{FP}{n_{stent}}\right) \tag{3.2}$$

Moreover, correlation between the number of stent struts that were identified with the two segmentation methods was assessed through a Kruskal-Wallis test and the length of apposition (LOA), defined as the radial distance between a strut and the lumen contour (Ughi et al., 2012). The agreement between sets of data was evaluated with the Bland-Altman analysis.

3.4 3D reconstruction methodology

The detected lumen contour and stent struts points were aligned with the angiography centerline, translating in two point clouds in the 3D space. These were used to reconstruct the 3D geometry of both lumen and stent. The former was obtained by interpolating the lumen contour curve with a surface, whereas the latter was achieved via a morphing procedure. The lumen reconstruction and the stent point cloud were validated against the geometry produced by a commercial software from the μCT slices.

3.4.1 Alignment and orientation of the detected components

The detected lumen contours and stent struts were aligned with the centerline of the artery phantom extracted after μCT scan. This enables quantitative

comparison between the reconstruction achieved with the proposed methodology and the reference geometry. The MB vessel centerline was sampled by assuming the same distance between consecutive frames as acquired on the OCT catheter. Such an assumption ensures a correspondence between each point on the MB centerline and each OCT frame. The alignment method included the superimposition of lumen contours on the corresponding vessel centerline point and, subsequently, the orientation according to Frenet-Serret formulas (Eqs.3.3) (Wahle et al., 1999), which resembled the alignment of OCT frames perpendicularly to the curve, as shown in Fig.3.8A. In particular, in Eqs.3.3 the three right-handed orthonormal vectors, i.e. tangential (T), normal (N) and binormal (B), to a space curve (c) are defined as function of the arc length (s). The curvature (k) and torsion (τ) are defined as $k = \det\left\{c^{''}(s)\right\}$ and $\tau = \dfrac{\det\left\{c^{'}(s), c^{''}(s), c^{'''}(s)\right\}}{k^2(s)}$, respectively.

$$\frac{d\mathbf{T}}{ds} = k\mathbf{N} \tag{3.3a}$$

$$\frac{d\mathbf{N}}{ds} = -k\mathbf{T} + \tau\mathbf{B} \tag{3.3b}$$

$$\frac{d\mathbf{B}}{ds} = \tau\mathbf{N} \tag{3.3c}$$

In order to reduce the axial twist angle error that generally rises from intravascular imaging techniques (Bland and Altman, 2010), the centerline of one SB is chosen as the landmark for twist angle estimation. That choice is driven by the quality of the acquired OCT frames concerning the degree of distinction between MB and SB at the carina. A marker for the chosen SB is manually selected on an OCT frame that corresponds to the middle of the bifurcation region so that the twist angle is computed to superimpose the marker on the SB centerline (Fig.3.8B). The whole set of detected components is rotated according to that estimated angle.
Two point clouds are obtained from the alignment and orientation procedure, one for the lumen contours and one for the struts centroids, then used to define a geometry for subsequent CFD analyses.

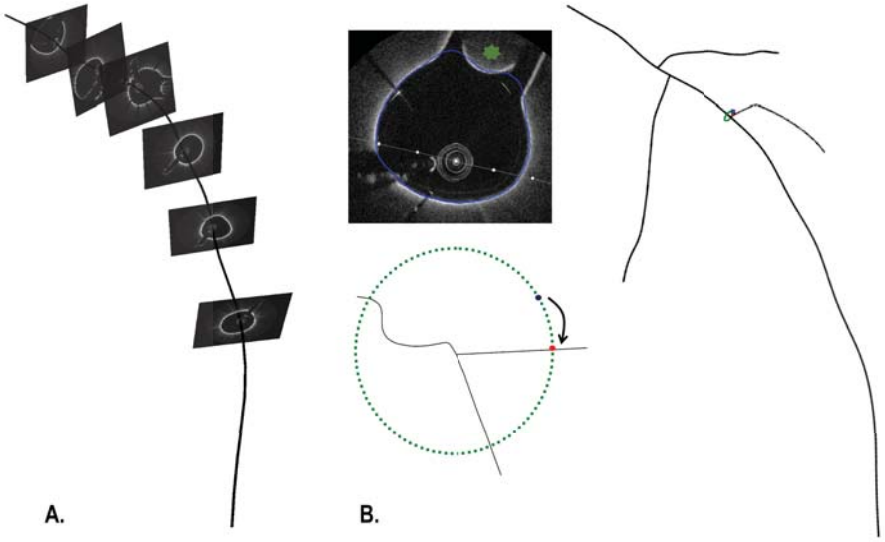

Figure 3.8 A: Alignment of optical coherence tomography (OCT) frames with the main branch centerline of the main branch. B: Manual selection of a marker (green star) for the side branch chosen as landmark for rotation of the lumen contour (in blue) and stent. The rotation was needed to superimpose the marker (initial position in blue) on the side branch centerline (final position in red).

3.4.2 3D geometry and fluid dynamic model

The 3D geometry was obtained with Rhinoceros v.5.0 (Robert McNeel and Associates, Seattle, WA, USA). In particular, the lumen surface was reconstructed starting from the aligned point cloud of the lumen contours. Lumen contour points were automatically interpolated with curves that were used for adapting a surface (i.e. through a lofting procedure).
The 3D stent geometry was reconstructed starting from the obtained point cloud of the stent struts with a morphing procedure (Fig.3.9A). The centerline of a free expanded 3.5x12 mm Multi-Link 8 stent (straight configuration) was extracted from μCT slices following the same procedure adopted for the phantom. The straight stent centerline was morphed into the deployed stent configuration using Hypermesh (Altair Engineering, Inc., Troy, MI, USA). Handles for mesh morphing were created on the centerline and moved on points that belong to the stent point cloud so that their distance was minimized (Fig.3.9B). The morphed centerline was imported in Rhinoceros and the 3D geometry of the stent was achieved by means of the graphical algorithm editor Grasshoper® (www.grasshopper3d.com). In particular, cross-section curves (i.e. squares with sides of 81 μm as the Multi-Link 8 stent strut cross-sections) were po-

sitioned on each ring and bridge (Fig.3.9C) and were used for lofting. The 3D

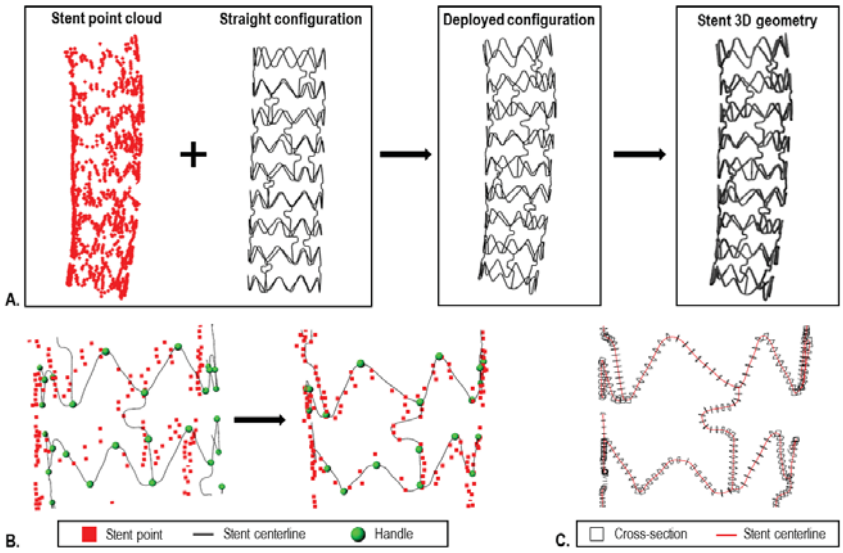

Figure 3.9 A: Alignment of optical coherence tomography (OCT) frames with the main branch centreline of the main branch. B: Manual selection of a marker (green star) for the side branch chosen as landmark for rotation of lumen contour (in blue) and stent. Rotation was needed to superimpose the marker (initial position in blue) on the side branch centerline (final position in red).

reconstruction Fig.3.10 was used to perform a proof-of-concept hemodynamic analysis on the actual LAD configuration after stent deployment (Fig.3.1). The fluid domain was discretized using 3,234,032 tetrahedral elements by means of ANSYS ICEM CFD v.16 (ANSYS Inc., Canonsburg, PA, USA).
The transient CFD analysis was performed using ANSYS Fluent v.16 (ANSYS Inc.). A typical human LAD flow waveform (Davies et al., 2006) was applied as a flat velocity profile to the inlet surface (Chiastra et al., 2013b). Its mean value in time was defined so that the flow rate was 45.15 ml min^{-1}, in agreement with the literature (Kessler et al., 1998). At the outlet surface a zero pressure condition was set. No slip-condition was applied to the arterial and stent walls, which were defined as rigid. The blood was modelled as an incompressible, non-Newtonian fluid using the Carreau model (Caputo et al., 2013). The blood density was set to 1060 kg m^{-3} (Kessler et al., 1998). The assumption of laminar flow was made as the maximum Reynolds number was $\backsim$157 at peak diastole. Solver settings are reported elsewhere (Chiastra et al., 2013b).

Figure 3.10 3D geometry provided by the proposed method. The arrow indicates the direction of the simulated blood flow.

3.4.3 Validation of the reconstruction

The 3D lumen reconstruction, which was obtained with the proposed OCT-based method, was validated against that from μCT scan, used as reference. In particular, the distance between the lumen surface of the OCT and μCT reconstructions was evaluated. Then, the surface area of OCT reconstruction with a distance greater than 0.25 mm from the reference lumen geometry was calculated (Chiastra et al., 2016). The relative error between the OCT and μCT reconstructions in terms of lumen volume was also computed. Furthermore, the point cloud for the stent obtained from OCT was compared with the stent centerline points from μCT by calculating the total distances between corresponding points.

3.5 Results

3.5.1 Validation of the segmentation algorithm

The Kruskal-Wallis test proved no statistical differences between lumen areas computed with the automatic and manual methods ($p > 0.05$). Linear

regressions reported strong correlation between area values, resulting in correlations coefficients of 0.999 ($p < 0.005$) for all the combinations considered (i.e. algorithm vs. reader 1, algorithm vs. reader 2 and reader 1 vs. reader 2) (Fig.3.11). The regression equations supported a significant linearity between datasets (Giavarina, 2015). The Bland-Altman diagrams of the agreement between sets of lumen area values are reported in Fig.3.12. The diagrams showed that the distribution of the differences in the lumen area values did not depend on the mean of the measurements among datasets. These distributions were featured by a mean of 0.29 mm^2 for the comparison automatic against reader 1, a mean of 0.26 mm^2 for the comparison automatic against reader 2, and a mean of -0.03 mm^2 for the inter-observer comparison. The 95% of the differences in lumen areas lied between -0.04 mm^2 and 0.61 mm^2 for the comparison automatic against reader 1, 0.032 mm^2 and 0.49 mm^2 for the comparison automatic against reader 2, and -0.41 mm^2 and 0.36 mm^2 for the inter-observer comparison, respectively. The resultant biases in the Bland-Altman diagrams corresponded to relative errors in lumen area values of 3.42% (Fig.3.12A), 3.15% (Fig.3.12B), and 0.31% (Fig.3.12C) with respect to the median area values of the reference region-of-interest. The similarity indexes evaluated from comparison between datasets are reported in Table 3.2.
The Kruskal-Wallis for the detected number of stent struts reported no statistical differences between datasets ($p > 0.05$). The Bland-Altman diagrams for the LOA are shown in Fig.3.13. These diagrams were featured by a mean of -17.43 μm, -17.73 μm, and -0.13 μm for the comparisons automatic against reader 1, automatic against reader 2 and reader 1 against reader 2, respectively. The 95% of the differences in LOA lied respectively between -41.83 μm and 36.01 μm for the comparison automatic against reader 1, -43.37 μm and 36.85 μm for the comparison automatic against reader 2, lastly -25.01 μm and 24.74 μm for the inter-observer comparison. The similarity indices evaluated from comparison between datasets are reported in Table 3.2.

3.5.2 Validation of the alignment and orientation method

Figs. 3.14A and 3.14B shows the superimposition between the 3D lumen geometry reconstructed with the OCT-based method and the reference geometry obtained from μCT. The percent difference in area between the OCT and μCT lumen reconstructions was 17.5%. As highlighted by the lumen cross-sections of Fig. 3.14A, the best coincidence between the lumen geometries was observed in the central region close to the SB used as landmark for twist angle estimation. The relative error of the lumen volume between OCT and μCT lu-

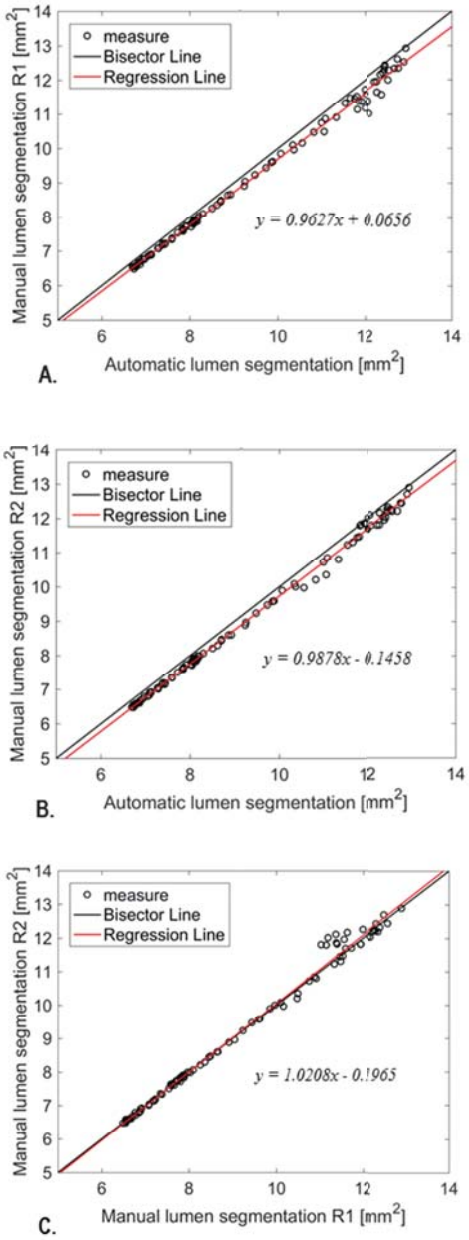

Figure 3.11 Linear regression of lumen areas with the regression equation. A: Automatic segmentation against manual segmentation made by reader 1. B: Automatic segmentation against manual segmentation made by reader 2. C: Inter-observer linear regression.

men reconstructions was 7.1%. In addition, a qualitative comparison between reconstructed 3D models with stent is reported in Fig. 3.14C and shows satisfactory geometrical consistency. The distribution of the total distances between points of the stents are reported in Fig. 3.15. The 1st, 2nd, and 3rd quantiles of

Table 3.2 Similarity indices for the segmentation of lumen and stent that were obtained from the indicated comparisons.

	Sensitivity	**Specificity**	**Jaccard index**	**Dice index**
Lumen				
Auto vs R1	$96.8 \pm 1.2\%$	$99.6 \pm 0.1\%$	$96.5 \pm 1.2\%$	$98.2 \pm 0.7\%$
Auto vs R2	$96.8 \pm 0.8\%$	$99.9 \pm 0.1\%$	$96.4 \pm 0.9\%$	$98.2 \pm 0.5\%$
R1 vs R2	$98.9 \pm 0.4\%$	$99.8 \pm 0.3\%$	$97.6 \pm 1.5\%$	$98.8 \pm 0.8\%$
Stent				
Auto vs R1	$91.7 \pm 13.2\%$	$77.8 \pm 28.2\%$	$78.1 \pm 17.7\%$	$86.5 \pm 12.8\%$
Auto vs R2	$93.5 \pm 12.3\%$	$72.9 \pm 33.6\%$	$77.6 \pm 18.6\%$	$86.0 \pm 13.6\%$
R1 vs R2	$96.5 \pm 7.8\%$	$89.4 \pm 18.0\%$	$89.2 \pm 13.7\%$	$93.6 \pm 9.0\%$

the total distances were 136.93 μm, 198.75 μm and 283.46 μm, respectively.

3.5.3 CFD simulation

Fig.3.16A shows the contour map of time-averaged wall shear stress (TAWSS) along the MB wall. The distal portion was characterized by higher values of TAWSS, which was in agreement with the reduced dimension of the lumen cross-section compared to the proximal segment. The region with low TAWSS (i.e, TAWSS$<$ 0.4 Pa), recognized as critical for the occurrence of ISR (Malek et al., 1999), was confined to the stent region. The percentage area of the stented MB portion exposed to low TAWSS was 48.2%. In Figs. 3.16B and 3.16C velocity contours with in-plane velocity streamlines are depicted at two selected locations at peak flow-rate. Velocity streamlines highlighted a disturbed flow at regions with stent malapposition.

3.6 Discussions

In this chapter it was presented a semi-automatic method to reconstruct the actual configuration of coronary arteries after stent implantation from OCT images. The algorithm was applied on a rigid phantom that resembled a segment of LAD with bifurcations and was used to acquire OCT images after stent deployment.
The fully automatic OCT segmentation procedure was validated against manual segmentation and provided good results as confirmed by high values of similarity indices and correlation coefficients. The obtained 3D reconstruc-

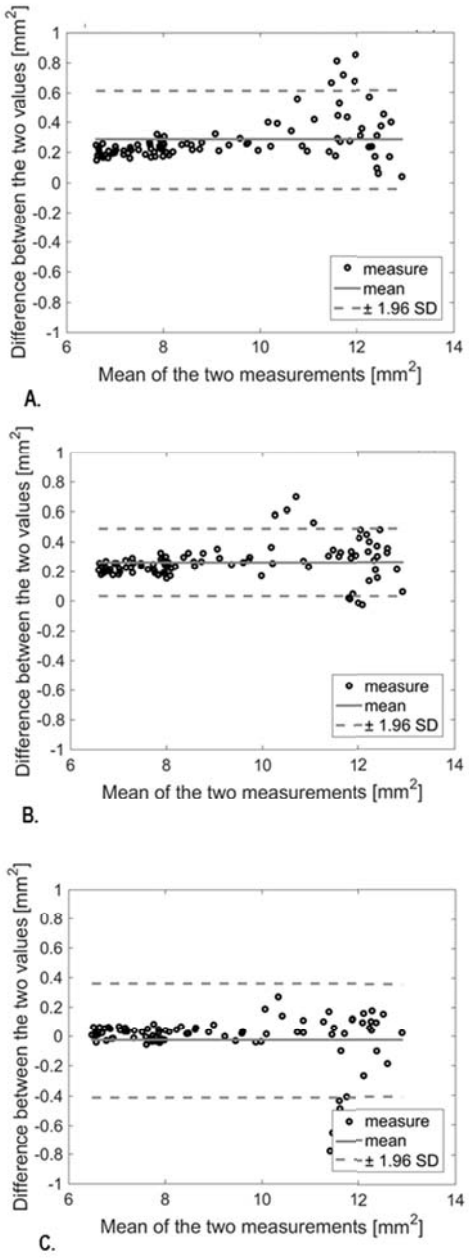

Figure 3.12 Bland-Altman diagrams for agreement analysis of lumen areas. A: Automatic segmentation against reader 1 segmentation. B: Automatic segmentation against reader 2 segmentation. C: Inter-observer agreement study.

tion of the stented phantom was compared with the geometry reconstructed from μCT scan, used as ground truth, demonstrating the incidence of distortion from catheter-based imaging techniques. Finally, the 3D reconstruction was

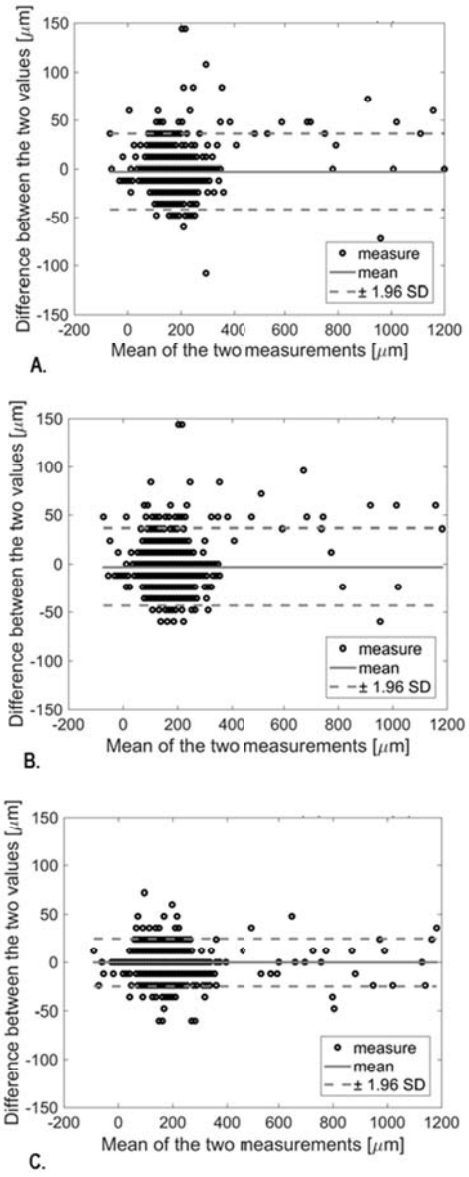

Figure 3.13 Bland-Altman diagram for agreement analysis of length of apposition (LOA). A: Automatic segmentation against reader 1 segmentation. B: Automatic segmentation against reader 2 segmentation. C: Inter-observer agreement study.

successfully used to investigate the local hemodynamics. The good outcomes obtained from validation procedure enables to state that the proposed reconstruction methodology is a promising tool for CFD analyses also on patient-specific stented geometries.

Results showed that the segmentation algorithm identified correctly the lumen

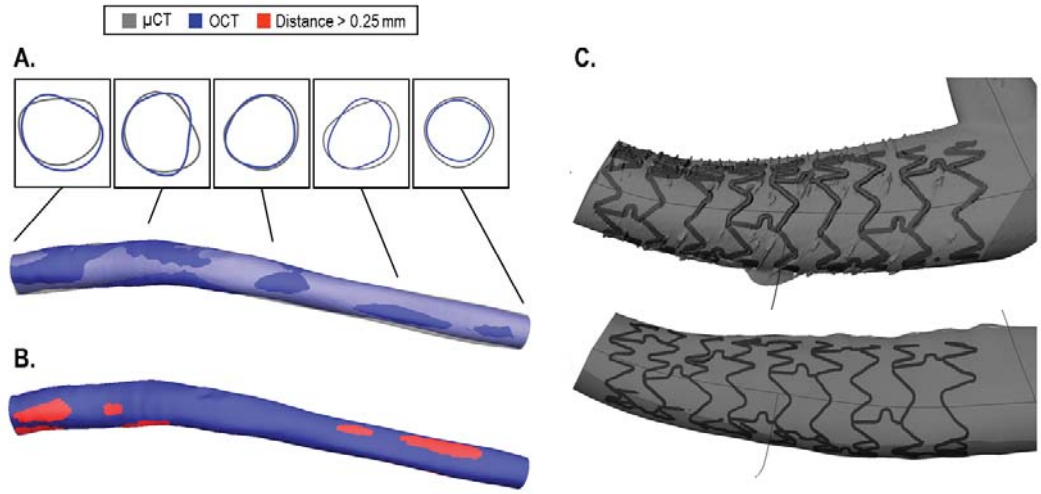

Figure 3.14 Comparison between the 3D reconstruction obtained using the OCT-based method and the 3D reference model reconstructed from μCT. A: Superimposition of the 3D lumen geometries provided by OCT (blue) and μCT (grey) data. B: Regions of the OCT vessel geometry exhibiting distances from the μCT reference greater than 0.25 mm. C: Qualitative comparison between the 3D stent geometry reconstructed from μCT (top) and that reconstructed with the OCT-based reconstruction method (bottom).

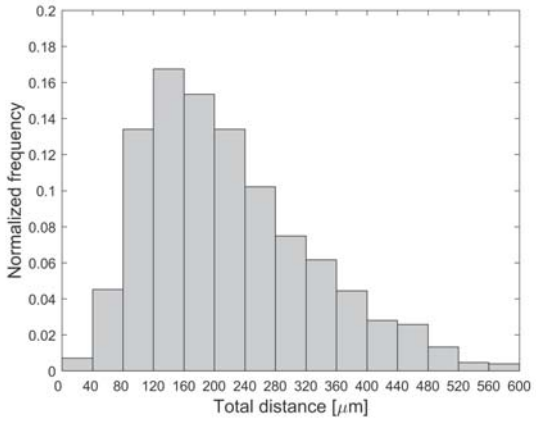

Figure 3.15 Histogram of the total distances between centreline points of the stents reconstructed using the OCT-based method and those provided by μCT data.

contours and provided a good stent identification. Indeed, similarity indexes for the lumen were close to 100% considering the manual segmentation per-

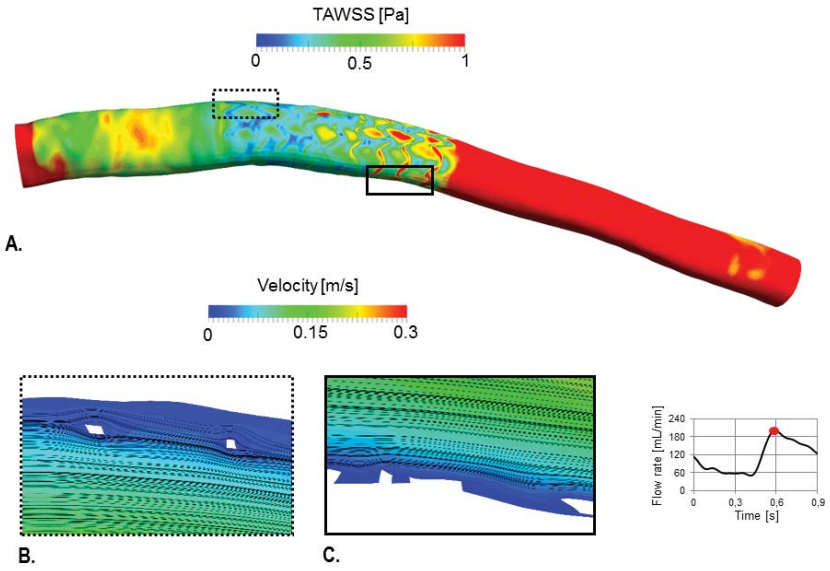

Figure 3.16 Results of the CFD analysis. A: Contour plot of time-averaged wall shear stress (TAWSS). B: Velocity contour with in-plane velocity streamlines at peak flow-rate at a cross-section characterized by malapposed struts. C: Velocity contour with in-plane velocity streamlines at peak flow-rate at a cross-section with apposed struts.

formed by the two image readers. In fact, the sets of computed lumen areas had strong linear correlations and good agreement. The resultant biases in the Bland-Altman diagrams were 3% of the lumen areas from manual segmentation and were comparable to values reported in previous studies (Celi and Berti, 2014; Chatzizisis et al., 2014; Macedo et al., 2016). Ranges with the 95% of the differences in lumen areas were smaller than those obtained in the works of Celi et al. (i.e. -1.2 mm^2 and 1.2 mm^2) (Celi and Berti, 2014) and Chatzizisis et al. (i.e. -1.6 mm^2 and 1.3 mm^2) (Chatzizisis et al., 2014). The similarity indexes for stent segmentation reported good stent detection. The average sensitivity of the algorithm for stent segmentation was in agreement with the work of Wang et al. (i.e. 94%) (Wang et al., 2013). The Bland-Altman diagrams for LOA reported no significant bias and smaller limits of agreement than those found by Ughi et al. (Ughi et al., 2012). (i.e. 80-85 μm).

The alignment and orientation procedure provided reliable 3D reconstruction of phantom MB and stent. In particular, discrepancies between lumen surfaces were larger distally to the reference SB due to the axial twist angle. Indeed, reference points in that vessel portion (i.e. bifurcation points) could not be de-

tected for estimation of the twist angle. Similar observations are valid for the stent reconstruction, since stent centroids were processed with the same alignment algorithm as the points belonging to the lumen contours. The median of total distances between the reconstruct stent centerline and the reference was comparable to twice the strut thickness.
The obtained 3D geometry allowed successfully running a CFD analysis. The local hemodynamics was investigated in a high fidelity geometry with respect to the real one, which enabled to distinguish apposed and malapposed stent struts as they were in the real case. Indeed, the considered hemodynamic indexes were in agreement with previous computational studies on image-based stented coronary arteries (Chiastra et al., 2013b; Ellwein et al., 2011). In particular, adverse values of TAWSS were located at stent struts and disturbed blood flow structures were caused by stent malapposition.
In general, the framework proposed in this study showed promising results concerning the accuracy of the obtained vessel 3D reconstruction and the feasibility of CFD analysis with the achieved geometry. The fundamental contribution of the described methodology is the reconstruction of a patient-specific stented coronary artery through images that are regularly acquired during PCI. The resultant high fidelity geometry allows to evaluate local hemodynamics alterations within coronary arteries after stent deployment, with outcomes that are peculiar of each clinical case. Therefore, the presented framework might be used by cardiologists as a tool during both pre-operative planning phase and post-operative follow-up windows, providing a knowledge of the regions most prone to ISR due to adverse WSS along the endothelium.
Although results supported the reliability of the presented framework, there are limitations. The developed reconstruction method was applied to a rigid phantom made of a polymeric material. Therefore, the OCT acquisition was not performed in nominal conditions and the images were featured by a higher brightness as compared to in vivo acquisitions. However, the image segmentation outcomes are not influenced because the automatic algorithm is based on grayscale gradients in each OCT frame. Second, it was not possible to use the two proximal SBs as landmark to improve the reconstruction because of the impossibility to clearly distinct those from the MB at the bifurcation carina. Third, the assumption made to sample the MB centerline according to the distance between OCT frames might compromise the accuracy when a vessel with significant tortuosity is reconstructed. Indeed, in those cases the alignment should be performed along the path followed by the OCT catheter during pull-back. Fourth, the implemented algorithm for stent strut detection is not applicable to bioresorbable stents, since OCT images do not present the same

features (i.e. black trailing shadows behind high intensity pixels) as when the implanted device is made of metallic material.

3.7 Conclusions

This Chapter presented a semi-automatic method to reconstruct the actual configuration of coronary arteries after stent implantation from OCT images. The algorithm was applied on a rigid phantom that resembled a segment of LAD with bifurcations and was used to acquire OCT images after stent deployment.
The fully automatic OCT segmentation procedure was validated against manual segmentation and provided good results as confirmed by high values of similarity indices and correlation coefficients. The obtained 3D reconstruction of the stented phantom was compared with the geometry reconstructed from μCT scan, used as ground truth, demonstrating the incidence of distortion from catheter-based imaging techniques. Finally, the 3D reconstruction was successfully used to investigate the local hemodynamics.
The good outcomes obtained from validation procedure enables to state that the proposed reconstruction methodology is a promising tool for CFD analyses also on patient-specific stented geometries.

Chapter 4

Patient-specific models of coronary arteries with metallic stent: from in-vivo medical images to CFD simulations

This chapter describes the computational fluid dynamic analyses that were performed to assess the coronary hemodynamics of patients treated with metallic stents.The work was carried out in collaboration with the Institute of Cardiology, Catholic University of the Sacred Heart of Rome (Italy) and with the Northern General Hospital, Sheffield Teaching Hospitals NHS Foundation Trust, Sheffield (UK).

4.1 Introduction

THE validated reconstruction methodology described in Chapter 3 was employed to achieve high fidelity 3D models of three patients' diseased coronary arteries that underwent PCI and the insertion of a metallic scaffold at the Institute of Cardiology, Catholic University of the Sacred Heart of Rome (Italy).
Patients' hemodynamics was simulated by means of information that was obtained from medical images and results showed the effects of patient-specific flow conditions. The anatomical environment represents an impediment for the collection of flow measurements within coronary arteries, therefore the definition of patient-specific CFD boundary conditions is an open challenge for the scientific community. Several strategies are commonly used to model the hemodynamics within the reconstructed vessel and the surrounding environment but the literature lacks of studies about the sensitivity of CFD models to the variabilities of the imposed boundary conditions.
In this scenario, an uncertainty analysis of CFD boundary conditions was performed on one case and results did not report sensible differences in the distribution of WSS. The work was carried out in collaboration with University College London and aimed to compare the effects of such CFD models on the results, focusing on the specific interest in wall shear stresses.
This analysis sought to provide a contribution towards the development of fully patient-specific CFD models, both concerning the anatomic reconstruction and the peculiar hemodynamics. The lack of in-vivo measurements is due to the prohibitive position of coronary arteries, as well as the strong and periodic deformations of the vessels. Additionally, the relevance of this collaborative work is motivated by the lack of similar studies at coronary arterial tree with stented bifurcations in the literature. For instance, Sankaran and co-authors (Sankaran et al., 2016) described an uncertainty analysis of CFD boundary conditions to model the blood flow in an artery tree that was reconstructed from CT scan. The reconstruction included an occlusion at the left anterior descending (LAD) coronary artery without an intravascular scaffold.
Moreover, it is here described the application of the developed framework for the analysis of the blood flow after the treatment of an occluded left main coronary artery (LMCA) - LAD bifurcation with one stent. The PCI procedure was performed at the Northern General Hospital, Sheffield Teaching Hospitals NHS Foundation Trust, Sheffield (UK).
Occlusive unprotective left main coronary artery (ULMCA) disease is a high-risk condition, as it is responsible for the supply of the myocardium(Borges

et al., 2017). This pathology is registered for the 5% - 10% of the cases. The preferable treatment has been coronary artery bypass grafting (CABG) since the 1970s and when PCI techniques were in the first stages of development (Sheiban et al., 2009). The introduction of bare-metal stents gave ambiguous results because of the high rate of in-stent restenosis and the relative mortality rates of the 40%. Drug-eluting stents were designed to overcome such barrier by reducing the inflammatory reactions and smooth cell proliferation over the scaffold.

Several clinical trials were carried out to compare the outcomes of PCI and CABG for the treatment of ULMCA. For instance, the Synergy Between PCI With TAXUS and Cardiac Surgery (SYNTAX) trial aimed to evaluate the intervention strategy for cases affected by multivessel CAD or ULMCA disease with randomisation to CABG or PCI with the implantation of TAXUS stent (Boston Scientific). The primary end-point (i.e. death, stroke, repeat revascularisation) after 12 months was registered for the 17.8% of the patients in the PCI group and for the 12.4% in the CABG group. Therefore, results of SYNTAX trial confirmed the superiority of CABG over PCI for the treatment of ULMCA for the analysed population (Morice et al., 2010). Different outcomes were recorded from the Evaluation of XIENCE Versus Coronary Artery Bypass Surgery for Effectiveness of Left Main Revascularization (EXCEL) trial (Stone et al., 2016). It was a multicenter trial which randomised patients with ULMCA to PCI with XIENCE™ stents (Abbott Vascular) against CABG. The complete revascularisation of the ischeamic tissue was found in the majority of cases and data from ultrasound assessment supported the advantages of stent implantation.

Clinical trials provided evidences that did not prefer either PCI or CABG as optimal management of ULMCA disease. Indeed, mild mortality and primary end-point differences were registered between study groups. The evolution of stent manufacturing has recently been moving toward the design of dedicated bifurcation stents, as well al specific designs for the left main bifurcation (Borges et al., 2017) and innovative intervention procedures. Morris and co-workers (Morris et al., 2018) studied the stent expansion and repeat PCI in the simultaneous kissing stents (SKS) technique for the treatment of left main stem bifurcation. Briefly, SKS involves the deployment of two equal-sized stents at a bifurcation, one for the main branch and the second for the side branch. Then, the stents were adjacent at the proximal main branch (Sharma et al., 2004) and artificially anticipate the bifurcation. The main findings of the study were the growth of a continuous sheet at the artificial carina and the reduced restenosis, which were consistent with the computational results.

4.2 Methods

4.2.1 3D geometry reconstruction

In Table4.1 is listed the information about the treated coronary segments of the first three patients (i.e. Case 1, Case 2 and Case 3), with the design and size of the implanted stent. In particular, the stent size is reported as nominal external diameter and length. Whereas, the size of the stent strut cross-section is reported as diameter for circular-shaped struts and as side length for square-shaped struts. One XIENCE Sierra (Abbott) 4x38 mm stent was deployed in the left main bifurcation of Case 4, which was in overlapping with a Ultimaster (Terumo) 3.5x18 mm stent at the left anterior branch.
The treated blood vessels were reconstructed from angiograms and OCT images with the method described in Chapter 3. In particular, angiographic images were elaborated with a commercial software (CAAS, PIE Medical Imaging) to obtain the centreline of the treated vessel with bifurcations. This last was used to reconstruct the 3D main branch with the implanted stent from the processed OCT images. The side branches were reconstructed from information achieved with a 3D-QCA that was carried out with CAAS (PIE Medical Imaging). Essentially, the SB circular-shaped cross-section was created by scaling the MB cross-section area to preserve the ratio between MB and SB cross-section areas of the 3D-QCA geometry. The length of each side branch was 2.5 times the SB cross-section diameter.

4.2.2 CFD analyses

The hemodynamics of the first three cases of study (i.e. Case 1, Case 2 and Case 3) was estimated with a transient computational fluid dynamic (CFD) simulation performed with ANSYS Fluent v18.2 (Ansys Inc., Canonsburg, PA, USA). Whereas, the blood flow of Case 4 was analysed with a transient computational fluid dynamic (CFD) simulation that was performed with ANSYS CFX v19 (Ansys Inc., Canonsburg, PA, USA) at University College London. A preliminary CFD analysis did not report sensible differences in the results between the two software in terms of WSS distribution.
The fluid dynamic domain was discretised in tetrahedral elements with ANSYS ICEM (Ansys Inc., Canonsburg, PA, USA) and the smallest element size was

approximately one fourth of the strut thickness. In Fig.4.1 the 3D geometries and cross-sections of the mesh are shown, with the strut cross-sections highlighted with an arrow. The mesh size allowed a good characterisation of the blood flow at both stented and side branch regions, it was defined according to a mesh independence study that was performed in previous computational fluid dynamics works, such as in (Chiastra et al., 2013b). A coupled solver was used with a second-order upwind scheme for the momentum spatial discretization and second-order implicit scheme for the time. The flow Courant number was set to 50. The under-relaxation factors were set to 0.3 for the pressure and the momentum and to 1 for density. Convergence criterion was set to 10^{-5} for continuity and 10^{-6} for velocity residuals. A time step of 0.009 s was chosen for running the simulations (100 time steps were necessary for one cardiac cycle). (Chiastra et al., 2016). The blood was described as an incompressible non-Newtonian fluid, implementing a Bird-Carreau constitutive law with μ_∞=0.0035 kg m^{-1} s^{-1}, μ_0=0.25 kg m^{-1} s^{-1}, k=25 s, n=0.25 and density of 1060 kg m^{-3} (Caputo et al., 2013).
In Tab.4.2 the information about the computational model is listed, with the size of the grid, the mean inflow rate and the outflow split condition.

Table 4.1 Details of the treated coronary artery segment and implanted stent. The length of the reconstructed main branch (MB) and number of side branches (SBs) are reported. The stent size is reported as nominal external diameter and length. The size of the stent strut cross-section is reported as diameter for circular-shaped and as side length for square-shaped struts.

Cases	Case 1	Case 2	Case 3
Treated coronary artery	LAD	RCA	RCA
MB length $[mm]$	47	50	53
Number of SBs	1	1	3
Implanted stent $[mm]$	Resolute Integrity (Medtronic) 3.5 x 18	Xience Prime (Abbott) 3.5 x 28	Nobori (Terumo) 3.5 x 24
Stent cross-section size $[mm]$	diameter=0.91	length=0.81	length=0.125

The imposed boundary conditions were computed from available information about the patient-specific blood flow conditions, as mentioned in Section2.6.1. The flow profiles that were imposed at the inlets resembled the typical left and right coronary artery pulsatile flow waveforms (Davies et al., 2006;

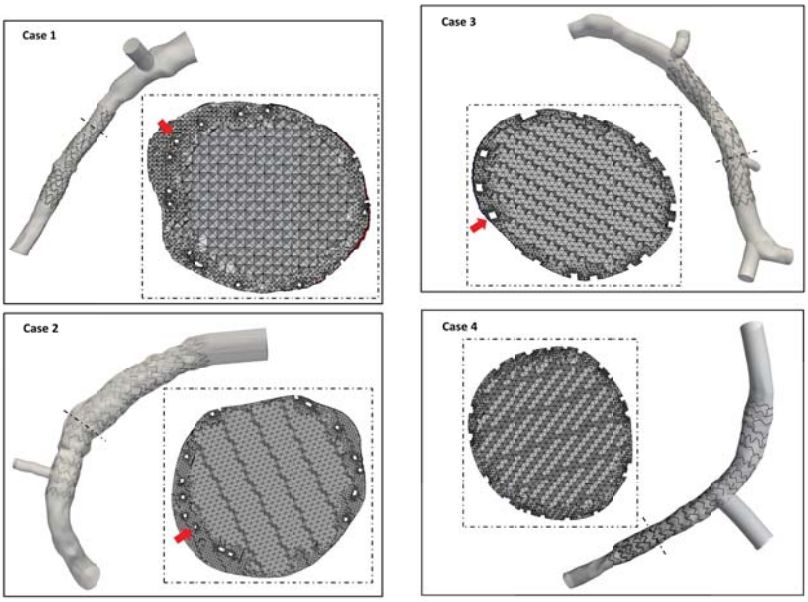

(a) (b)

Figure 4.1 3D reconstructions and cross-section of the volume mesh of the studied cases, respectively Case 1, Case 2 (a), Case 3 and Case 4 (b). The stent struts cross sections, eventually in malapposition, are depicted with a raw.

Hadjiloizou et al., 2008) and had mean values that were computed from the flow of the radio-opaque liquid injected during angiography, in agreement with a method proposed in the literature (Sakamoto et al., 2013).
Geometric characteristics of each 3D geometry were used to obtain the corresponding flow-split conditions at the outlets, implemented with the relationship proposed by van der Giessen (Van der Heiden et al., 2013). The surfaces of the blood vessel and stent were rigid and no-slip settings were imposed as boundary conditions. Details about the solver settings are available in (Chiastra et al., 2013b). In Table4.2 the boundary conditions that were imposed to the CFD model specific for each patient are listed, including the grid dimension and the boundary conditions at the inlet, distal main branch and side branch respectively.
For each case, the velocity field within the domain was evaluated at the peak of flow rate. Then, the pattern of TAWSS averaged over the entire cardiac cycle was assessed, focusing on regions under values of TAWSS considered as potential trigger for complications, such as ISR, that is TAWSS $\leqslant$ 0.4 Pa. Moreover, the percentages of the lumen surface area that were exposed to intervals

Table 4.2 Information of the implemented CFD model for cases' hemodynamic assessment.

Cases	Number of elements	$\mathbf{Q}_{inlet}$ $[ml\ min^{-1}]$	Flow split ratios
Case 1	$2.291 \cdot 10^6$	127.44	0.55:0.45
Case 2	$5.958 \cdot 10^6$	85.68	0.94:0.06
Case 3	$6.826 \cdot 10^6$	91.96	0.33:0.28:0.05:0.33
Case 4	$6.879 \cdot 10^6$	50	0.4:0.6

of TAWSS between 0 Pa and 3 Pa were computed. Such plot provides quantitative information about the global spectrum of the wall shear stresses at the endothelium.

Evaluation of the effects of CFD boundary conditions

The Case 3 was selected for the study, the CFD simulations were carried out with ANSYS CFX v19 (Ansys Inc., Canonsburg, PA, USA). The uncertainty analysis comprised the application of the models for outflow estimation that were proposed by Murray (Murray, 1926), van der Giessen (Van der Giessen et al., 2011), Huo and Kassab (HK) (Huo et al., 2009), and zero pressure conditions. Such models implement the relationship between the ratio of bifurcation branches and local flow split condition. As mentioned in Section2.6.1 :

$$\frac{q_{D2}}{q_{D1}} = \left(\frac{d_{D2}}{d_{D1}}\right)^{\alpha} \tag{4.1}$$

where q_{D1} and q_{D2} are the outflow rate at the branch with larger and smaller diameter, respectively d_{D1} and d_{D2}. Whereas, the value of α depends on the formula that be considered:

- van der Giessen: $\alpha = 2.27$
- Murray's law: $\alpha = 3$
- HK model: $\alpha = 2.33$

Additionally, the effect of the assumption of Newtonian fluid (μ=0.0035 kg m^{-1} s^{-1}) on the results was evaluated.
The patient-specific flow condition that was implemented in Chapter 4 was used as reference for the results comparisons. In Tab.4.3 were listed the implemented

boundary conditions, where the reference CFD model had boundary conditions reported as Set 0, the studied models were labelled Set 1, Set 2 and Set 3.

Table 4.3 Information of the implemented CFD model for cases' hemodynamic assessment.

Sets	$\mathbf{Q}_{inlet}$ $[ml\ min^{-1}]$	**Outflow conditions**
Set 0 (van der Giessen model)	91.96	0.30:0.32:0.07:0.3
Set 1 (HK model)	91.96	0.28:0.34:0.09:0.29
Set 2 (Zero pressure)	91.96	P= 0 Pa
Set 3 (Murray model)	91.96	0.34:0.27:0.04:0.35

4.3 Results and discussions

Results obtained from the fulfilled CFD simulations of each case were reported as follows. Firstly, the velocity streamlines at peak of flow rate were shown, so that flow recirculation and the influence of the stent were presented. Secondly, the contour map plots pictured the distribution of TAWSS along the arterial wall averaged over the simulated cardiac cycle. Moreover, the area percentages of the scaffolded lumen surface under TAWSS below 3 Pa, seeking to present a quantitative plot of the resultant distribution including a wide spectrum of values (Wentzel et al., 2012). Finally, the area percentage values of the scaffolded main branch segment that underwent TAWSS $\leqslant$0.4 Pa were reported, considered as critical for the occurrence of ISR (Malek et al., 1999).
Results from the simulated hemodynamics of Case 1 are reported in Fig.4.2 and Fig. 4.3. In particular, in Fig.4.2A the roughness of the lumen surface and malapposed stent strut induced small recirculation at the wall. In such regions the distribution of TAWSS was mainly below $\sim$0.7 Pa, as well as at the proximal region where the lumen cross-section area enlarged, as reported in Fig.4.2B-C. The 19.73$\%$ of the scaffolded main branch segment underwent TAWSS $\leqslant$0.4 Pa. The 3D shape of the main branch and the malapposed stent struts induced flow recirculation and stagnation, as shown in Fig.4.3A. Such region is characterised by RRT above 20 Pa^{-1} (Fig.4.3D), due to both low TAWSS and high OSI as reported in Fig.4.3B-C. The 1.39$\%$ of the superficial area of the stented segment was under critical values of OSI (i.e. above 0.1), whereas an area of 1.18$\%$ was characterised by RRT$\geq$20 Pa^{-1} (Himburg et al., 2004). Therefore, it can be argued that the deployment of the stent recovered the physiological

blood flow, however the malapposed stent segment caused disruption of the flow which might lead to long-term complications.

Results from the simulated hemodynamics of Case 2 are reported in Fig.4.4 and Fig. 4.5.In Fig.4.6A the surface roughness and the vessel curvature affected the flow pattern by causing larger localized recirculation than in Case 1. Fig.4.6A-C pictured the distribution of TAWSS at the scaffolded region, which was characterised by values below $\sim$0.3 Pa. The 39.47% of the scaffolded main branch segment underwent TAWSS $\leqslant$0.4 Pa. The vessel curvature, the stent mallapposition and the superficial roughness of the lumen confirmed to be crucial factors for the local post-operative flow. The streamlines of the velocity at peak of flow rate experienced strong recirculation in Fig.4.5A at the displayed vessel segment. High values of RRT mirrored the areas that were exposed to critical and oscillatory TAWSS, as shown in Fig.4.5B-D. The 1.89% of the superficial area of the stented segment was under critical values of OSI (i.e. above 0.1), whereas an area of 2.25% was characterised by RRT$\geq$20 Pa^{-1}.

Results from the simulated hemodynamics of Case 3 are reported in Fig.4.6, Fig.4.7, Fig.4.8 and Fig.4.9. In Fig.4.6A the smooth lumen surface and the well apposed stent struts gave a flow stream without superficial recirculation. The distributions of TAWSS in Fig.4.6B-C presented mainly values above $\sim$1 Pa. The 13.72% of the scaffolded main branch segment underwent TAWSS $\leqslant$0.4 Pa. The resultant superficial fluid dynamic quantities revealed a well recovered flow, the good stent apposition and the smooth lumen surface were favourable for the post-operative flow conditions. The stented lumen surface that underwent critical OSI and RRT was $\sim$1.15%, which was mainly localised at the stent struts edges. In Fig.4.7 the distributions of TAWSS that resulted from the tested outflow assumptions were reported. The Set 3 (i.e. Murray model) appeared to slightly overestimate the values of wall shear stress respect to the other models. Similar results were found for the velocity magnitude reported in Fig.4.8 and Fig.4.9. However, the overall TAWSS distributions reported differences as mean relative error between area percentages of about 1.1% for the Set 1, 0.23% for the Set 2, 2.9% for the Set 3 and 0.5% for the Set 4. Such results might be addressed to the peculiar symmetric flow split at the distal outlets, which was due to the comparable dimensions. Therefore, it can be argued that for this particular case, 3D shape of the treated coronary artery segment, the choice of the mathematical model for flow conditions at the outlets did not affect the analysis.

Results from the simulated hemodynamics of Case 4 are reported in Fig.4.10 and Fig.4.11. In Fig.4.10A the velocity streamlines were affected by the vessel bending at the scaffolded segment, as well as by the local lumen enlargements

which caused flow recirculation. The in-plane flow pattern displayed the interaction between the flow and the stent struts at the bifurcation. In Fig.4.10B-C the distribution of TAWSS at the scaffolded region was mainly below 0.7 Pa, which was directly related to the reduced flow velocity. Critical TAWSS values ($\leqslant$ 0.4 Pa) were found in the 42.65$\%$ of the scaffolded main branch. The local vessel enlargement at the bifurcation caused strong flow recirculation, as reported in 4.11A. The distribution of OSI confirmed the high TAWSS oscillation at such region, which was reflected by the extension of RRT$\geq$20 Pa^{-1} as shown in 4.11B-D.

4.4 Conclusion

The medical images that were acquired in-vivo after three PCI procedures were elaborated to obtain high fidelity coronary artery reconstructions and to simulate the blood flow. The patient-specific geometries were achieved with the methodology described in Ch.3. Then, patients' hemodynamics was simulated by taking into account the peculiar blood flow rate, estimated from the angiography acquisitions, and the geometrical features of the specific coronary anatomic dimensions, such as MB cross-section area and outlets diameters (Section 2.6.1).

The results were elaborated to present a picture of the flow stream at peak of flow rate and the distribution of TAWSS after one cardiac cycle. The latter was quantified by computing the percentage area under TAWSS between 0 Pa and 3 Pa at intervals of 0.1 Pa. The variation in time of the WSS was quantified by means of the oscillatory index (OSI) and the relative residence time (RRT). The extension of critical values of OSI ($\geq$0.1) and RRT ($\geq$20 Pa^{-1}) (Himburg et al., 2004) reported the crucial role of the 3D shape of the treated coronary artery bifurcation, as well as the degree of stent apposition. Indeed, the superficial roughness and bending of the vessel lumen induced local flow recirculation, which were enhanced where the stent struts were far from the lumen surface. Results from the CFD simulation of Case 3 presented a limited dependency on the relationship used to model the outflow conditions. This was related to the peculiar quasi-symmetric flow partition along the treated vessel segment.

This Chapter illustrated the use of a patient-specific technique to model blood flow in a stented left main coronary artery bifurcation. The consistency that was found in the literature (Morris et al., 2018) between the computed hemodynamics and the main clinical findings at follow-up confirmed the potentiality of computational simulations as valuable predictors for procedure outcomes. The

described approach provided valuable complementary information for support the management of occluded LMCA.
Nevertheless, the accuracy of the study is affected by some limitations that were introduced to the reconstruction and the fluid dynamic model. The main limitation of the reconstruction methodology was due to the distortions of the OCT images. Indeed, the pull-back was not gated by electrocardiography (ECG), therefore the vessel deformations induced by heart contractions were not minimised. Consequently, the MB appeared crushed in some regions. This phenomenon is an open issue due to the lack of validating data about the actual geometry and cross section tapering of coronary tree branches. Concerning the simulation of patients' hemodynamics, the assumption of rigid wall might have affected the accuracy of the results. Fluid structure interaction simulations of coronary artery models, without the stent, were performed in a limited number of studies (Gamage et al., 2018; Kafi et al., 2017; Torii et al., 2009).

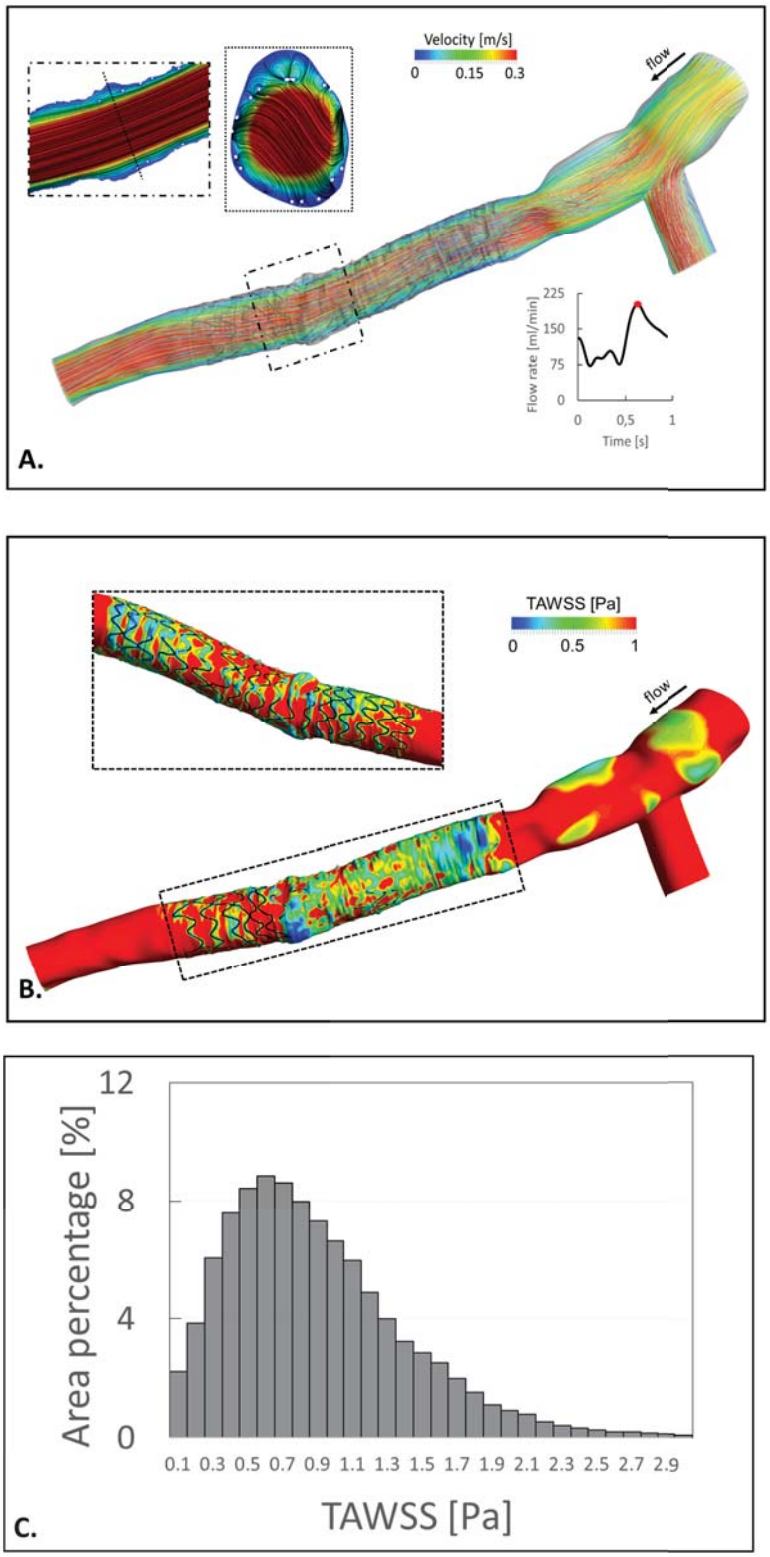

Figure 4.2 Results from the simulated flood flow of Case 1.A: Streamlines of the velocity coloured by the velocity magnitude and the in-plane velocity contour-map with in-plane streamlines at peak for flow rate. B: Contour map of the time-averaged wall shear stress (TAWSS) at the end of the simulated cardiac cycle with an enlargement of the opposite view of the bifurcation. C: Histogram of the scaffolded surface percentage area under intevals of TAWSS.

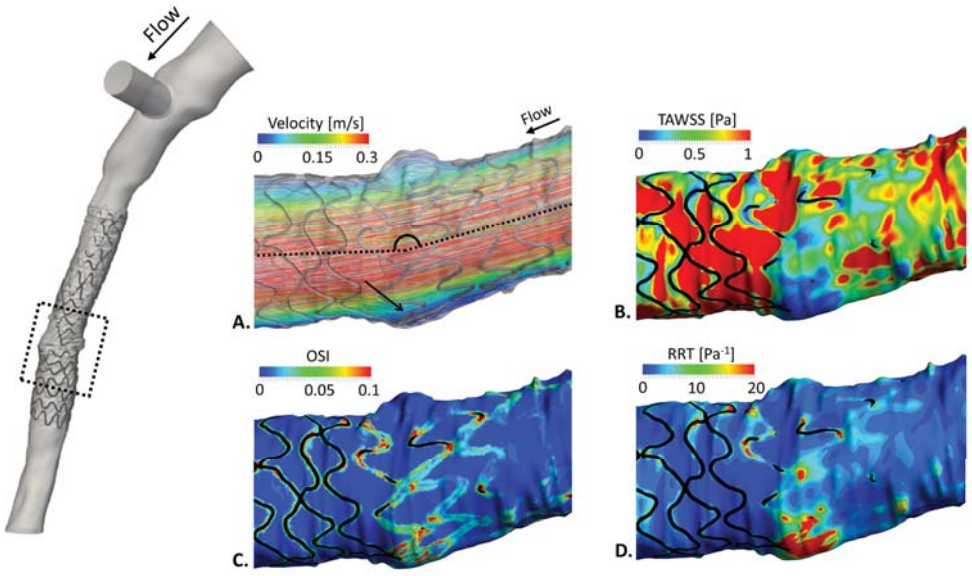

Figure 4.3 Distributions of the superficial hemodynamics quantities of Case 1 at the segment defined by the dotted rectangle. A: Streamlines of the velocity coloured by the velocity magnitude, the arrow depicts the flow recirculation at the bending of the vessels . B: Contour map of the time-averaged wall shear stress (TAWSS) over the simulated cardiac cycle. C: Contour map of the oscillatory index (OSI) that was computed over one cardiac cycle. D: Contour map of the residual residence time (RRT) computed over one cardiac cycle.

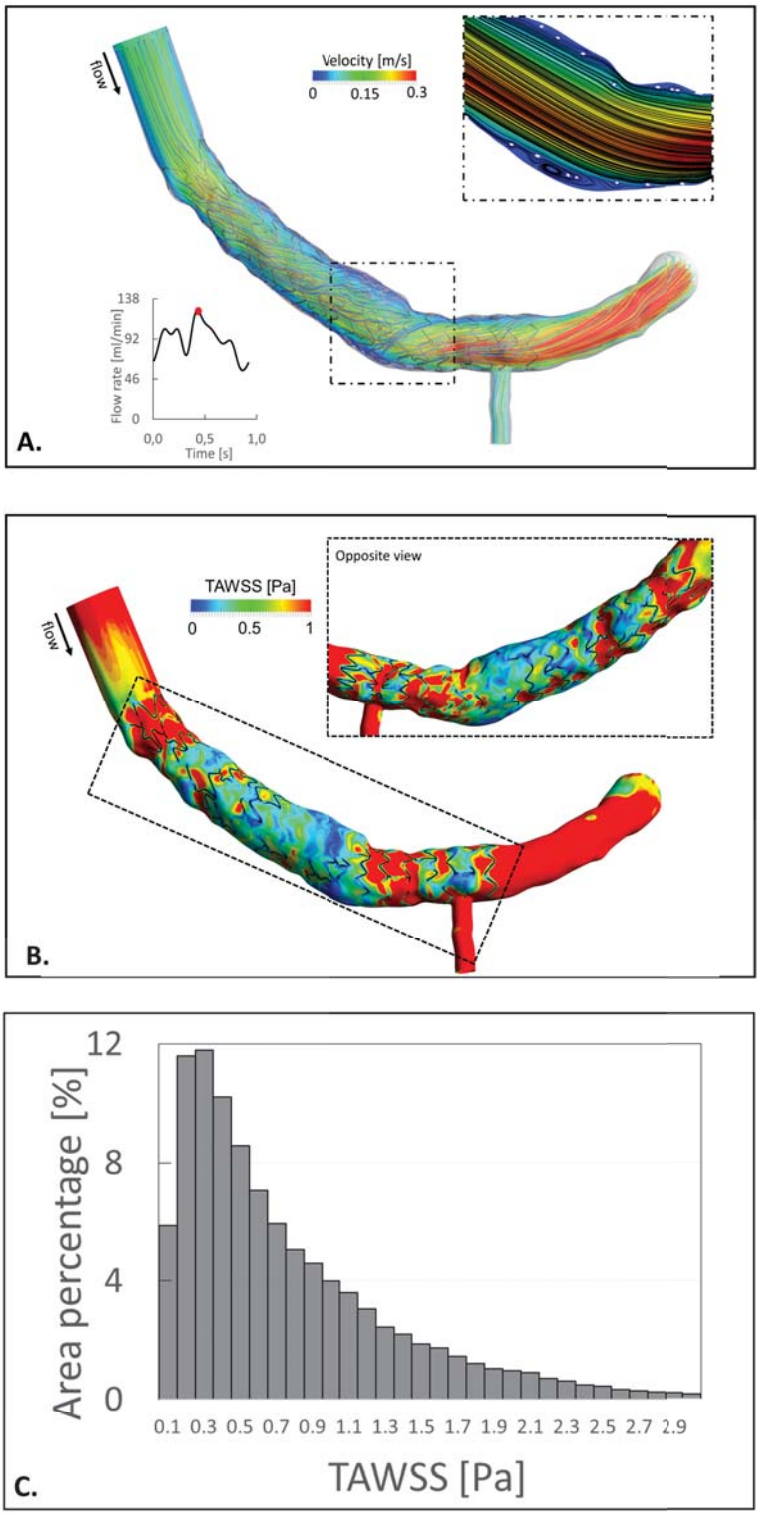

Figure 4.4 Results from the simulated flood flow of Case 2.A: Streamlines of the velocity coloured by the velocity magnitude and the in-plane velocity contour-map with in-plane streamlines at peak for flow rate. B: Contour map of the time-averaged wall shear stress (TAWSS) at the end of the simulated cardiac cycle with an enlargement of the opposite view of the bifurcation. C: Histogram of the scaffolded surface percentage area under intervals of TAWSS.

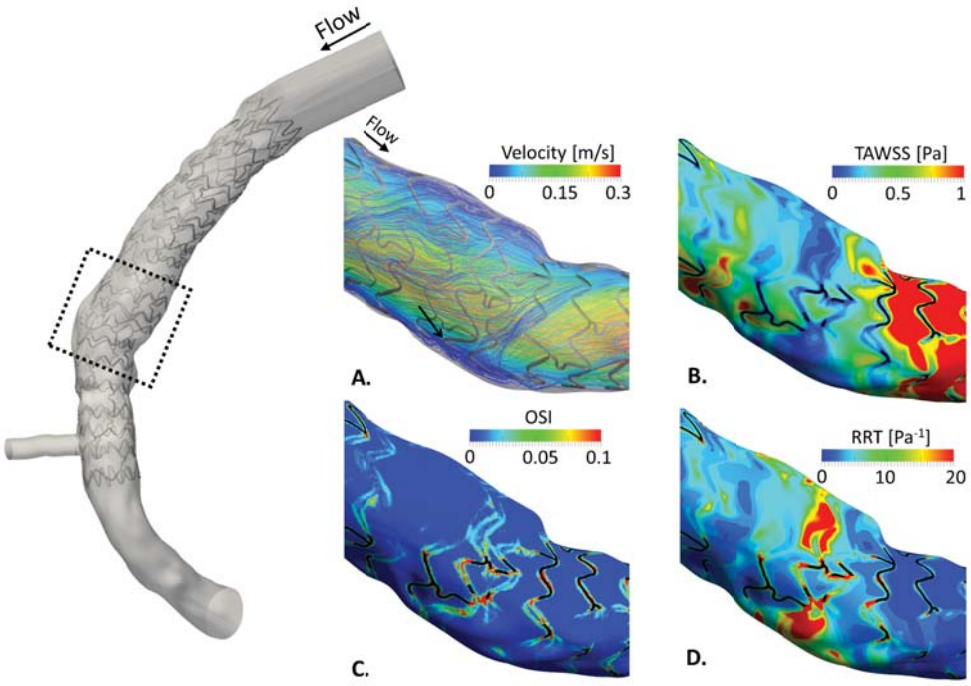

Figure 4.5 Distributions of the superficial hemodynamics quantities of Case 2 at the segment defined by the dotted rectangle.A: Streamlines of the velocity coloured by the velocity magnitude, the arrow depicts the flow recirculation at the bending of the vessels. B: Contour map of the time-averaged wall shear stress (TAWSS) over the simulated cardiac cycle. C: Contour map of the oscillatory index (OSI) that was computed over one cardiac cycle. D: Contour map of the residual residence time (RRT) computed over one cardiac cycle.

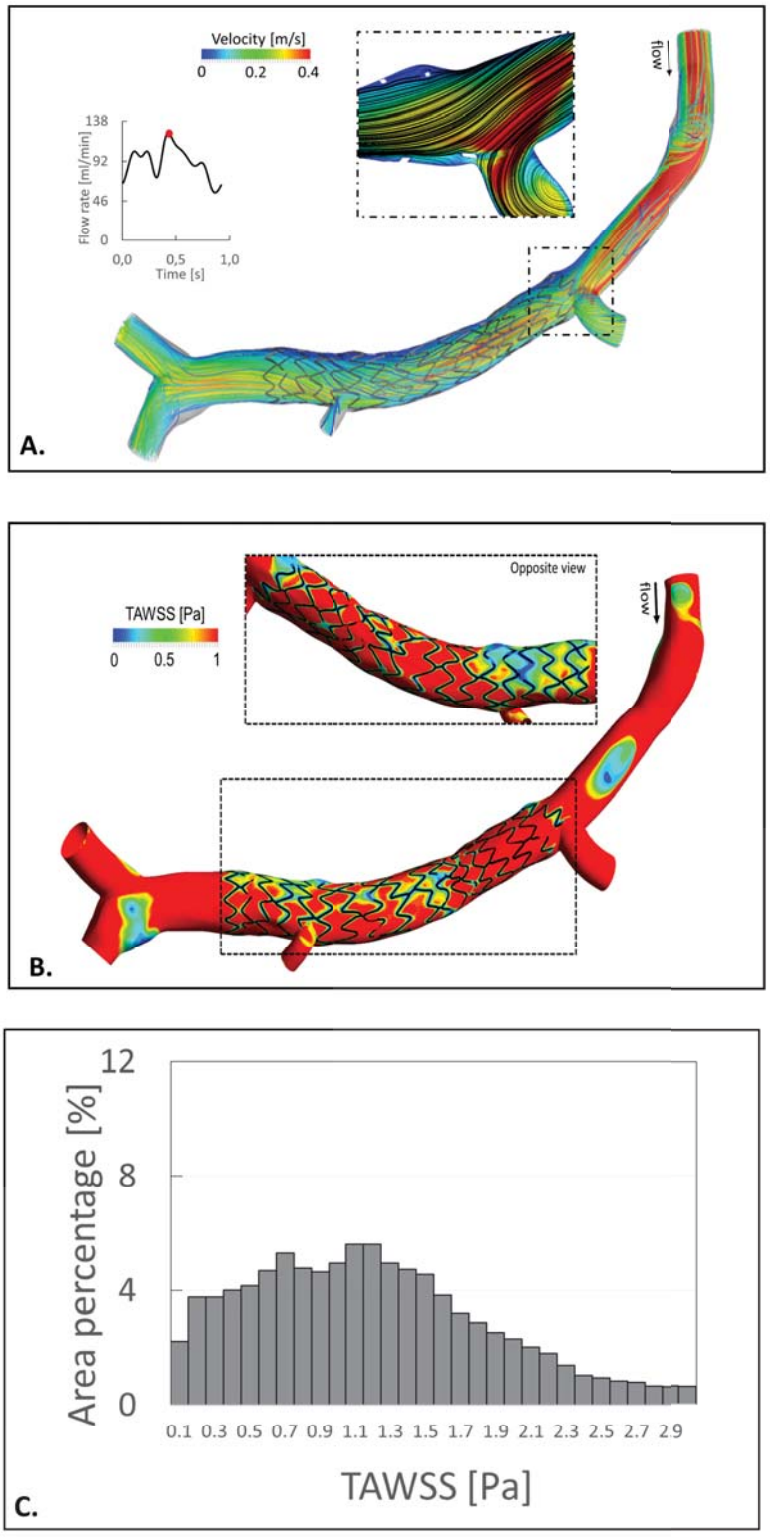

Figure 4.6 Results from the simulated flood flow of Case 3.A: Streamlines of the velocity coloured by the velocity magnitude and the in-plane velocity contour-map with in-plane streamlines at peak for flow rate. B: Contour map of the time-averaged wall shear stress (TAWSS) at the end of the simulated cardiac cycle with an enlargement of the opposite view of the bifurcation. C: Histogram of the scaffolded surface percentage area under intervals of TAWSS.

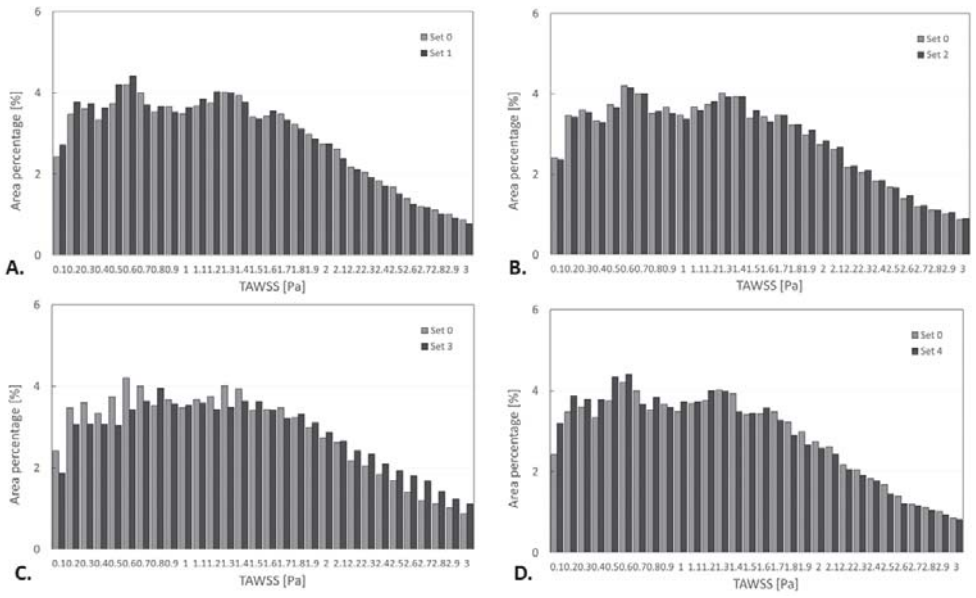

Figure 4.7 Histograms of the scaffolded surface percentage area under intervals of TAWSS from 0 Pa and 3 Pa.

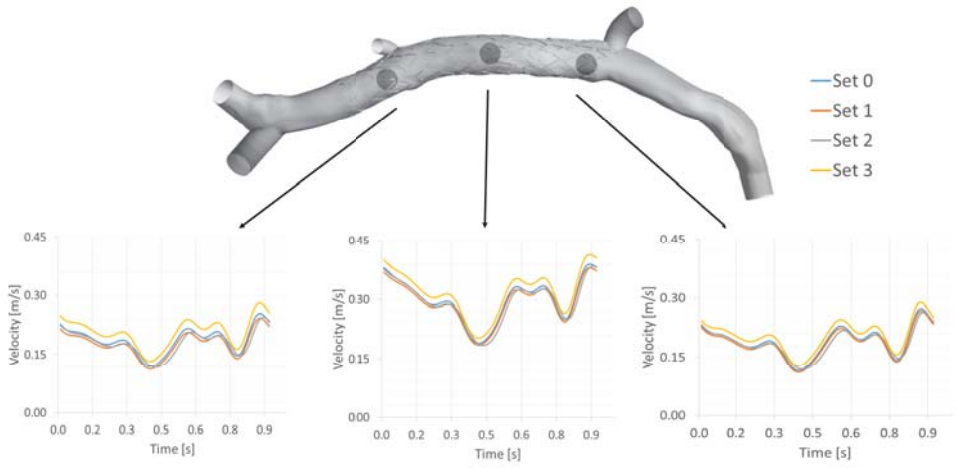

Figure 4.8 Curves of the velocity magnitude in time at three points in the scaffolded segment.

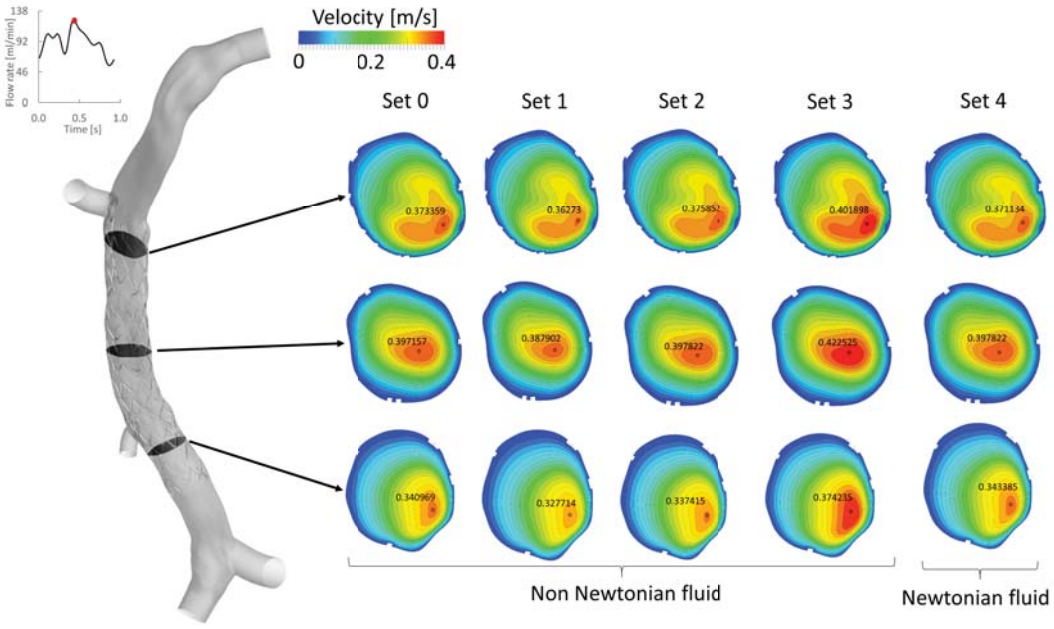

Figure 4.9 In-plane contour plot of the velocity magnitude at peak of flow rate at three cross-sections in the scaffolded segment

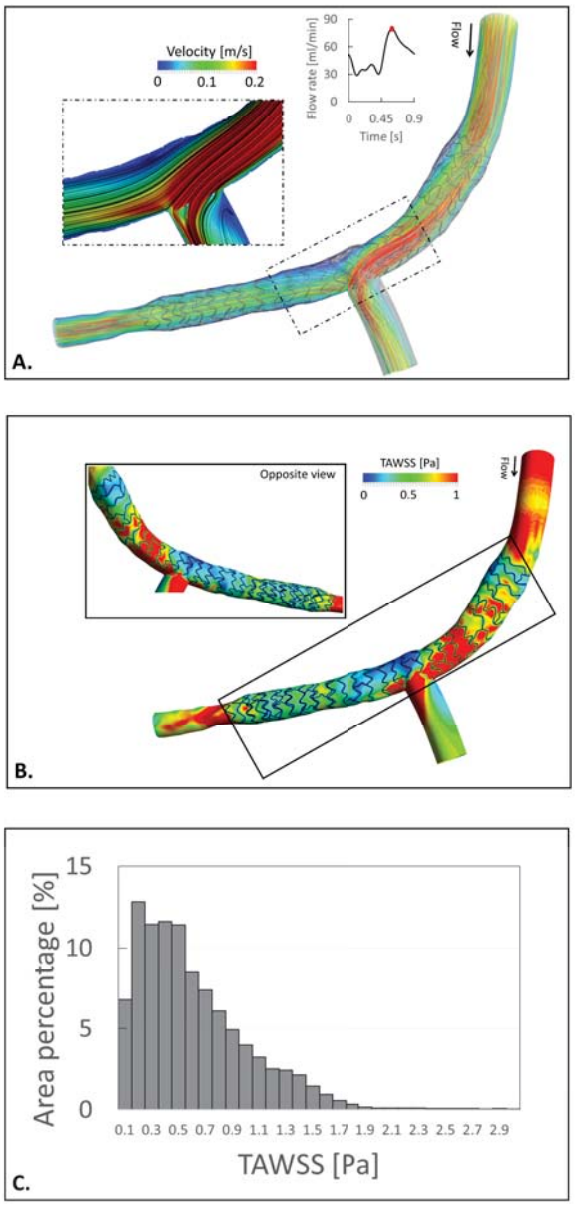

Figure 4.10 Results from the simulated flood flow of Case 4.A: Streamlines of the velocity coloured by the velocity magnitude (bottom) and the in-plane velocity contour-map with in-plane streamlines (top) at peak for flow rate. B: Contour map of the time-averaged wall shear stress (TAWSS) at the end of the simulated cardiac cycle (top) with an enlargement of the opposite view of the bifurcation (bottom). C: Histograms of the scaffolded surface percentage area under intervals of TAWSS from 0 Pa and 3 Pa.

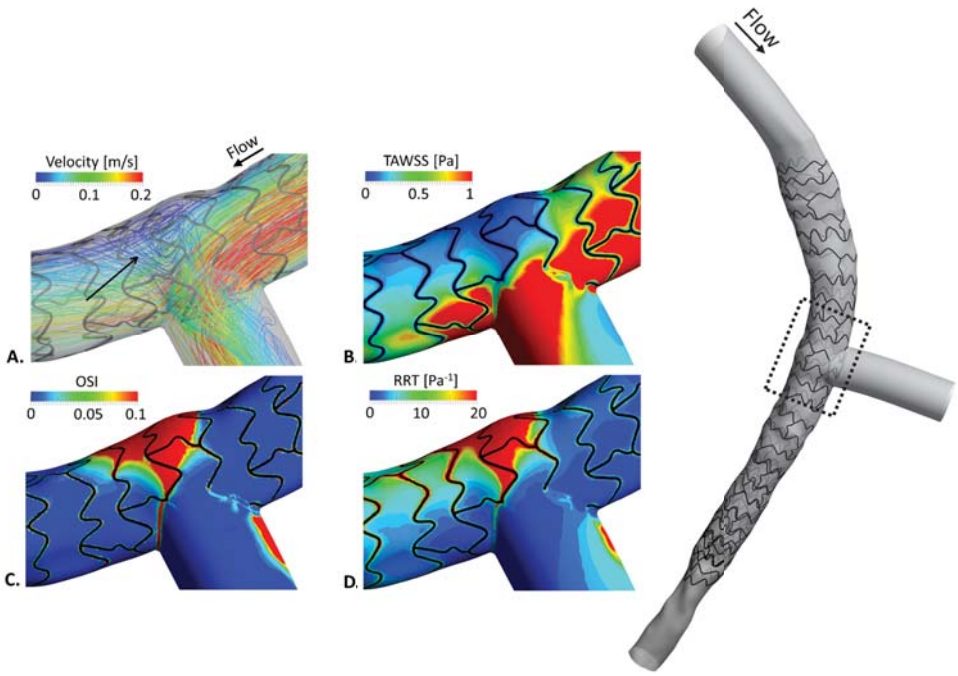

Figure 4.11 Distributions of the superficial hemodynamics quantities of Case 4 at the segment defined by the dotted rectangle. A: Streamlines of the velocity coloured by the velocity magnitude, the arrow depicts the flow recirculation at the bending of the vessels . B: Contour map of the time-averaged wall shear stress (TAWSS) over the simulated cardiac cycle. C: Contour map of the oscillatory index (OSI) that was computed over one cardiac cycle. D: Contour map of the residual residence time (RRT) computed over one cardiac cycle.

Chapter 5

Application to pre-operative CFD assessment: ulcerated plaque

In this Chapter the OCT-based reconstruction methodology was used to reconstruct a coronary artery segment characterised by ulcerated plaque. The peculiarity of such pathology is related to the hemodynamics at the lesion, which induces recirculation in the empty space between wall layers.

5.1 Introduction

SPONTANEOUS coronary artery dissection (SCAD) is a coronary artery disease that can cause acute myocardial infarction. It originates from a small opening at the intimal-media and the migration of blood into the vessel wall. The resultant detachment of tissue layers leads to a hematoma, with severe lumen occlusion and distortion. Evolutions of the pathology include bleeding in the intramural space, inflammatory reactions and intimal-media disruption that promotes an alternative path for plaque spreading (Giacoppo et al., 2014), as described in Fig.5.1. It is argued that most SCADs are at initially without luminal entry door that, subsequently, breaks and initiates a progressive enlargement of the intramural hematoma.

SCAD with open door can be recognised by angiographic features, such as

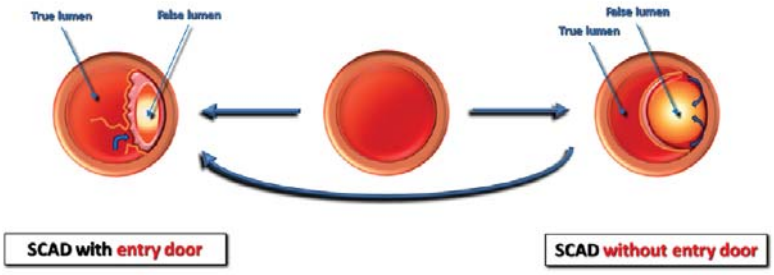

Figure 5.1 Spontaneous coronary artery dissection (SCAD), with entry door (left), that presents luminal entry door and a detached intimal-media membrane; SCAD without entry door (right), that has an intramural hematoma without communication with coronary lumen.*Reprinted with permission from International journal of cardiology, Vol. 175(1):8-20. Giacoppo D., et al. Spontaneous coronary artery dissection.* © *2014.*

prolonged intraluminal filling and delayed clearance of the contrast liquid. The diagnosis of this pathology is challenging due to the limited angiography resolution and acquisition frequency. Moreover, SCADs without open-door are angiographic invisible, therefore, intra-vascular imaging techniques are regularly employed for SCAD classification and treatment planning.

Registered clinical evidences report that the LAD is the most commonly involved vessel (59.7% of cases) followed by the RCA (26.5% of cases), the left circumflex (LCx) (19.4% of cases) and the left main coronary artery (LMCA) (8.9% of cases). Patients with SCAD are classified into three groups: cases affected by CAD, young women in the peripartum period and patients without known underlying coronary disease (DeMaio Jr et al., 1989). Indeed evidences support the hypothesis of some relation of SCAD with atherosclerosis,

hormonal changes during pregnancy and connective tissue disorders, however, there are some exemptions that present SCAD but display a weak relationship with such causes.
The treatment of ulcerated plaques is an open discussion, due to the high heterogeneity and the lack of evidences that support particular strategies. Therefore, the therapeutic decision should follow a detailed investigation of the involves echo-cardiographic indexes with angiography and endovascular imaging to locate the lesion, besides its extension and features as well as the lumen occlusion severity (Mortensen et al., 2009; Stone and St. Goar, 1996). PCI is recommended for unstable acute coronary syndromes. Stent deployment is suggested for dissections with relevant degree of lumen narrowing (70-90%) and in association with unstable condition. Stone and colleagues (Stone and St. Goar, 1996) reported the first case with SCAD that was treated with stent deployment 15 years ago and many successful procedures were registered.
OCT commonly presents good lesion coverage, stent apposition, but in some cases the intramural emathoma is persistent at the scaffolded region and at the distal extremity of the stent (75%). The successful rate of PCI for treatment of SCAD is variable, the literature registered rates between 65% and 90% (Giacoppo et al., 2014). Stent implantation is generally preferred, however it might represent a risk for complications, for instance the pressure applied to the false lumen and to the hematoma can induce the propagation of the lesion towards unaffected coronary segments (Giacoppo et al., 2014). The rate of SCAD spreading in healthy vessel wall is higher than in atherosclerotic vessels because the plaque between the wall layers is an impediment for detachement of the media membrane. It has been found that the medium length of SCAD in combination with CAD is approximately 37 ± 26 mm and in cases without atherosclerosis 23 ± 16 mm (Mortensen et al., 2009).
Currently it is not available a unique guidance for the management of SCAD, due to the low number of registered cases and the high pathological heterogeneity. The knowledge of lesion features lead to case-specific decision making approach.
The peculiar flow conditions across an ulcerated plaque can be emulated via computational simulations. Giannopoulos and co-authors (Giannopoulos et al., 2015) reconstructed an ulcerated plaque and performed CFD simulations to extract the hemodynamic implications of the lesion configuration.
This chapter describes a study that was performed from available pre-operative images. In particular, SCAD with open door was recognised in Case 3 (Fig.5.2) and the OCT images were elaborated to obtain a 3D geometry of the diseased vessel with side branches.

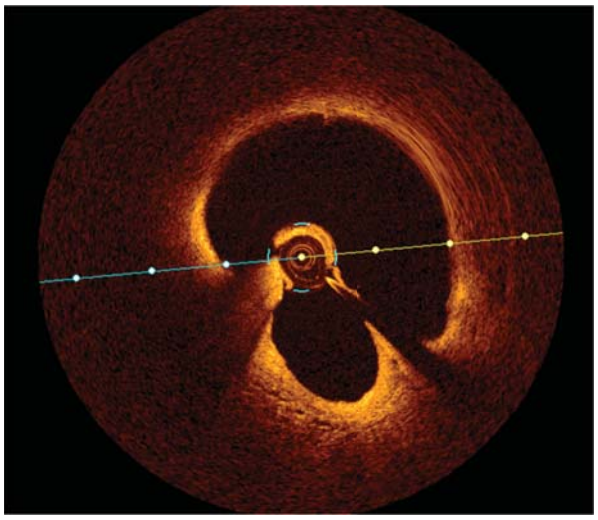

Figure 5.2 OCT frame that pictures the ulcerated plaque with open-door. The guide wire and OCT catheter are located in the true lumen, the broken membrane is in contact with the probe.

5.2 Methods

Pre-operative OCT images of Case 3 were elaborated with the methodology described in Chapter 3 to obtain the 3D reconstruction of the coronary artery segment with an ulcerated plaque and three bifurcations. The SCAD with open-door created a chamber, where the blood can recirculate, and the lesion narrowed the lumen for a length of about 16 mm between two bifurcations. Case 3 underwent PCI and the post operative flow conditions were described in Chapter 4.
In Fig.5.3 the 3D reconstruction of the RCA with a particular of the ulceration, Fig.5.3A. In Fig.5.3C a particular of the occluded coronary segment displayed the geometry of the ulcerated plaque, which created a chamber in the arterial wall. This last can cause heavy flow recirculation and stagnation. The geometry was divided in 1,849,596 tetrahedral elements with ANSYS ICEM v.16 (ANSYS Inc.), the ulceration was discretised with a high density mesh, as shown in Fig.5.3C. This allowed a good representation of the local flow conditions while preserving limited computational costs. The transient CFD analysis was performed using ANSYS Fluent v.16 (ANSYS Inc.). As done for the previous analyses, a typical human RCA flow waveform (Davies et al., 2006) was applied as a paraboloid-shaped velocity profile to the inlet surface (Chiastra et al., 2013b). Its average value in time was defined so that the flow-rate was 64.32 ml min^{-1}, computed by means of the relationship introduced by Sakamoto and

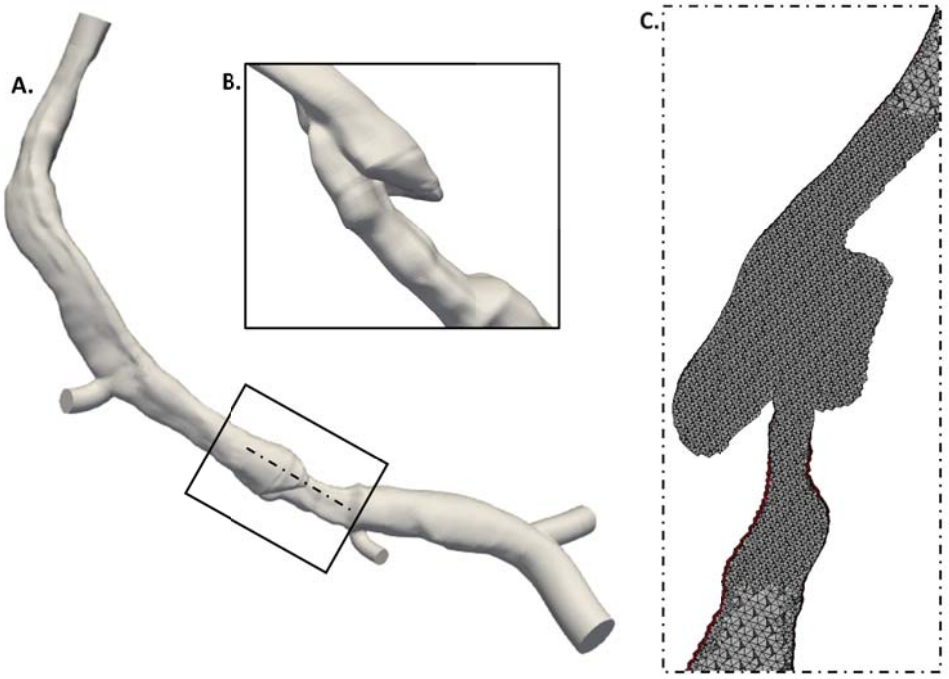

Figure 5.3 3D reconstruction of a RCA affected by SCAD. A: 3D geometry; B: Particular of the ulcerated plaque; C: Longitudinal section of the volume mesh, with higher density at the plaque.

co-authors (Sakamoto et al., 2013). At the outlet surface a zero pressure condition was set. No slip-condition was applied to the arterial and stent walls, which were defined as rigid. Details abut the solver settings are reported in Chapter 4, in the work of Chiastra and co-authors (Chiastra et al., 2013b). The blood was modelled as an incompressible, non-Newtonian fluid using the Carreau model (Caputo et al., 2013). The blood density was set to 1060 kg m^{-3} (Kessler et al., 1998).

Results were analysed seeking to provide a picture of the flow disruption caused by this type of pathology. Firstly, the flow stream at the ulceration was described focussing on both the whole domain and the lesion. Secondly, the WSS averaged over a cardiac cycle was reported as contour map, with an upper limit of 10 Pa, and its distribution was captured in terms of percentage area of the vessel surface.

5.3 Results

In Fig.5.4 the 3D streamlines of the blood velocity at peak of the flow rate were reported. In Fig.5.4A and Fig.5.4B presented two views of the lesion. The local flow stream was characterised by heavy recirculation both at the ulceration and at the interface with the normal lumen, which can lead to blood stagnation. The peculiar geometry of the plaque caused flow vorticity in the chamber, as reported in Fig.5.4C, and at the lumen separation pictured in Fig.5.4D. The planar section of the SCAD presented the abnormal vessel shape, with discontinuous intra-luminal space. Moreover, the increase of lumen cross section area after the lesion resulted in large recirculation and local vorticity.
In Fig.5.5 the contour-map of the distribution of TAWSS over the simulated cardiac cycle is shown. The reduced lumen cross-section area at the diseased region caused values of TAWSS above 10 Pa, that was the 0.49% of the vessel lumen. On the other hand, the lumen surface at the vessel enlargement experienced TAWSS below 0.4 Pa, that was the 16.34% of the domain shown in Fig.5.6. The regions under low and moderate values of TAWSS were reported respectively in blue and green, whereas in gray and red the areas under high TAWSS were depicted (Wentzel et al., 2012). The superficial distribution of TAWSS at the ulceration mirrored the variable flow stream in such region.

5.4 Conclusion

The developed OCT-based reconstruction methodology was successfully employed to study the effect of SCAD with plaque ulceration on the hemodynamics. Results revealed a high degree of flow recirculation both at the ulceration and at the interface with the normal lumen.
The lack of clinical practice guidelines makes the treatment of non-occlusive plaques an open question. The application of advanced intra-coronary images, high fidelity reconstructions and CFD simulations might guide the management of such pathology.
The achieved findings proved the applicability of the developed framework for CFD analyses on complicated patient-specific anatomies, such as ulcerated plaques. A potential application is the prediction of the diffusion of ulceration though intra-mural space, as WSS might provide indexes of local wall failure. For instance, similar analyses were performed in the literature to predict the failure of aneurysms. Steinman and colleagues (Steinman et al., 2003) simulated the blood flow in a intracranial aneurysm reconstructed from computed

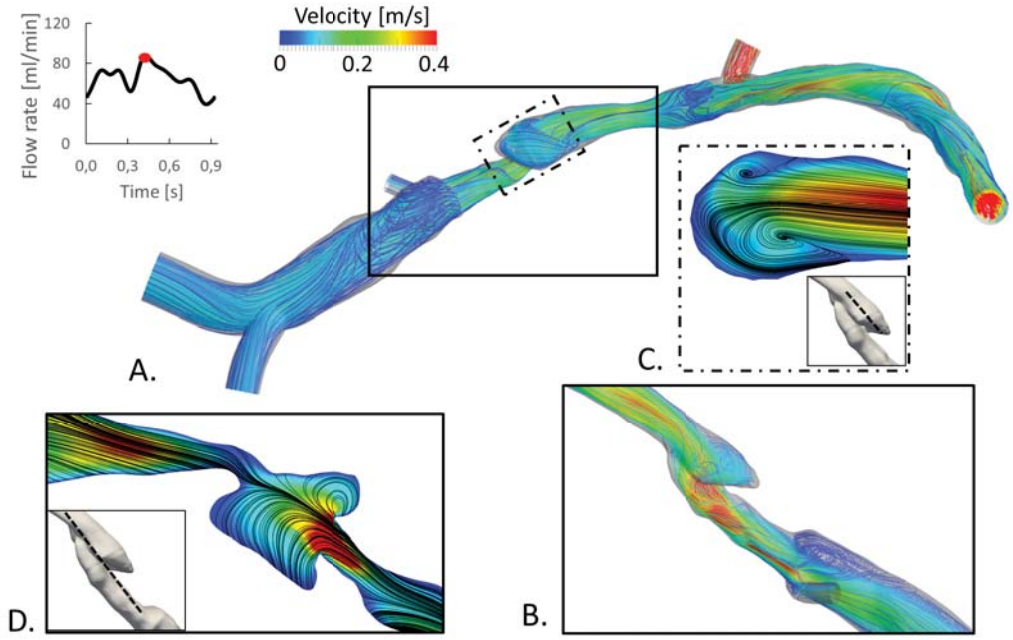

Figure 5.4 Streamlines of the velocity coloured by the velocity magnitude (A,B) and the in-plane velocity contour-map with in-plane streamlines (C,D) at peak for flow rate.

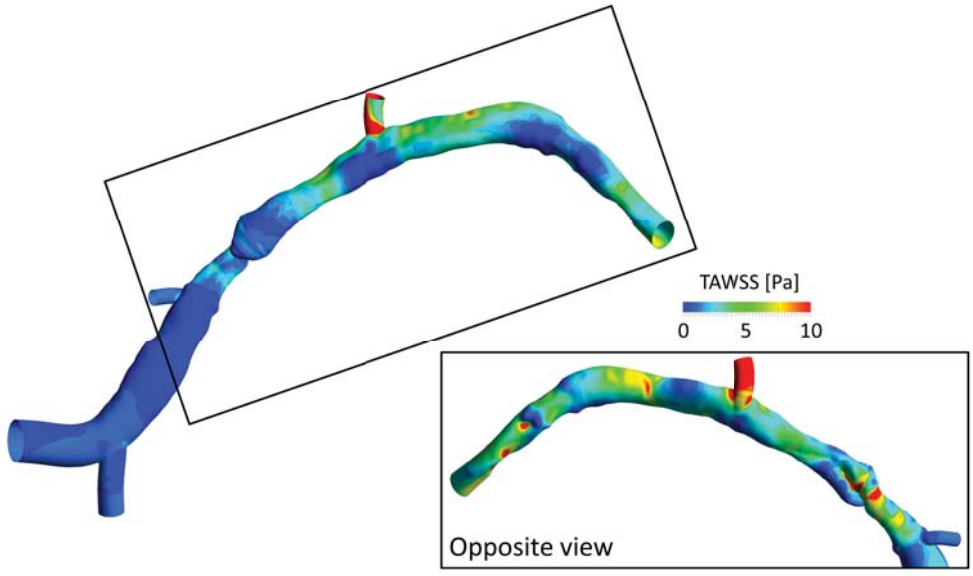

Figure 5.5 Contour map of the time-averaged wall shear stress (TAWSS) at the end of the simulated cardiac cycle (top) with an enlargement of the opposite view of the bifurcation (bottom).

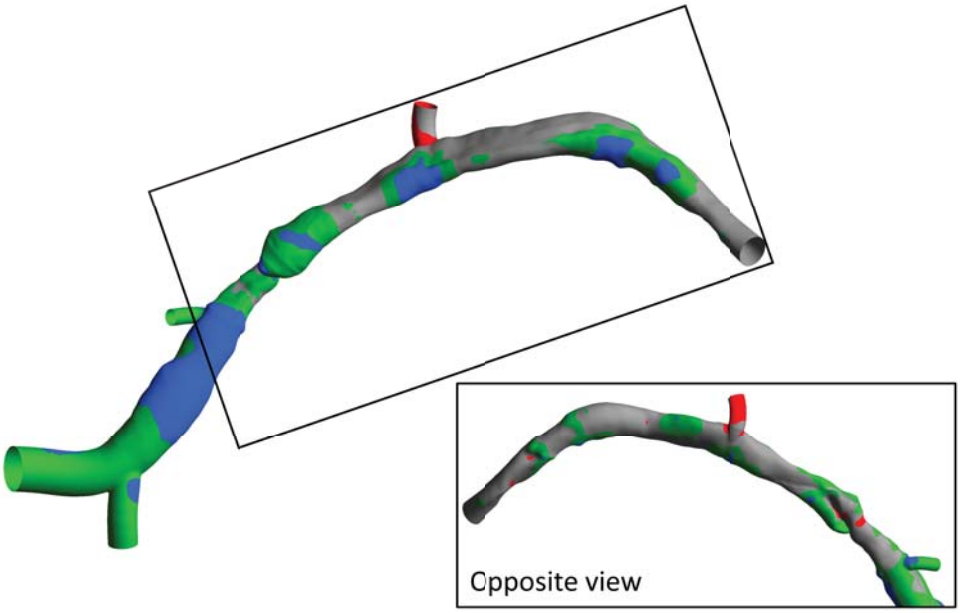

Lumen area [%]			
TAWSS < 0.4 Pa	0.4 Pa < TAWSS < 2 Pa	2 Pa < TAWSS < 10 Pa	TAWSS > 10 Pa
16.34	44.07	37.49	0.49

Figure 5.6 Contour map showing intervals of the time-averaged wall shear stress (TAWSS) at the end of the simulated cardiac cycle (top) with an enlargement of the opposite view of the bifurcation (bottom).

rotational angiography. The prediction of WSS associated to the anatomy of the disease could assist the assessment of wall growth and rapture, as well as the clinical decision making.

Chapter 6

Application to polymeric bioresorbable scaffold for the treatment of coronary bifurcations

This chapter describes the computational fluid dynamic analysis that were performed to assess the coronary hemodynamics of patients treated with polymeric bioresorbable scaffolds.The work was carried out in collaboration with the Sussex Cardiac Centre, Brighton and Sussex University Hospitals, Brighton, UK. A dedicated algorithm for the segmentation of the acquired OCT images was developed, so that the polymeric scaffolds could be automatically identified. Moreover, the 9-months follow-up image sets were elaborated to evaluate the remodelling of the vessel wall and results were compared with the hemodynamics.

Part of the content of this chapter is included in the paper **S Migliori** et al. (Migliori et al., 2018) that was published in the Open Access Journal Applied Sciences.

6.1 Introduction

IN the past years, bioresorbable coronary devices have been developed seeking to overcome the limitations of the state-of-the-art drug-eluting permanent stents, including the risks of target lesion revascularisation, neoatherosclerosis, hindrance of late lumen enlargement, and the lack of reactive vasomotion in the stented vessel (Sotomi et al., 2017). These devices, which are referred to as bioresorbable scaffolds, fully dissolve in the vessel wall in two or three years after recovering the lumen passageway (Sotomi et al., 2017).
The ideal bioresorbable scaffold re-opens the artery without any long-term adverse sequelae such as restenosis or thrombosis. Vascular tissue re-modelling after stent implantation is influenced by the local blood flow pattern (Van der Heiden et al., 2013). The endothelium actively responds to wall shear stress (WSS), which triggers vascular smooth muscle cell proliferation and migration to the endoluminal surface causing vessel healing and strut coverage. This last can be quantified by measuring the neo-intimal thickening (NIT), which is defined as the perpendicular distance between the midpoint of the adluminal strut surface and the inner luminal surface measured on optical coherence tomography (OCT) images (Van der Heiden et al., 2013). Another method is to calculate the restenosis area defined as the difference between the scaffold area and the sum of the strut and luminal area at a particular cross-section of the OCT on follow-up imaging. The evaluation of WSS relies on the application of CFD to model patients hemodynamics. The incidence of adverse neointimal hyperplastic response may be predicted using surrogate quantities, such as a low WSS averaged over one cardiac cycle ($\leqslant$ 0.4 Pa) (Malek and Izumo, 1996) and disrupted flow stream at bifurcation.
The validated reconstruction methodology described in Chapter3 was employed to achieve high fidelity 3D models of twelve patients that underwent PCI and the insertion of an Absorb BVS (Abbott Vascular, Abbott Park, IL, USA) at the Sussex Cardiac Centre, Brighton and Sussex University Hospitals (Brighton, UK). The patients were selected for the Absorb in Bifurcation Coronary trial (ABC-ONE), a single centre, randomized trial (Rampat et al., 2018). It aimed to compare the outcomes from different sizing strategies for the treatment of coronary bifurcation disease. The study complied with the Declaration of Helsinki on human research and was approved by the South East Coast (Brighton and Sussex, UK) Research Ethics Committee. All patients gave informed consent.

6.2 Image segmentation

The polymeric material has different optical properties than metals, therefore a dedicated segmentation algorithm was developed for the identification of polymeric BVS struts. The light emitted by the OCT probe can pass through the struts and reflections come from the difference in refractive index between the scaffold and the surrounding environment. Therefore, the stent struts are recognisable as black boxes closed by bright boundaries. The work of Wang and co-authors (Wang et al., 2014) proposed an approach that is usually considered as reference for the segmentation of polymeric BVS.
The implemented algorithm comprised four main steps: *i)* image pre-preprocessing; *ii)* lumen segmentation; *iii)* stent struts segmentation; *iv)* strut-based lumen correction. Seventeen in-vivo OCT pullbacks of coronary arteries treated with the Absorb BVS (Abbott Vascular) were selected to develop and validate the segmentation algorithm.

6.2.1 Image pre-processing

The pre-processing step was similar to the one defined for metallic stents, as described in the Chapter 3. Briefly, the OCT images (Fig.6.1A) were elaborated to remove the visualization tools and the OCT catheter. A further processing step was employed to remove the noise in the lumen, which was due to the injected contrast liquid for OCT procedure. This noise was removed by means of a binary mask that was created with the following steps: *i)* intensity thresholding, voxels with an intensity below the threshold were included in the mask; *ii)* morphological opening, this was used to enlarge clusters of voxels, *iii)* area thresholding, large regions were removed. The result was a set of images with an uniform dark lumen.

6.2.2 Lumen contour segmentation

The strategy used to detect the internal lumen contour was similar to the one described in the Chapter 3. The pre-processed images were converted into polar coordinates (i.e. r and θ) and a Sobel filter was applied to detect the edges with high intensity voxels. The first pixel detected as edge for each value of θ (i.e. for each A-scan) was considered as part of the lumen contour. The identified pixels were interpolated and the result was converted back to Cartesian coordinates. In Fig.6.1B the internal lumen contour in Cartesian coordinates.

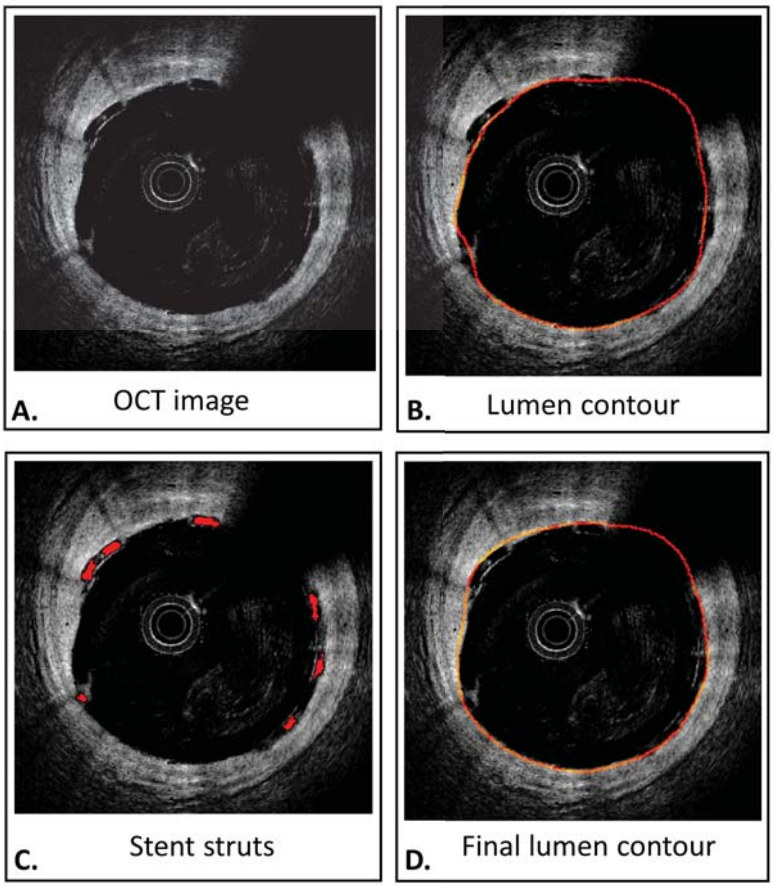

Figure 6.1 Detected components from the segmentation of OCT images that picture a coronary artery treated with Absorb BVS stent (Abbott Vascular). A: OCT frame. B: Detected lumen contour (a dilatation of 1 pixel was applied to enable the edge visualization). C: Detected stent struts. D: Final lumen contour after the correction with the stent struts (a dilatation of 1 pixel was applied to enable the edge visualization).

6.2.3 Stent segmentation

An innovative strategy was implemented for the detection of scaffold struts. It was performed entirely in Cartesian coordinates. The scaffold recognition was based on the rectangular-shaped dark clusters of voxels. The procedure comprised three main steps: *i)* intensity thresholding, the dark regions were identified via a pre-defined quantile of the pixel intensity distribution; *ii)* holes filling, to close any space in the binary image; *iii)* boolean subtraction of the original binary image from the filled image. This procedure failed when the bright rectangular contours presented gaps (i.e. open box struts), instead false positives were identified. This problem was addressed by a first morphologi-

cal closing, besides the intensity thresholding step, and by enhancing the image contrast with nonlinear filter (γ-filter, with γ=0.6).
The false positives were removed by means of successive elaborations. Firstly, acceptable struts area values were bounded between specific number of pixels. Then, the lumen contour line was dilated in order to cover the region with high probability of struts presence. Lastly, the centroids of the struts identified by a first rough segmentation were interpolated with a spline and centroids that laid at a distance within a tolerance were considered scaffold voxels. This interpolation line was created also from the struts identified in the images adjacent to the one of interest, to account for images with a low number of struts, where the quality of the interpolation is low. In Fig.6.1C the detected scaffold struts after the corrective elaborations.

6.2.4 Strut-based lumen correction

This is the last step of the segmentation process. The vessel lumen contour at baseline was expected to stay underneath the scaffold struts. However, the lumen identified in the first part of the algorithm was not accurate when either two struts were in contact, or there was residual blood close to the lumen wall. The struts-based correction provided a new lumen contour by combining the pre-correction lumen with the line that interpolated the position of the abluminal wall of the struts. This analysis was performed in polar coordinates. For each θ, only the contour with the highest radial value was chosen. In Fig.6.1D the obtained lumen contour at baseline.

6.2.5 Validation of the OCT segmentation algorithm

To validate the algorithm, the results were compared with manual segmentation performed by an expert reader using open source software MRIcro (http://www.mccauslandcenter.sc.edu). In particular, the region of interest (ROI) for lumen segmentation was the region enclosed in the identified lumen contour in each OCT image, while for scaffold segmentation the ROIs were represented by the scaffold struts. Fifty test images were sampled for each acquisition, for a total of 850 images for the lumen and 850 images for the scaffold. The sampling of the images was performed uniformly through the whole acquisition for the lumen segmentation and the scaffolded portion for the stent segmentation. The quality of the automatic segmentation was assessed through the computation of sensitivity and specificity indexes, expressed as mean and standard deviation (Migliori et al., 2017).

6.3 3D geometry reconstruction and CFD simulations

The treated coronary artery segments with bifurcations of twelve patients were reconstructed by means of the developed methodology. In particular, the point clouds for the lumen and the implanted stent were aligned with the 3D vessel centerline. This last was obtained from angiographic images that were elaborated with a commercial software (CAAS, PIE Medical Imaging).
The procedure that was followed to reconstruct the MB with bifurcations is described in Chapter 4. The surface for the blood vessel MB was defined as follows. The lumen contour curves were built from a point interpolation and, then, were used to create the lumen surface with a lofting procedure. The side branches were reconstructed from information obtained with a 3D-QCA that was carried out with CAAS (PIE Medical Imaging).
The Absorb BVS skeleton was drawn in Rhinoceros v.5 (Robert McNeel & Associates, Seattle, WA, USA) as a sequence of sinusoidal rings connected with straight bridges, in order to resemble the actual BVS design. High resolution pictures were taken during an in-vitro free expansion of an Absorb BVS. These were used to extract measurements that were useful to customise the sinusoidal function, so that the crowns were correctly resembled. In Fig.6.2 a crown of the drawn skeleton and a high resolute picture of the expanded device are shown. This last was morphed in order to minimise the distance with the aligned stent point cloud, as described in Chapter 4. The final 3D reconstructions of the implanted scaffolds were achieved by means of the graphical algorithm editor Grasshoper® (www.grasshopper3d.com). In particular, the cross-section curves were rectangles with sides that were customised according to the size of the scaffold. In general, Absorb BVS designs can be grouped in small scaffolds and medium scaffolds. The former have an external diameter of 2.5-3 mm, the ring and bridge cross-sections have sizes (i.e. width x thickness) of 0.905 x 0.1575 mm and 0.1397 x 0.1575 mm. The medium design have a diameter of 3.5 mm, the cross sections of ring and the bridges are 0.2159 x 0.1575 mm and 0.1397 x 0.1575 mm rectangles (Food and Administration, 2016).
In Tab. 6.1 the twelve studied cases are listed, with information about the coronary artery segment, size of the implanted device and number of reconstructed side branches. The majority of the lesions were located in the LAD at bifurcation with the first diagonal, one case was treated at the RCA and one at the LCx. The size of the implanted Absorb BVS scaffolds were chosen according to the randomized criterion, that is the stent diameter was defined from the dimension of the MB either proximal or distal to the treated bifurcation. In Fig.6.3 the

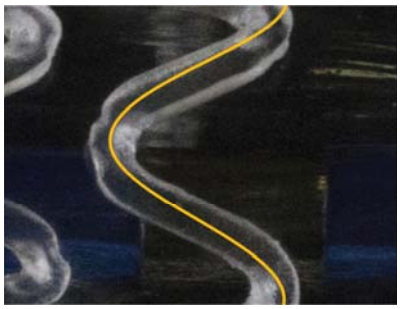

Figure 6.2 The drawn Absorb BVS skeleton (in orange) that was superimposed on a high resolution picture of the expanded stent.

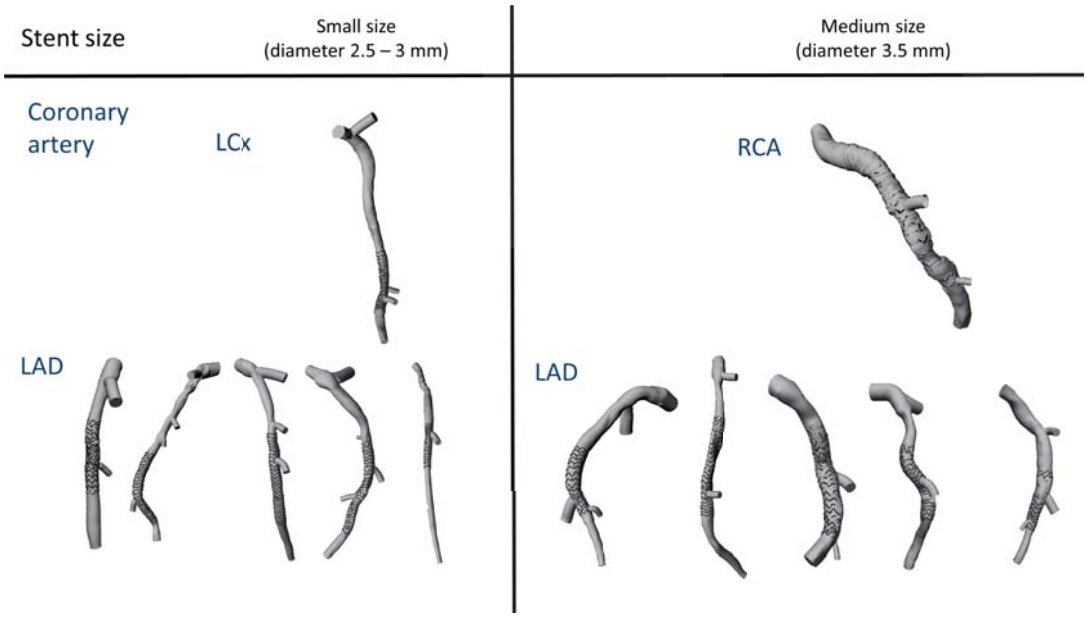

Figure 6.3 The 3D reconstructions of the analysed twelve cases, which are grouped according to the coronary artery branch and the size of the implanted scaffold.

3D reconstructions of the analysed twelve cases are grouped according to the coronary artery branch and the size of the implanted scaffold.

Geometric characteristics of each 3D geometry were used to obtain the corresponding flow-split conditions at the outlets, implemented with the relationship proposed by van der Giessen (Van der Giessen et al., 2011). The surfaces of the blood vessel and the stent were rigid and no-slip settings were imposed as boundary conditions. Details abut the solver settings are reported in Chapter 4, in the work of Chiastra and co-authors (Chiastra et al., 2013b). In Table 6.2 a summary of the boundary conditions imposed to the CFD model specific for

Table 6.1 Details of the treated coronary artery segment and implanted stent, reported as nominal external diameter and length.

Cases	**Treated coronary artery**	**Stent size** $[mm]$	**MB length** $[mm]$	**Number of SBs**
Case 5	LAD	3.5 x 18	57.14	3
Case 6	LAD	3 x 28	71.8	4
Case 7	RCA	3.5 x 28	51.47	2
Case 8	LAD	3.5 x 23	64.24	3
Case 9	LAD	3.5 x 23	39.79	2
Case 10	LAD	3 x 23	44.34	2
Case 11	LAD	3.5 x 28	73.35	2
Case 12	LAD	3.5 x 18	62.7	3
Case 13	LAD	3 x 28	71.26	3
Case 14	LAD	3 x 28	69.6	4
Case 15	LAD	2.5 x 18	82.05	1
Case 16	LCx	3 x 18	67.6	3

each patient, the flow at the distal MB and SB respectively, with the grid dimension.
For each case, the velocity field within the domain was evaluated at the peak of flow rate. Then, the pattern of time-average wall shear stress (TAWSS) over the simulated cardiac cycle was assessed, focusing on regions under values of TAWSS considered as potential trigger for complications, such as ISR, that is TAWSS $\leqslant$ 0.4 Pa. Moreover, the percentages of the lumen surface area that were exposed to intervals of TAWSS between 0 Pa and 3 Pa were computed. Such plot provides quantitative information about the global spectrum of the wall shear stresses at the endothelium.

6.3.1 Neo-intimal thickening at follow-up

Among the objectives of the trial ABC-ONE, reported in the work of Rampat and colleagues (Rampat et al., 2018), was the assessment of clinical outcomes of the implantation of Absorb BVS at coronary bifurcations. This was performed by comparing the OCT images sets at baseline and after 9 months from PCI. Therefore, the availability of intravascular images at 9-months follow-up enabled the computation of the neo-intimal coverage, defined in terms of percentage restenosis area.
The OCT image set at 9-months follow-up were elaborated to retrieve the lumen

Table 6.2 Information of the implemented CFD model for cases' hemodynamic assessment.

Cases	**Number of elements**	$\mathbf{Q}_{inlet}$ $[ml\ min^{-1}]$	**Flow split ratios**
Case 5	$5.32 \cdot 10^6$	38.16	0.39:0.2:0.33:0.08
Case 6	$5.24 \cdot 10^6$	97	0.19:0.38:0.23:0.12:0.08
Case 7	$6.5 \cdot 10^6$	96	0.72:0.19:0.08
Case 8	$6.06 \cdot 10^6$	229	0.23:0.65:0.1:0.02
Case 9	$4.3 \cdot 10^6$	81.92	0.75:0.216:0.037
Case 10	$3.3 \cdot 10^6$	90.17	0.442:0.495:0.064
Case 11	$6.17 \cdot 10^6$	77	0.38:0.53:0.09
Case 12	$6.66 \cdot 10^6$	252.18	0.18:0.54:0.2:0.07
Case 13	$5.19 \cdot 10^6$	177	0.22:0.58:0.13:0.07
Case 14	$5.089 \cdot 10^6$	96	0.23:0.48:0.05:0.16:0.08
Case 15	$2.0297 \cdot 10^6$	29.24	0.59:0.41
Case 16	$3.821 \cdot 10^6$	43.14	0.45:0.38:0.04:0.13

contours both at baseline and at follow-up. This choice was motivated by the fact that it is not possible to uniquely correlate each baseline OCT frame to the corresponding frame at follow-up because of many factors, such as blood vessel remodelling, different catheter path and unpredictable pull-back start point. Fig.6.4 shows an illustration of the components used to define the percentage restenosis area. The follow-up lumen contour was the innermost lumen boundary (Fig.6.4A), the stent struts were used as guidance for the identification of the baseline lumen contour (Fig.6.4B-C). In some cases, malapposed scaffold struts at baseline appeared completely covered by neointima in the follow-up acquisition. For such cases, the baseline lumen contours for the computation of the NIT were traced as shown in Fig.6.4C, as the high image resolution enabled to distinguish the grown layer of vascular smooth muscle cells. Whereas, the malapposed stent struts at follow-up were not considered for the computation of the NIT. A similar approach was used by Bourantas and colleagues (Bourantas et al., 2014a) to compute the neo-intima thickening after 1-year follow-up. Thus, the regions that were assumed as NIT are reported in Fig.6.4D. The tissue remodelling was quantified by the ratio between NIT area and the baseline lumen area, reported as the percentage of restenosis area. Such evaluation was performed at the scaffolded portion of the main branch, which was divided in proximal and distal regions, with respect to the side branch, and in bifurcation region, at the side branch.

Seeking to explore the relationship between TAWSS and NIT, the percentages of lumen area under intervals of TAWSS were related to the computed percentage of restenosis area. Quantitative evaluations were performed with plots and statistical indexes. Moreover, the relative distance between follow-up and baseline lumen contours was mapped on a 2D grid that was compared with the distribution of RRT.

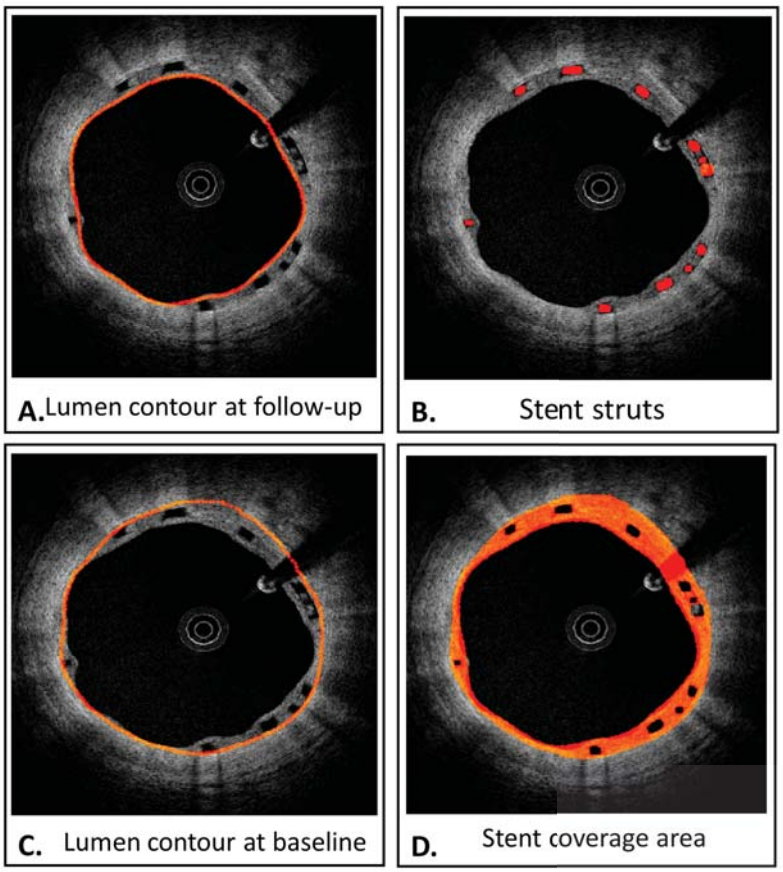

Figure 6.4 Definition of lumen contour at 9-months follow-up (A), stent struts(B) and at baseline (C). The restenosis area was obtained from the pixels between contours that was subtracted with the stent struts.

Table 6.3 Similarity indices for the segmentation of lumen and stent.

	Sensitivity	**Specificity**
Lumen	$98.4 \pm 3.14\%$	$99.48 \pm 0.33\%$
Stent	$78.64 \pm 20.10\%$	$91.42 \pm 15.89\%$

6.4 Results

6.4.1 Validation of the segmentation algorithm

In Tab.6.3 the results of the segmentation algorithm validation. The similarity indexes for the lumen segmentation were large and comparable with results obtained from the segmentation of metallic scaffolds. Limitation of the results was due to the fact that the struts appeared in the elaborated images as open-boxes rather than well define closed structures. As a consequence, the strategy proposed by Wang and co-authors (Wang et al., 2014) was not effective.

6.4.2 CFD simulations

Results obtained from the fulfilled CFD simulations of each case were reported as follows. Firstly, the velocity streamlines at peak of flow rate were shown, so that flow recirculation and the influence of the stent were presented. Secondly, the contour map plots pictured the distribution of TAWSS along the arterial wall over the simulated cardiac cycle. Moreover, the area percentages of the scaffolded lumen surface under TAWSS below 3 Pa, seeking to present a quantitative plot of the resultant distribution including a wide spectrum of values (Wentzel et al., 2012). Finally, the area percentage values of the scaffolded main branch segment that underwent TAWSS $\leqslant$ 0.4 Pa were reported, considered critical for the occurrence of ISR (Malek et al., 1999).
Results from the simulated hemodynamics of Case 5 are reported in Fig.6.5. The velocity streamlines were characterised by a smooth trend and followed the vessel curvature, as reported in Fig.6.5A. The distribution of TAWSS at the proximal and scaffolded regions was mainly below $\sim$0.5 Pa, which was caused both by the low flow rate at the inlet and by the lumen cross section area. Whereas distally the reduced lumen area resulted in higher WSS, as reported in Fig.6.5B-C. Critical TAWSS values ($\leqslant$ 0.4 Pa) were found in the 17.07% of the scaffolded main branch segment. Results from the simulated hemodynamics of Case 6 are reported in Fig.6.6. In Fig.6.6A the velocity streamlines were heavily affected by the vessel bending at the scaffolded segment. The in-plane flow

pattern displayed the interaction between the flow and the stent struts at the bifurcation. In Fig.6.6B-C the distribution of TAWSS at the scaffolded region was mainly below ∼0.5 Pa, which was directly related to the reduced flow velocity. Critical TAWSS values ($\leqslant$ 0.4 Pa) were found in the 63.04% of the scaffolded main branch.

Results from the simulated hemodynamics of Case 7 are reported in Fig.6.7.In Fig.6.7A the velocity streamlines were affected both by the vessel curvature and by the superficial roughness of the lumen, as well as by the malapposed stent struts. In Fig.6.7B-C the distribution of TAWSS at the scaffolded region was mainly below ∼0.3 Pa, due to localised flow recirculation. The 79.52% of the scaffolded main branch segment underwent TAWSS $\leqslant$ 0.4 Pa. Results from the simulated hemodynamics of Case 8 are reported in Fig.6.8. In Fig.6.8A the velocity patterns were due to the vessel tortuous 3D shape. This last affected the distribution of TAWSS Fig.6.8B-C at the scaffolded region, which comprised high values of WSS, above ∼0.3 Pa. The 41.19% of the scaffolded main branch segment underwent TAWSS $\leqslant$0.4 Pa. Results from the simulated hemodynamics of Case 9 are reported in Fig.6.9. In Fig.6.9A the velocity streamlines experienced recirculation and stagnation where the vessel bends. Consequently, the TAWSS contour-map in Fig.6.9B was featured by low values and were influenced by stent malapposition. The distribution in Fig.6.9C confirmed that the 39.01% of the scaffolded main branch underwent TAWSS below 0.4 Pa. Results from the simulated hemodynamics of Case 10 are reported in Fig.6.13. In Fig.6.13A the velocity streamlines at peak of flow rate. Blood flow into the diagonal branch was disrupted by the presence of the scaffold over the orifice leading to micro-re-circulatory zones. Fig.6.13B shows the contour map of TAWSS along the arterial wall at the end of the simulated cardiac cycle. The distribution of TAWSS at the scaffolded main branch was reported in terms of percentage area in Fig.6.13C. The 55.6% of the scaffolded main branch segment underwent TAWSS $\leqslant$ 0.4 Pa. Low values of TAWSS were found at the region of stent malapposition, as the stent struts and local surface roughness induced localised flow recirculation. Results from the simulated hemodynamics of Case 11 are reported in Fig.6.11. In Fig.6.11A the velocity streamlines were slowed at the wall by the malapposed struts. The plots in Fig.6.11B-C showed the TAWSS pattern, with values below $\leqslant$0.3 Pa. The lumen shrinkage near the bifurcation and the following re-enlargement reflected in a localised area of high TAWSS within the scaffold. Finally, the distal vessel portion was under high values of WSS. The 68.06% of the scaffolded main branch segment underwent values of TAWSS below 0.4 Pa. Results from the simulated hemodynamics of Case 12 are reported in Fig.6.12. In Fig.6.12A the velocity

streamlines were affected by the vessel curvature. The in-plane velocity pattern reported the flow disruption at the bifurcation due to the presence of the stent. The plots in Fig.6.12B-C showed the TAWSS pattern, with values above 1 Pa. The 26.29% of the scaffolded main branch segment underwent values of TAWSS below 0.4 Pa. Results from the simulated hemodynamics of Case 13 are reported in Fig.6.13. In Fig.6.13A the blood flow appeared smooth in the domain, whereas the lumen enlargement at the proximal stent extremity induced flow recirculation. In Fig.6.13B the vessel curvature gave regions with higher values of TAWSS at one lumen semi-surface. In Fig.6.13C the 41.57% of the scaffolded main branch segment underwent TAWSS $\leqslant$ 0.4 Pa. Results from the simulated hemodynamics of Case 14 are reported in Fig.6.14. The vessel curvature and change of lumen cross-section size caused zones with decreased flow velocity in Fig.6.14A. The distribution of TAWSS was characterised by moderate values below $\leqslant$0.7 Pa and the 37.69% of the scaffolded surface in Fig.6.14B-C had values below 0.4 Pa. Results from the simulated hemodynamics of Case 15 are reported in Fig.6.15.Local lumen shrinkage in the proximal region induced flow acceleration in Fig.6.15A and in in-plane lines pictured the flow disruption due to the stent struts. The distribution of TAWSS at the scaffold was featured by values below 0.7 Pa in Fig.6.15B-C. The 17.06% of the scaffolded main branch segment underwent TAWSS with in the critical range. Results from the simulated hemodynamics of Case 16 are reported in Fig.6.16. The velocity streamlines at peak of flow rate in Fig.6.16A followed the vessel 3D shape, the change of lumen cross-section size caused zones with decreased flow velocity. Fig.6.16B-C shows the TAWSS values along the arterial wall at the end of the simulated cardiac cycle, the 49.21% of the scaffolded main branch segment was in the critical range.

6.4.3 Neo-intima thickening and wall shear stress

The computed percentage restenosis area are shown in Fig.6.17. The reported boxplots show different degrees of NIT dispersion among regions across the scaffolded segment. The data sets of the proximal region were characterised by dispersions with different amplitude and a larger number of outsiders compared to the other vessel regions, as reported in Fig.6.17A. The computed NIT at the bifurcations presented larger degree of skewness for the majority of cases, as reported in Fig.6.17B. Whereas, the widest distributions of percentage of restenosis area were found at the distal regions, as reported in Fig.6.17C. The Kruskal-Wallis and the Wilcoxon tests reported significant statistical differences between distributions of TAWSS and NIT, exception made for the bi-

furcation region of Case 5 and Case 11 ($p>0.05$). Spearmans test reported a monotonic relationship between data sets at the stented segment of Case 5 and Case 8 ($\rho > 0.7$). At the proximal regions of Case 8, Case 11 ($\rho \sim 0.7$) and Case 9 ($\rho \sim 0.9$); at the bifurcation regions of Case 5 ($\rho \sim 0.7$), Case 11, Case 14 ($\rho \sim 0.8$), Case 8 ($\rho \sim 0.9$); at the distal regions of Case 8 ($\rho \sim 0.7$), Case 7 ($\rho \sim$-0.9). The distance between lumen contour at baseline and at 9-months follow-up was computed from the follow-up OCT acquisition and it was mapped on a grid resembling the scaffolded segment, therefore the size of the grid was defined according to the circumference and length of the stented main branch. The position of the bifurcations were defined by the corresponding OCT frames and the range of pixels within each frame and were depicted in the maps as rectangles. The regions of the scaffolded vessel were indicated with dotted lines as proximal (Prox), bifurcation (SB) and distal (Distal) regions. Moreover, the contour map of RRT over the simulated cardiac cycle was shown as contour plot. The two sides of the vessel were defined by means of the side branch with the larger diameter, respectively at the branch side (front side) and opposite to the bifurcation.

The contours distance map and RRT distribution of Case 5 is shown in Fig.6.18. The grid that was used to plot the distance values was defined so that the circumference of the vessel and a length of 19 mm were spanned. The distance map reported minimum values at the proximal region and larger values in a small area between the bifurcation and distal regions. Three areas with large RRT were found along the scaffold, which were mainly located at the malapposed scaffold struts. A limitation of this analysis was represented by the low quality of the image set that did not enable a clear visualisation of the grown tissue. In fact, the proximal region of the scaffold was malapposed at baseline and was completely covered by the neo-intima after 9 months from the intervention. Therefore, a possible consideration of the described findings can be that the detachment between stent struts and the vessel wall induced heavy flow recirculation which might have facilitated the coverage of the stent by the neointima.

The map of the distance between lumen contours and RRT distribution at the scaffolded segment of Case 6 are shown in Fig.6.19. The grid that was used to plot the values was defined so that the circumference of the vessel and a length of 29 mm were spanned. The distance map reported one area with maximum values that was located at the bifurcation region, approximately opposite to the side branch, and other areas with large tissue growth were mainly located at the distal portion. Whereas, the distribution of RRT was featured by moderate magnitude and larger values were found close to the bifurcation region.

The Case 7 was found with the highest level of restenosis, the contour map of the distance between lumen contours at 9-months follow-up is reported in Fig.6.20. The grid that was used to plot the values was defined so that the circumference of the vessel and a length of 31 mm were spanned. In Fig.6.20 four regions with high NIT were recognised and were related to the distribution of RRT. The dotted lines in Fig.6.20 defined the analysed portions of the scaffolded region and high values of RRT were found where the stent was malapposed, as well as at a spot with high superficial roughness of the lumen.

The map of the distance between lumen contours at the scaffolded segment of Case 8 is shown in Fig.6.21. The distance between the lumen contours was computed from the follow-up OCT acquisition. The grid that was used to plot the values was defined so that the circumference of the vessel and a length of 29 mm were spanned. The rectangles in Fig.6.21 depicts the position of the bifurcations, which were defined by the corresponding OCT frames and the range of pixels within each frame. Moderate values of distance between contours spread between the proximal and the side bifurcations regions, whereas minimum growing was recorder distally. Similarly, the distribution of RRT presented areas with higher values at the proximal portion and opposite to the side branch.

The map of the distance between lumen contours at the scaffolded segment of Case 9 is shown in Fig.6.22. The grid that was used to plot the values was defined so that the circumference of the vessel and a length of 24 mm were spanned. Three regions with higher values of distance between contours were identified along the scaffold. This was reflected by the distribution of RRT that presented areas with higher values at the proximal portion, opposite to the side branch and distally. Therefore, similarities between distributions were recorded which supported the possible correlations between hemodynamics and NIT.

The map of the distance between lumen contours at the scaffolded segment of Case 10 is shown in Fig.6.23. The grid that was used to plot the values was defined so that the circumference of the vessel and a length of 24 mm were spanned. Two regions with higher values of distance between contours were identified across the scaffold. Large areas with moderate vessel growth were found at the bifurcation and distally, whilst medium growth proximally. The vessel wall experienced high RRT mainly close the bifurcation, proximally and opposite to the side branch. There was coherence between the distributions, which again confirmed possible correlations between hemodynamics and NIT.

The map of the distance between lumen contours at the scaffolded segment of Case 11 is shown in Fig.6.24. The grid that was used to plot the values was defined so that the circumference of the vessel and a length of 29 mm were

spanned. Two regions with higher values of distance between contours were identified across the scaffold, respectively at the proximal region and from the bifurcation to the distal region. A detachment between the stent and the vessel was along the proximal region induced moderated and high RRT at the main branch surface. Whilst, low intima growth was found in the same region which again might lead to possible correlations between hemodynamics and NIT.

The map of the distance between lumen contours at the scaffolded segment of Case 12 is shown in Fig.6.25. The grid that was used to plot the values was defined so that the circumference of the vessel and a length of 19 mm were spanned. Three regions with higher values of distance between contours were identified at the proximal region, opposite to the bifurcation and at the distal region. Similarly, three portions of the main branch experienced moderate and high values of RRT as reported above. The scaffold was well in contact with the vessel wall, then the three-dimensional curvature and the distal variable cross-section area might have influenced the flow conditions.

The map of the distance between lumen contours at the scaffolded segment of Case 13 is shown in Fig.6.26. The grid that was used to plot the values was defined so that the circumference of the vessel and a length of 29 mm were spanned. Three regions with higher values of distance between contours were found at the proximal region, opposite to the bifurcation and at the distal region. Such results were in correlation with the distribution of RRT over the simulated cardiac cycle. The variation of cross-section area was probably the cause of local flow recirculation and NIT.

The map of the distance between lumen contours at the scaffolded segment of Case 14 is shown in Fig.6.27. The grid that was used to plot the values was defined so that the circumference of the vessel and a length of 29 mm were pictured. Three regions with higher values of distance between contours were found at the proximal region and opposite to the two bifurcations. These last were reflected by the distribution of RRT over the simulated cardiac cycle, which were induced by malapposed stent struts and by variation of lumen cross-section area.

The map of the distance between lumen contours at the main branch segment of Case 15 is shown in Fig.6.28. The grid that was used to plot the values was defined so that the circumference of the vessel and a length of 19 mm were pictured. Two areas that experienced large values of distance between contours were opposite to the bifurcation and at the distally the side branch. The superficial RRT resembled such map with moderate levels of flow recirculation and stagnation.

The map of the distance between contours at the main branch segment of Case

16 is shown in Fig.6.29. The grid that was used to plot the values was defined so that the circumference of the vessel and a length of 19 mm were pictured. In this case the stent struts were covered by the intima, as the pattern of moderate wall growth resembled the implanted scaffold. Three areas with large values of growth were opposite to the bifurcations and at the proximal to the side branch. The superficial RRT resembled such map with moderate values close to the stent struts and wider areas opposite the bifurcations.

6.5 Discussion

A validated OCT-based reconstruction methodology was employed to analyze the blood flow pattern in 12 patients that underwent PCI and the implantation of an Absorb BVS in the main branch at a coronary artery bifurcation. The actual configuration of the implanted scaffold was part of the physical domain and patients' hemodynamics was simulated with a commercial CFD software. Then, it was demonstrated: *i)* the possibility of calculating the WSS distribution and blood flow patterns in bifurcation segments treated with an Absorb BVS; *ii)* the potential application of such simulations in the clinical setting by matching the numerical methods with imaging and clinical outcomes in patients. The proposed approach might improve the understanding of the hemodynamic impact of any scaffold design at coronary bifurcations. The additional 9-months follow-up intravascular images enabled the quantification of vessel remodelling after the implantation of a bioresorbable scaffold when treating non-complex bifurcations with a provisional strategy.

The main findings were in agreement with the literature. Results in the work of Himburg and co-authors (Himburg et al., 2004) reported that the variation in the permeability of the endothelium can be explained as a residence time effect, that is a combination of TAWSS and OSI. Indeed, the RRT accounts for both high oscillation of WSS and low values of averaged WSS over a cardiac cycle. Each patient was characterised by distinctive patterns of arterial wall growth and hemodynamics. Objectives of a future study can be a punctual comparison between NIT and hemodynamic quantities at the wall, seeking detailed information about the relationship between variation of endothelium permeability and WSS distribution.

In the literature, the effect of the implanted Absorb BVS on WSS has been limited to relatively straight coronary vessels without bifurcations and the CFD physical domain did not include the scaffold, as the innermost lumen boundary was traced. Karanasos and colleagues (Karanasos et al., 2015) evaluated the

effect of WSS after two years from the intervention in the scaffolded segment. Results were compared with the vascular healing response of eight patients from the ABSORB A cohort that underwent 5-year invasive follow-up OCT acquisition. It was found that regions exposed to low shear stress had thinner fibrous caps. In 12 patients from the ABSORB B cohort, Bourantas and colleagues (Bourantas et al., 2014a) investigated the effect of WSS after BVS implantation on neointimal growth at 1 year. Similar to studies with metal stents, areas that were exposed to low WSS showed more intimal thickening at follow up. Analysis of the peri-strut flow distribution showed regions of low WSS as well as recirculation zones on both sides of the struts and regions of high WSS at the top. This hemodynamic profile may explain the higher thrombotic rate of the Absorb BVS compared to drug eluting stents (Serruys et al., 2016). One of the postulated mechanisms is the activation of platelets induced by high WSS on top of struts and sequestration in low recirculation zones adjacent to struts causing thrombus formation (Serruys et al., 2015).

According to the most recent computational works about the application of polymeric bioresorbable scaffolds, such as the work of Thondapu and co-authors (Thondapu et al., 2018), and the review presented by Chiastra and colleagues (Chiastra et al., 2017a), the study here described is the first that includes the reconstruction of coronary bifurcations with an implanted scaffold, whose actual deployed configuration was included in the model (Migliori et al., 2017). Nevertheless, the applied method has limitations related to the periodic deformation of the coronary artery that affects the change of lumen cross-section area during the OCT pullback. Moreover, rigid wall conditions, with the coronary artery model fixed in the space domain, were assumed for the CFD simulation. Although it has been shown that the assumption of rigid walls is acceptable in case of stented geometries (Chiastra et al., 2014), it is still unclear whether the coronary motion due to heart contraction can be neglected (Chiastra et al., 2017a). The performed CFD simulation resembled the flow condition at baseline and the scaffold degradation was not modeled. Intuitively, the progressive reduction of scaffold struts cross-section area can influence the local flow conditions. However, it can be argued that flow condition at baseline plays an important role in the initiation of scaffold degradation and vessel wall remodeling (Bourantas et al., 2014a). Finally, it was not possible to associate each baseline and follow-up OCT images to compute the neo-intima thickening. Hence, we defined the baseline lumen contour from the follow-up OCT image dataset, as done in a previous study (Bourantas et al., 2014a).

6.6 Conclusions

The present study illustrated the use of a patient-specific technique to model blood flow in a scaffolded coronary bifurcation segment. The described approach provided valuable complementary information, which might improve the clinical outcomes in this subset of coronary artery diseases.

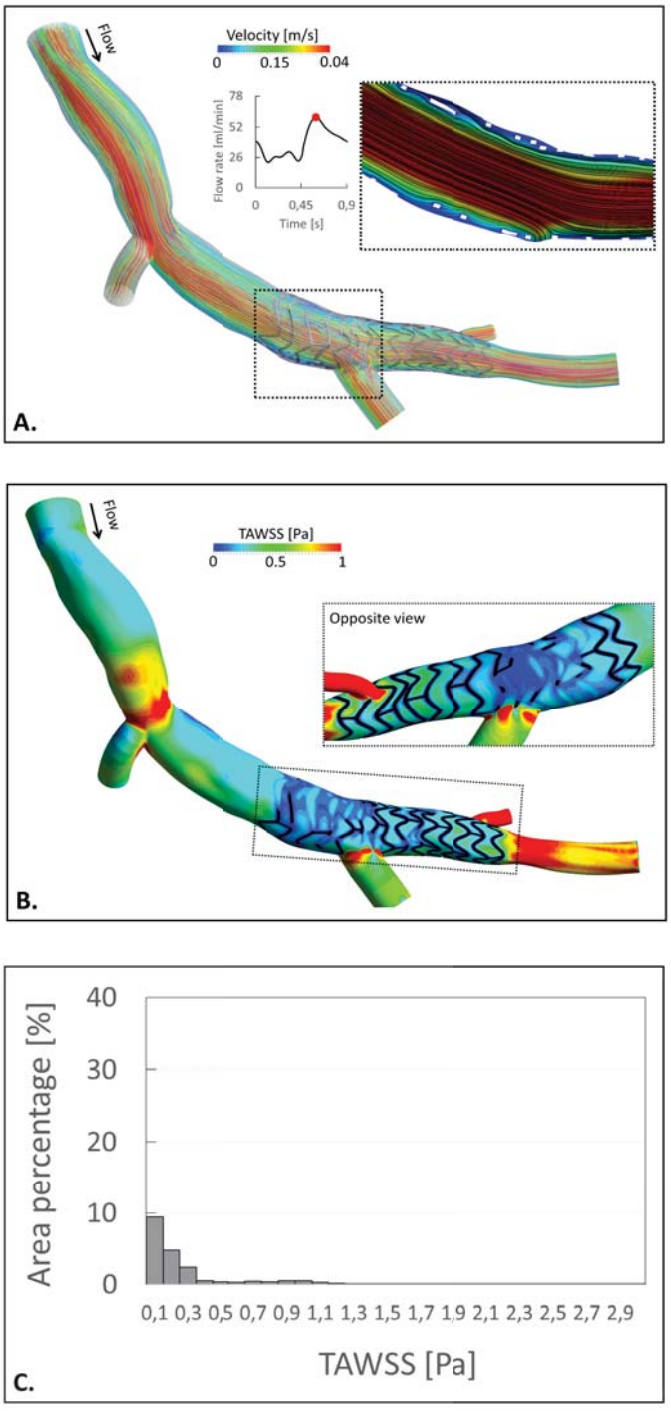

Figure 6.5 Results from the simulated blood flow of Case 5. A: Streamlines of the velocity coloured by the velocity magnitude and the in-plane velocity contour-map with in-plane streamlines at peak for flow rate. B: Contour map of the time-averaged wall shear stress (TAWSS) over the simulated cardiac cycle with an enlargement of the opposite view of the bifurcation. C: Histograms of the scaffolded surface percentage area under intervals of TAWSS from 0 Pa and 3 Pa.

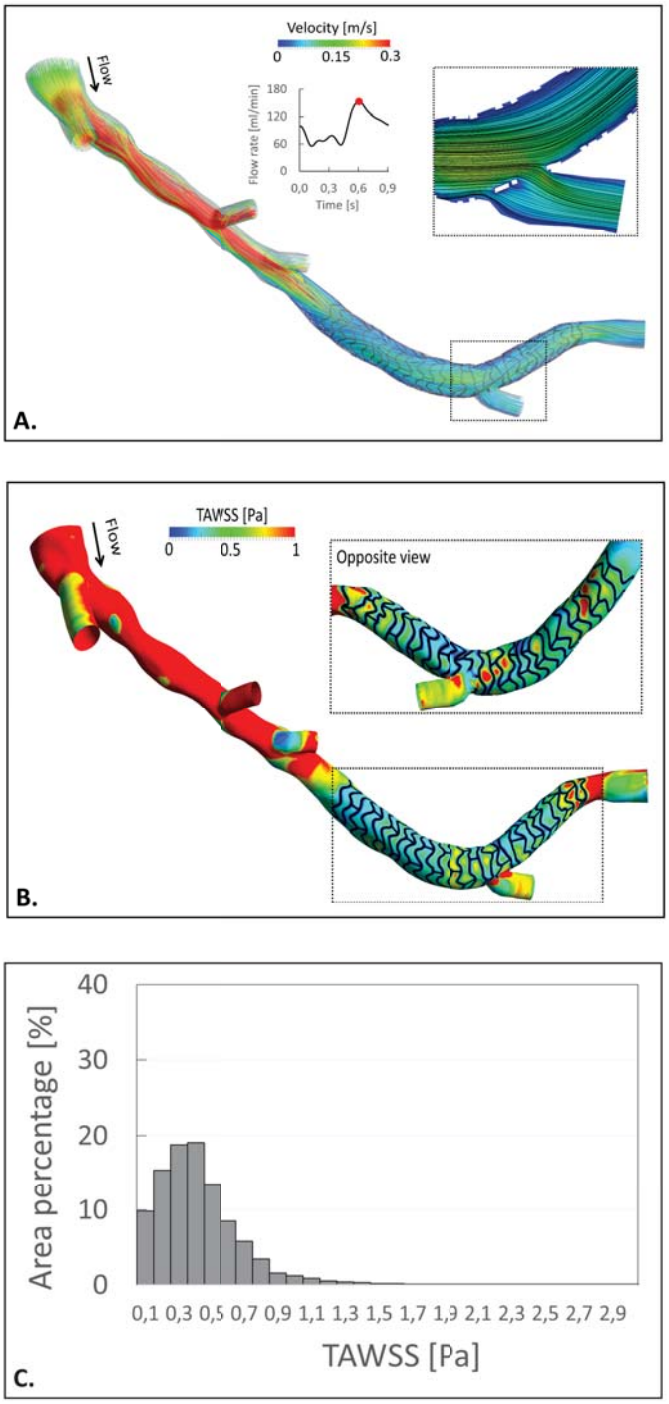

Figure 6.6 Results from the simulated blood flow of Case 6. A: Streamlines of the velocity coloured by the velocity magnitude and the in-plane velocity contour-map with in-plane streamlines at peak for flow rate. B: Contour map of the time-averaged wall shear stress (TAWSS) at the end of the simulated cardiac cycle with an enlargement of the opposite view of the bifurcation. C: Histograms of the scaffolded surface percentage area under intervals of TAWSS from 0 Pa and 3 Pa.

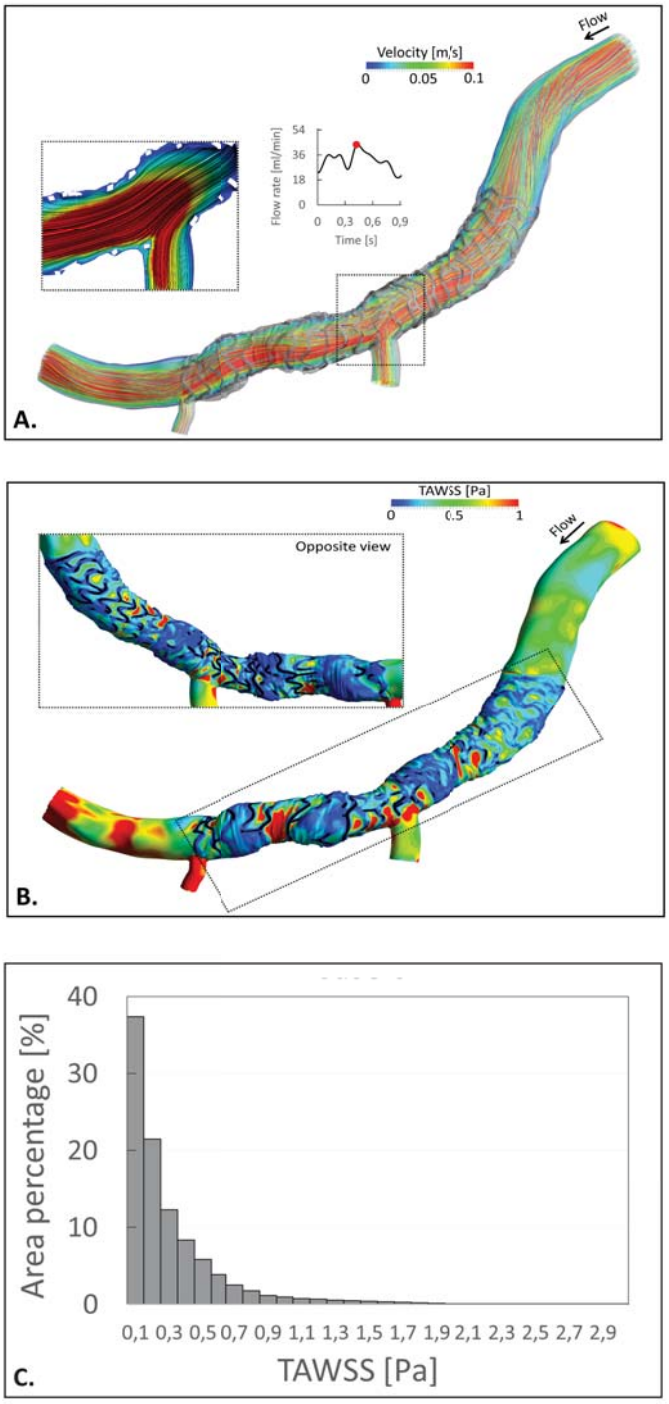

Figure 6.7 Results from the simulated blood flow of Case 7. A: Streamlines of the velocity coloured by the velocity magnitude and the in-plane velocity contour-map with in-plane streamlines at peak for flow rate. B: Contour map of the time-averaged wall shear stress (TAWSS) at the end of the simulated cardiac cycle with an enlargement of the opposite view of the bifurcation. C: Histograms of the scaffolded surface percentage area under intervals of TAWSS from 0 Pa and 3 Pa.

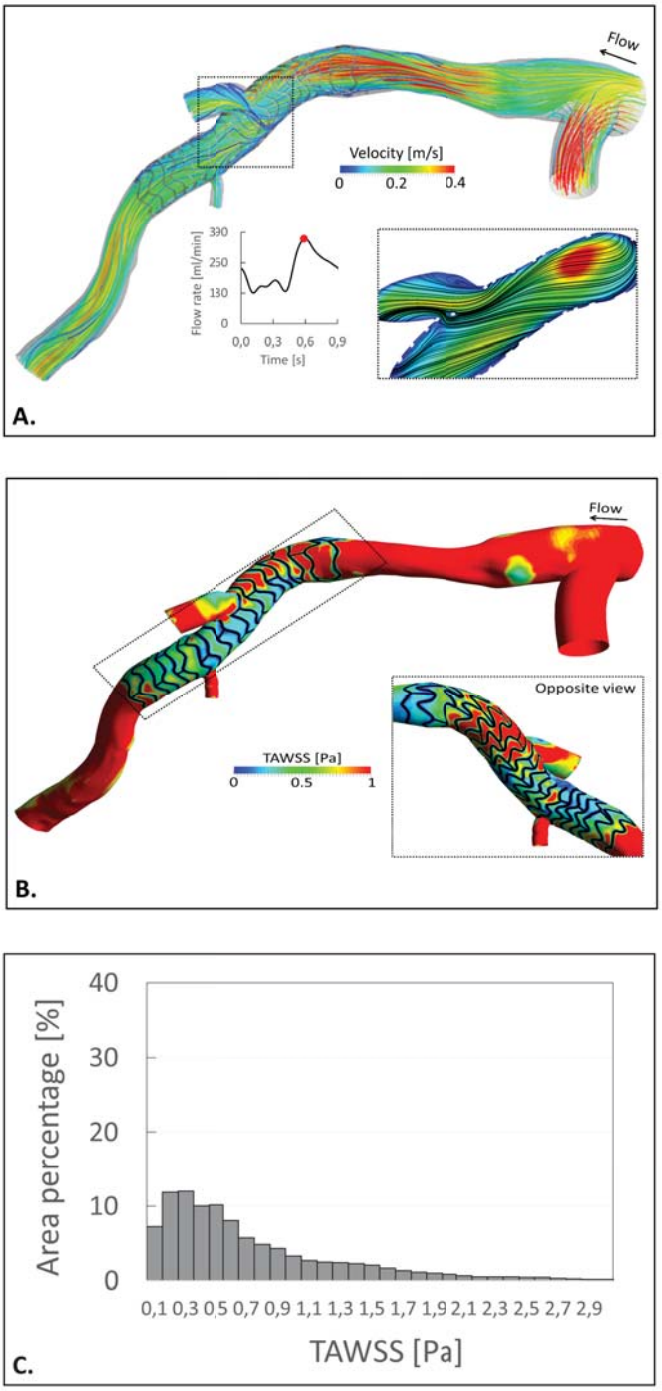

Figure 6.8 Results from the simulated blood flow of Case 8. A: Streamlines of the velocity coloured by the velocity magnitude and the in-plane velocity contour-map with in-plane streamlines at peak for flow rate. B: Contour map of the time-averaged wall shear stress (TAWSS) at the end of the simulated cardiac cycle with an enlargement of the opposite view of the bifurcation. C: Histograms of the scaffolded surface percentage area under intervals of TAWSS from 0 Pa and 3 Pa.

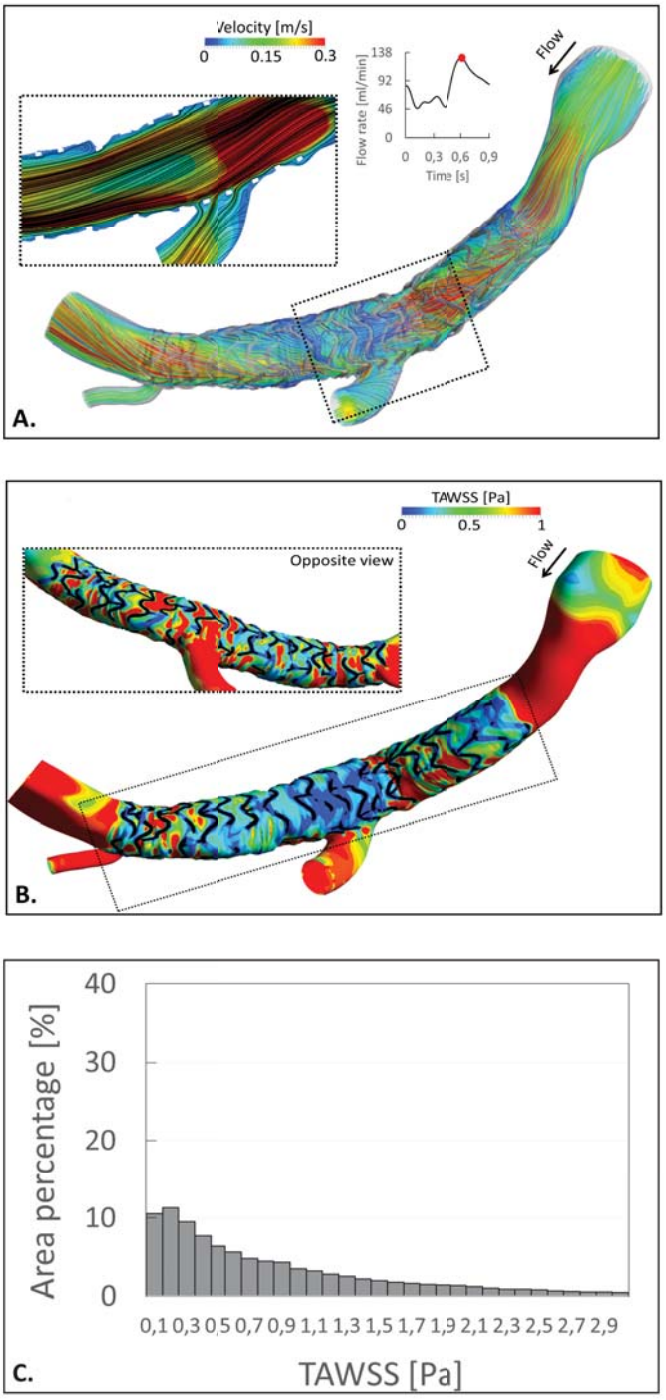

Figure 6.9 Results from the simulated blood flow of Case 9. A: Streamlines of the velocity coloured by the velocity magnitude and the in-plane velocity contour-map with in-plane streamlines at peak for flow rate. B: Contour map of the time-averaged wall shear stress (TAWSS) at the end of the simulated cardiac cycle with an enlargement of the opposite view of the bifurcation. C: Histograms of the scaffolded surface percentage area under intervals of TAWSS from 0 Pa and 3 Pa.

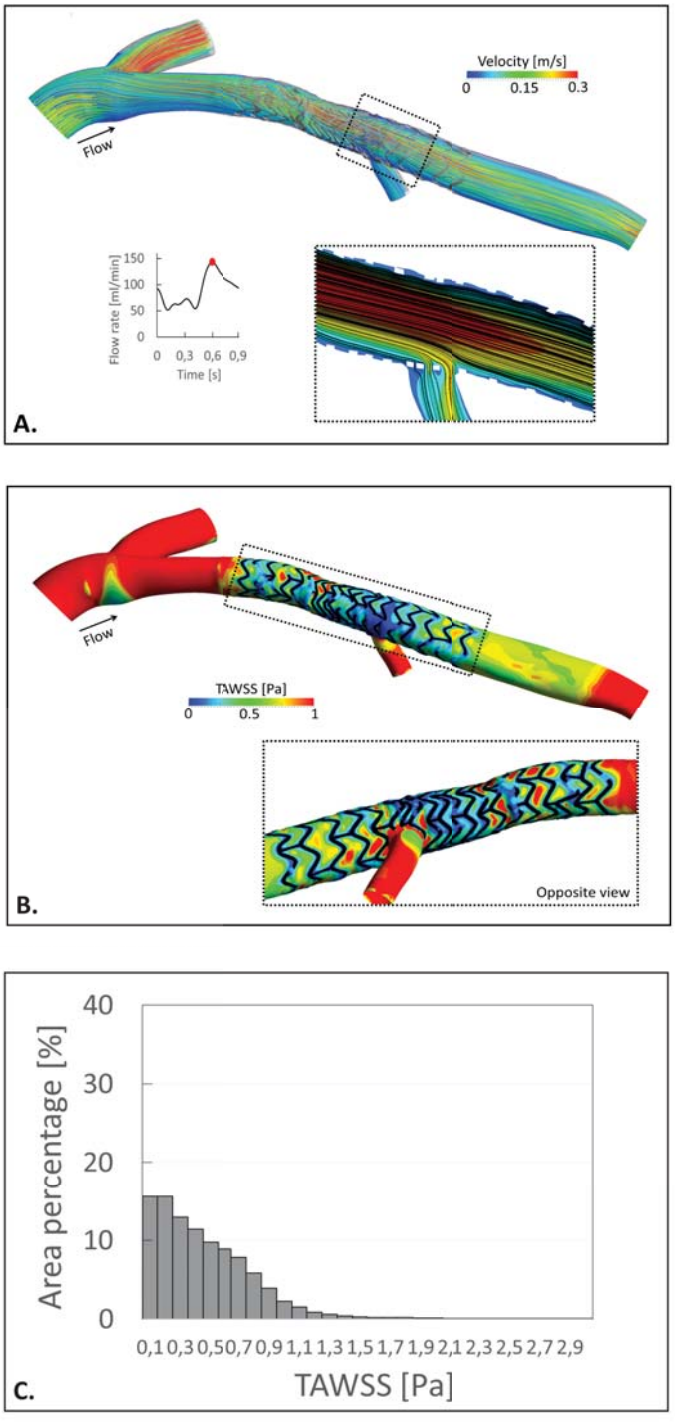

Figure 6.10 Results from the simulated blood flow of Case 10. A: Streamlines of the velocity coloured by the velocity magnitude and the in-plane velocity contour-map with in-plane streamlines at peak for flow rate. B: Contour map of the time-averaged wall shear stress (TAWSS) at the end of the simulated cardiac cycle with an enlargement of the opposite view of the bifurcation. C: Histograms of the scaffolded surface percentage area under intervals of TAWSS from 0 Pa and 3 Pa.

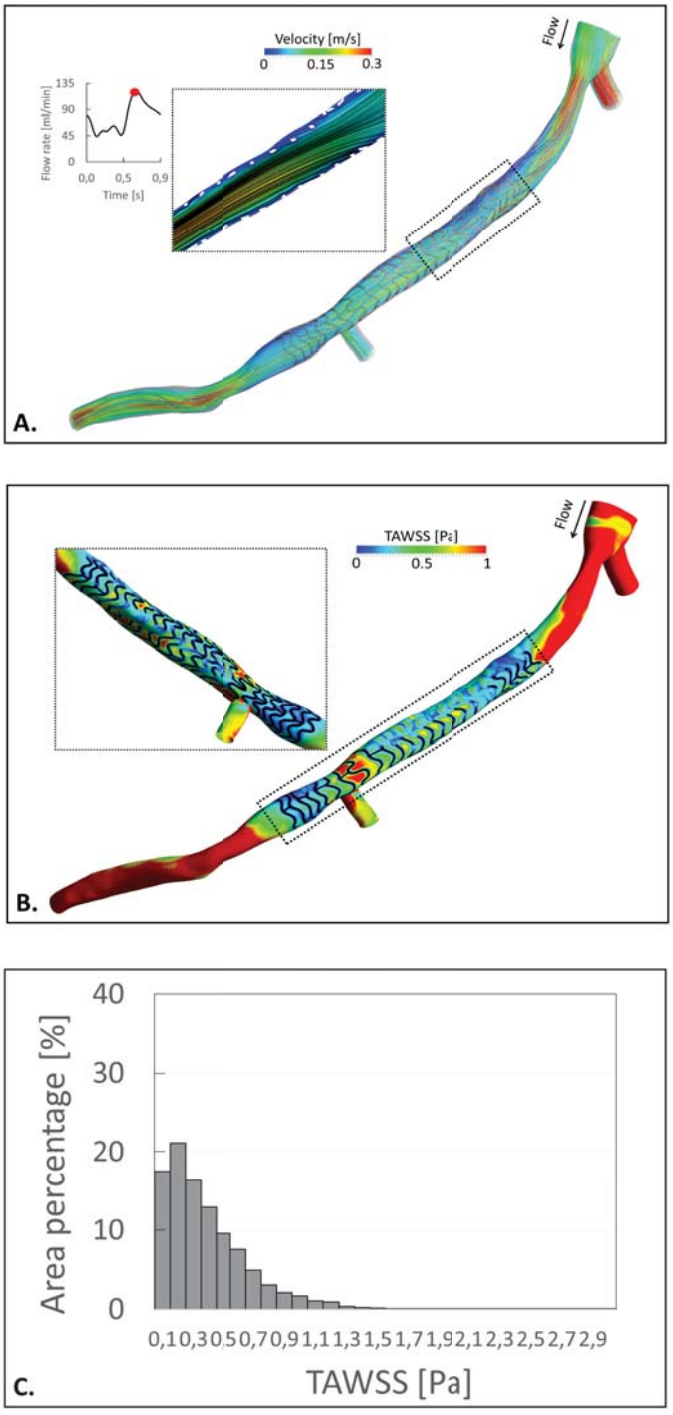

Figure 6.11 Results from the simulated blood flow of Case 11. A: Streamlines of the velocity coloured by the velocity magnitude and the in-plane velocity contour-map with in-plane streamlines at peak for flow rate. B: Contour map of the time-averaged wall shear stress (TAWSS) at the end of the simulated cardiac cycle with an enlargement of the opposite view of the bifurcation. C: Histograms of the scaffolded surface percentage area under intervals of TAWSS from 0 Pa and 3 Pa.

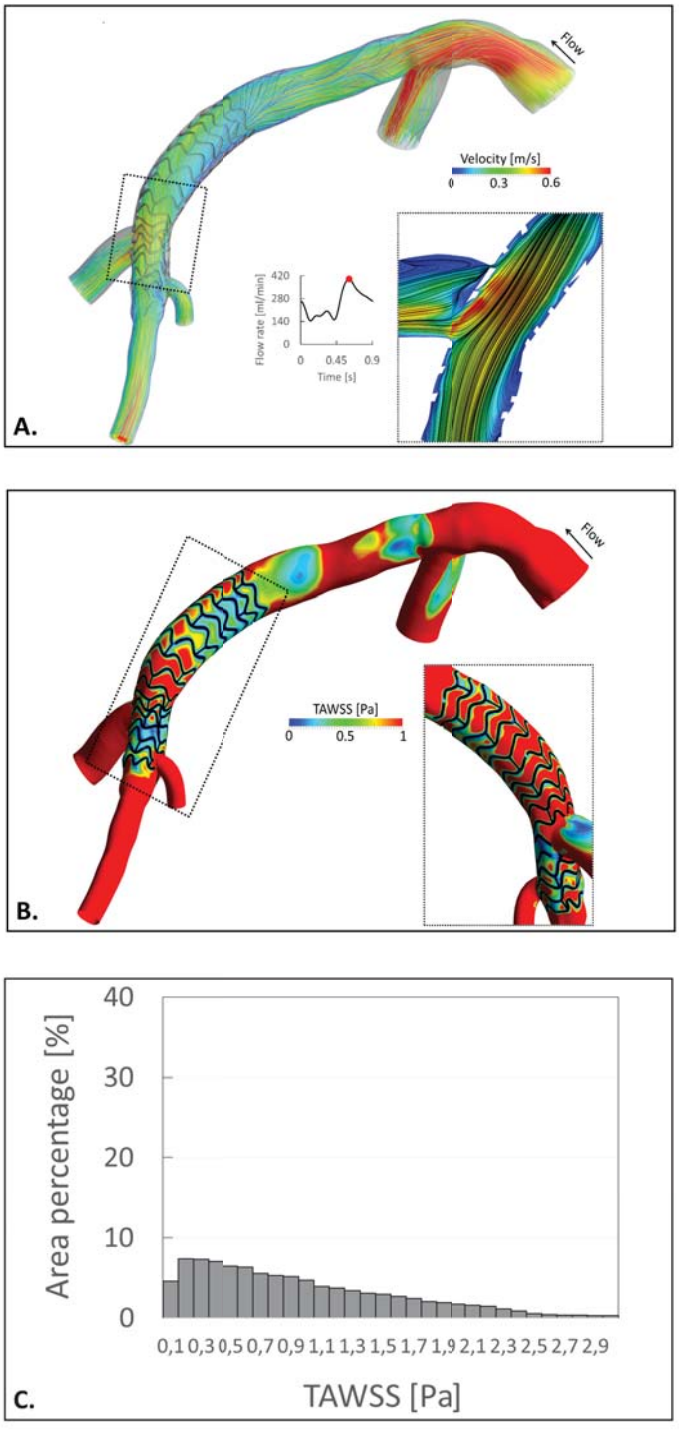

Figure 6.12 Results from the simulated blood flow of Case 12. A: Streamlines of the velocity coloured by the velocity magnitude) and the in-plane velocity contour-map with in-plane streamlines at peak for flow rate. B: Contour map of the time-averaged wall shear stress (TAWSS) at the end of the simulated cardiac cycle with an enlargement of the opposite view of the bifurcation. C: Histograms of the scaffolded surface percentage area under intervals of TAWSS from 0 Pa and 3 Pa.

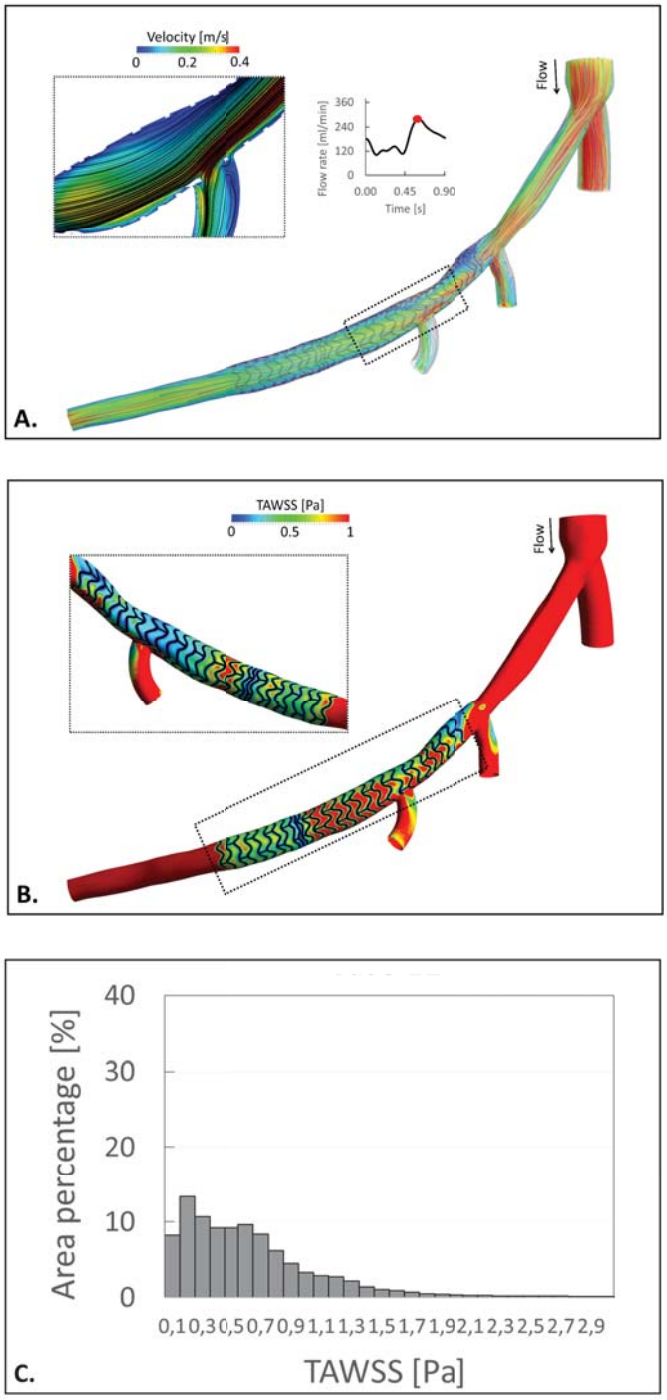

Figure 6.13 Results from the simulated blood flow of Case 13. A: Streamlines of the velocity coloured by the velocity magnitude and the in-plane velocity contour-map with in-plane streamlines at peak for flow rate. B: Contour map of the time-averaged wall shear stress (TAWSS) at the end of the simulated cardiac cycle with an enlargement of the opposite view of the bifurcation. C: Histograms of the scaffolded surface percentage area under intervals of TAWSS from 0 Pa and 3 Pa.

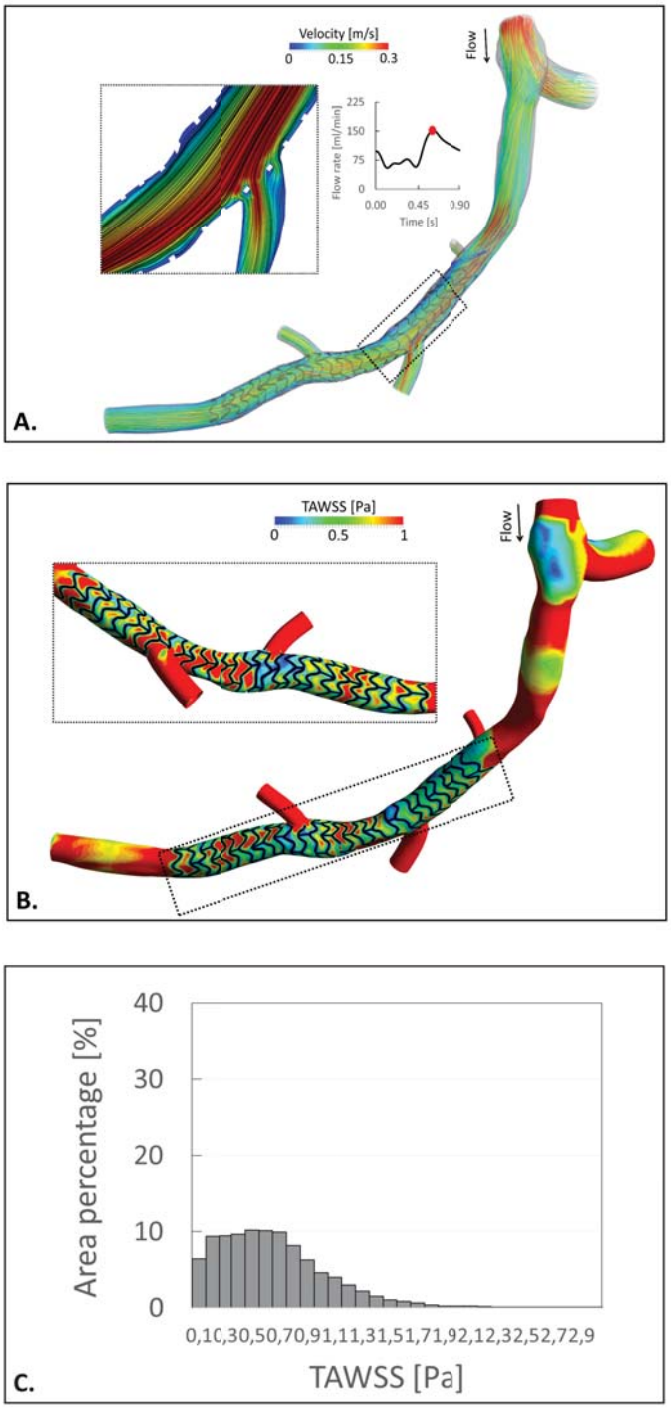

Figure 6.14 Results from the simulated blood flow of Case 14. A: Streamlines of the velocity coloured by the velocity magnitude and the in-plane velocity contour-map with in-plane streamlines at peak for flow rate. B: Contour map of the time-averaged wall shear stress (TAWSS) at the end of the simulated cardiac cycle with an enlargement of the opposite view of the bifurcation. C: Histograms of the scaffolded surface percentage area under intervals of TAWSS from 0 Pa and 3 Pa.

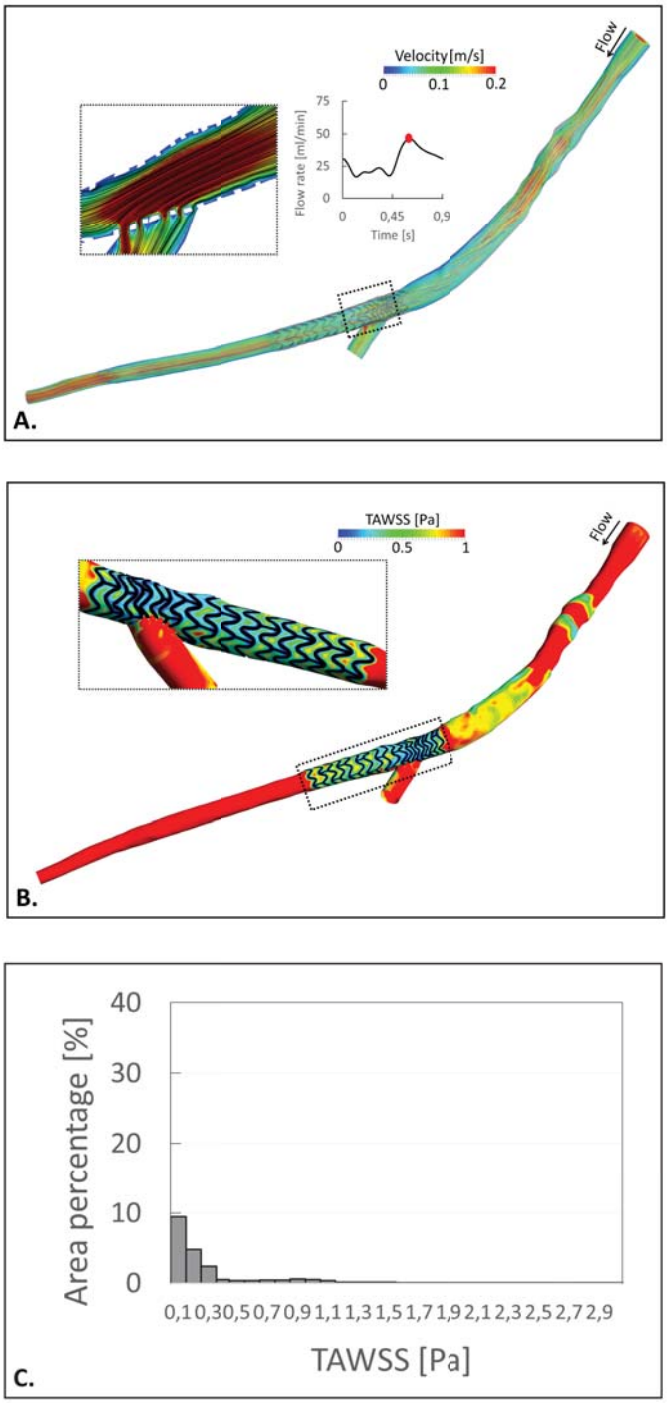

Figure 6.15 Results from the simulated blood flow of Case 15. A: Streamlines of the velocity coloured by the velocity magnitude and the in-plane velocity contour-map with in-plane streamlines at peak for flow rate. B: Contour map of the time-averaged wall shear stress (TAWSS) at the end of the simulated cardiac cycle with an enlargement of the opposite view of the bifurcation. C: Histograms of the scaffolded surface percentage area under intervals of TAWSS from 0 Pa and 3 Pa.

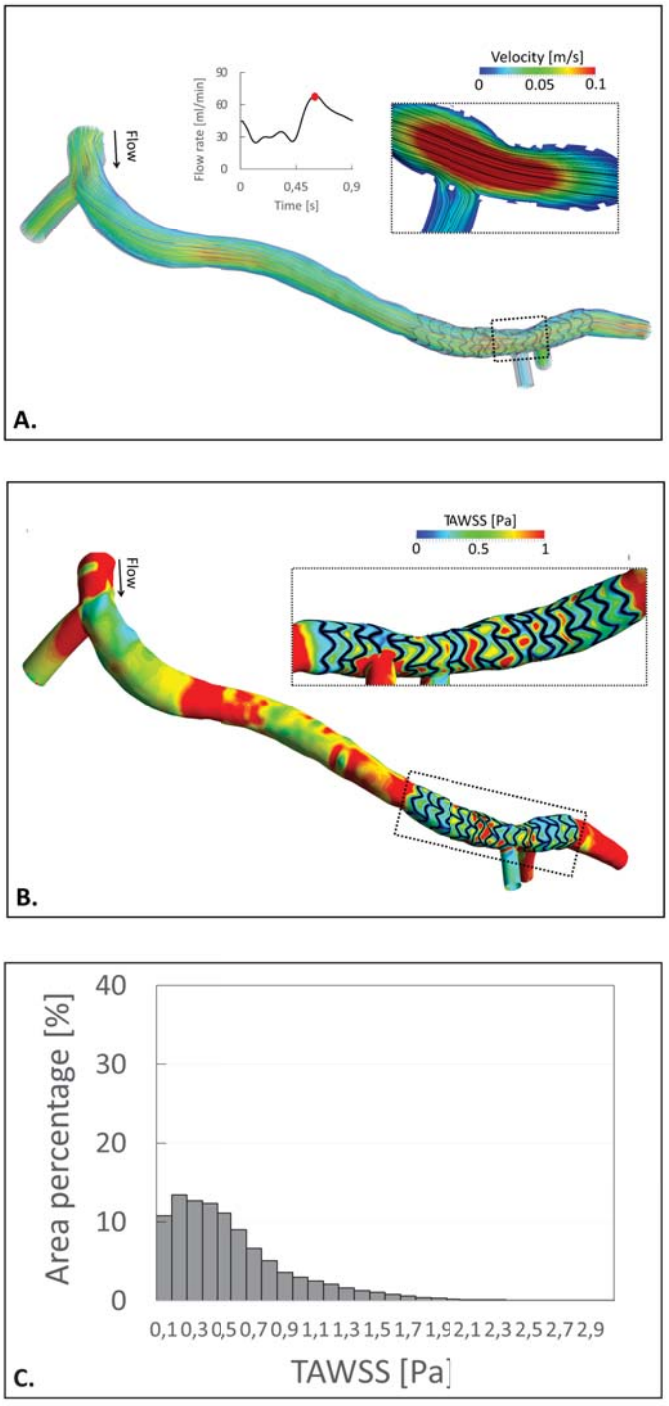

Figure 6.16 Results from the simulated blood flow of Case 16. A: Streamlines of the velocity coloured by the velocity magnitude and the in-plane velocity contour-map with in-plane streamlines at peak for flow rate. B: Contour map of the time-averaged wall shear stress (TAWSS) at the end of the simulated cardiac cycle with an enlargement of the opposite view of the bifurcation. C: Histograms of the scaffolded surface percentage area under intervals of TAWSS from 0 Pa and 3 Pa.

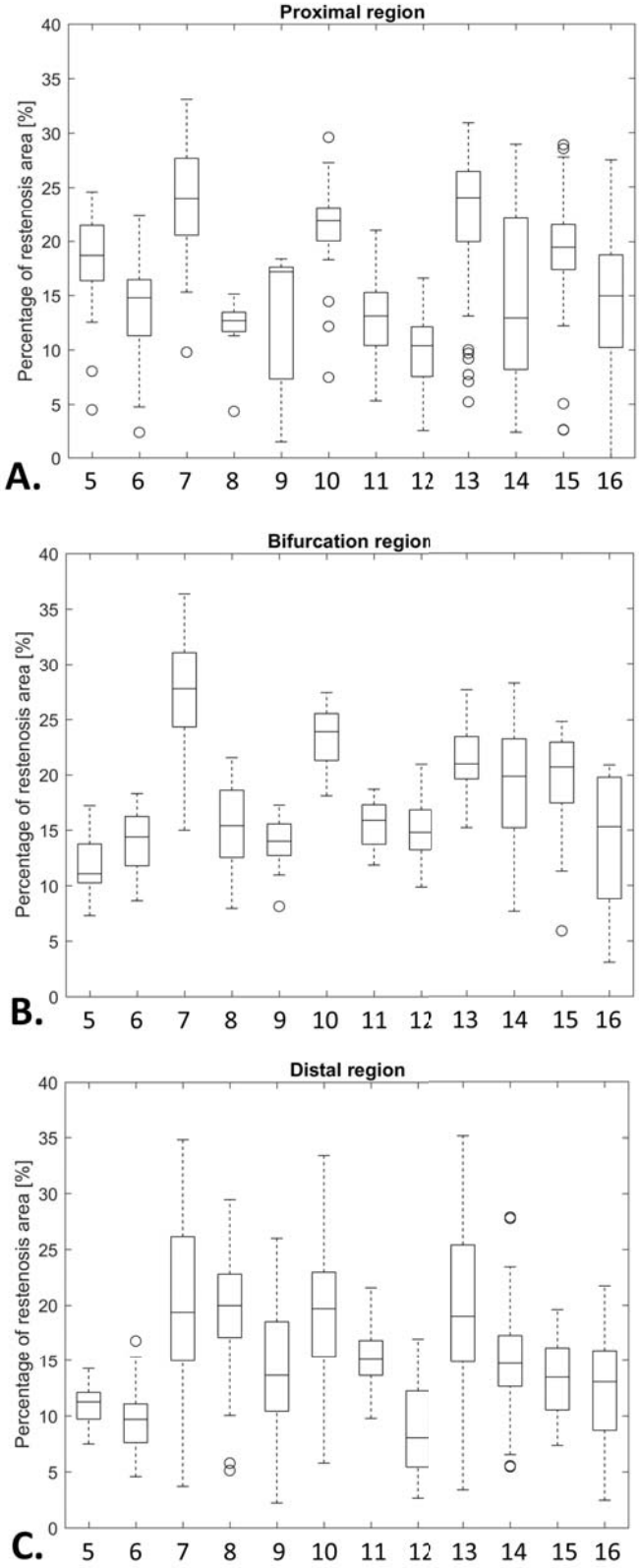

Figure 6.17 Boxplots of the computed neo-intima thickening of all the treated cases. The regions proximal (A), side branch (B) and distal (C) of the scaffolded segment were reported.

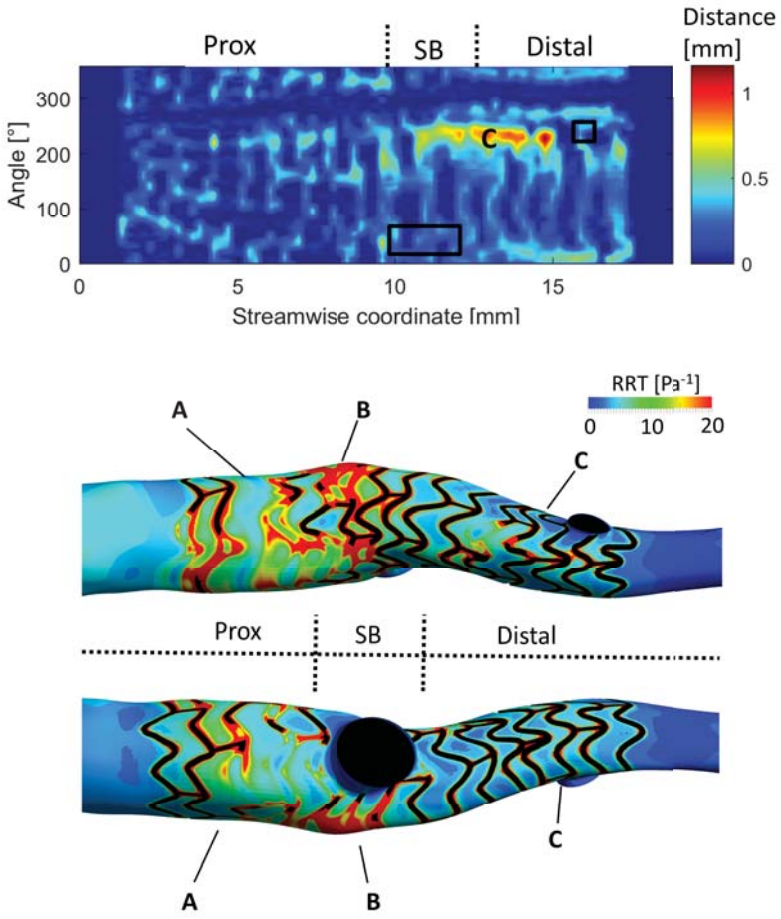

Figure 6.18 Comparison between artery wall remodelling and superficial hemodynamic quantity of Case 5. Distance between 9-months follow-up and baseline lumen contours at the scaffolded segment, a region with high neo-intimal thickening were recognised along the acquisition (C), and the rectangles defined the position of the bifurcations and the dotted line divides the front side and the back side of the vessel (Top map). Contour map of the residual residence time (RRT) that was computed over the simulated cardiac circle, both at the front and back sides of the vessel. Three regions with high RRT were recognised along the stented blood vessel (A,B,C) (Bottom map).

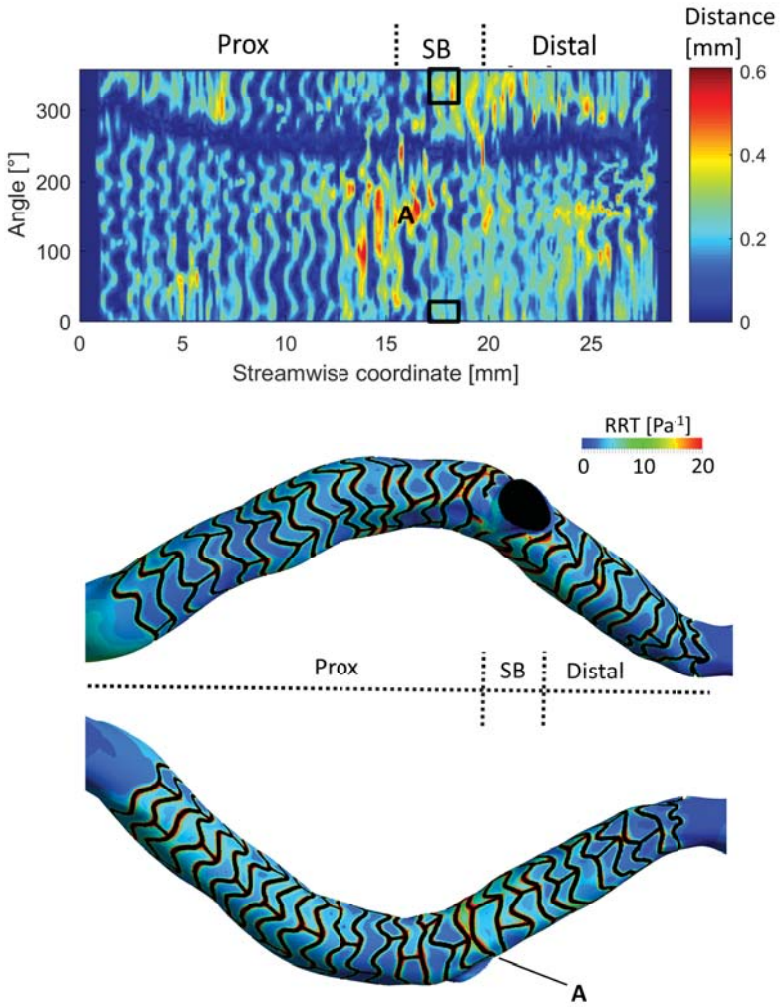

Figure 6.19 Comparison between artery wall remodelling and superficial hemodynamic quantity of Case 6. Distance between 9-months follow-up and baseline lumen contours at the scaffolded segment, a region with high neo-intimal thickening were recognised along the acquisition (A), and the rectangles defined the position of the bifurcations and the dotted line divides the front side and the back side of the vessel (Top map). Contour map of the residual residence time (RRT) that was computed over the simulated cardiac circle, both at the front and back sides of the vessel. One region with high RRT were recognised along the stented blood vessel (A) (Bottom map).

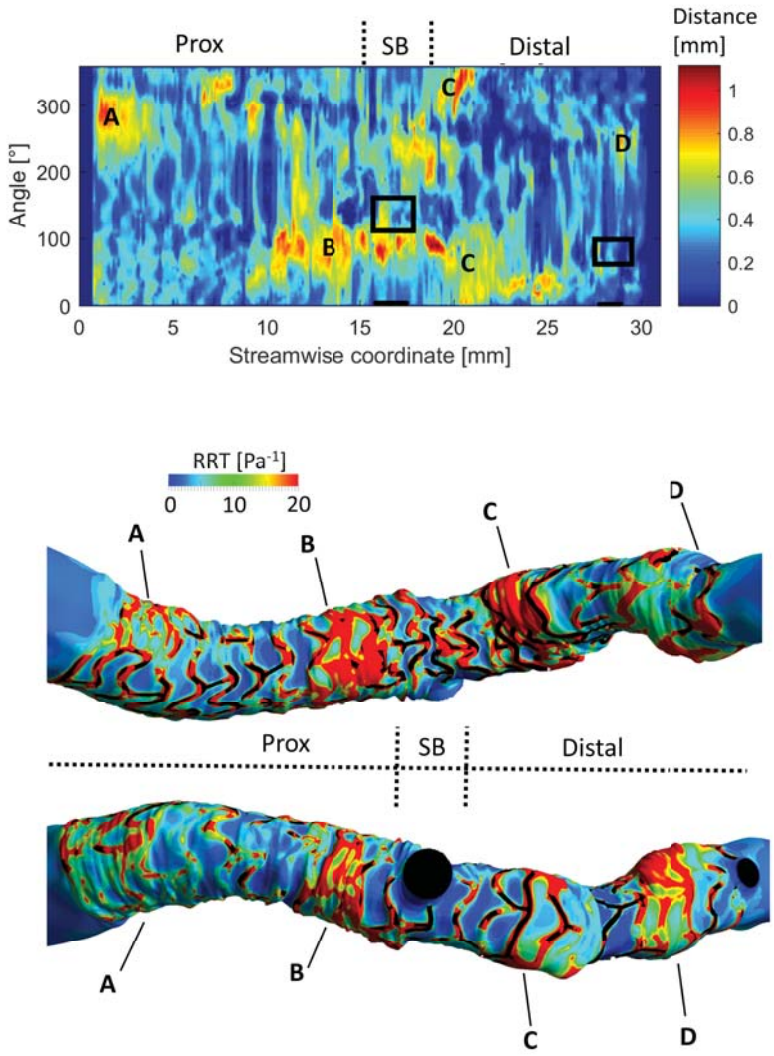

Figure 6.20 Comparison between artery wall remodelling and superficial hemodynamic quantity of Case 7. Distance between 9-months follow-up and baseline lumen contours at the scaffolded segment, regions with high neo-intimal thickening were recognised along the acquisition (A,B,C,D), and the rectangles defined the position of the bifurcations and the dotted line divides the front side and the back side of the vessel (Top map). Contour map of the residual residence time (RRT) that was computed over the simulated cardiac circle, both at the front and back sides of the vessel. Four regions with high RRT were recognised along the stented blood vessel (A,B,C,D) (Bottom map).

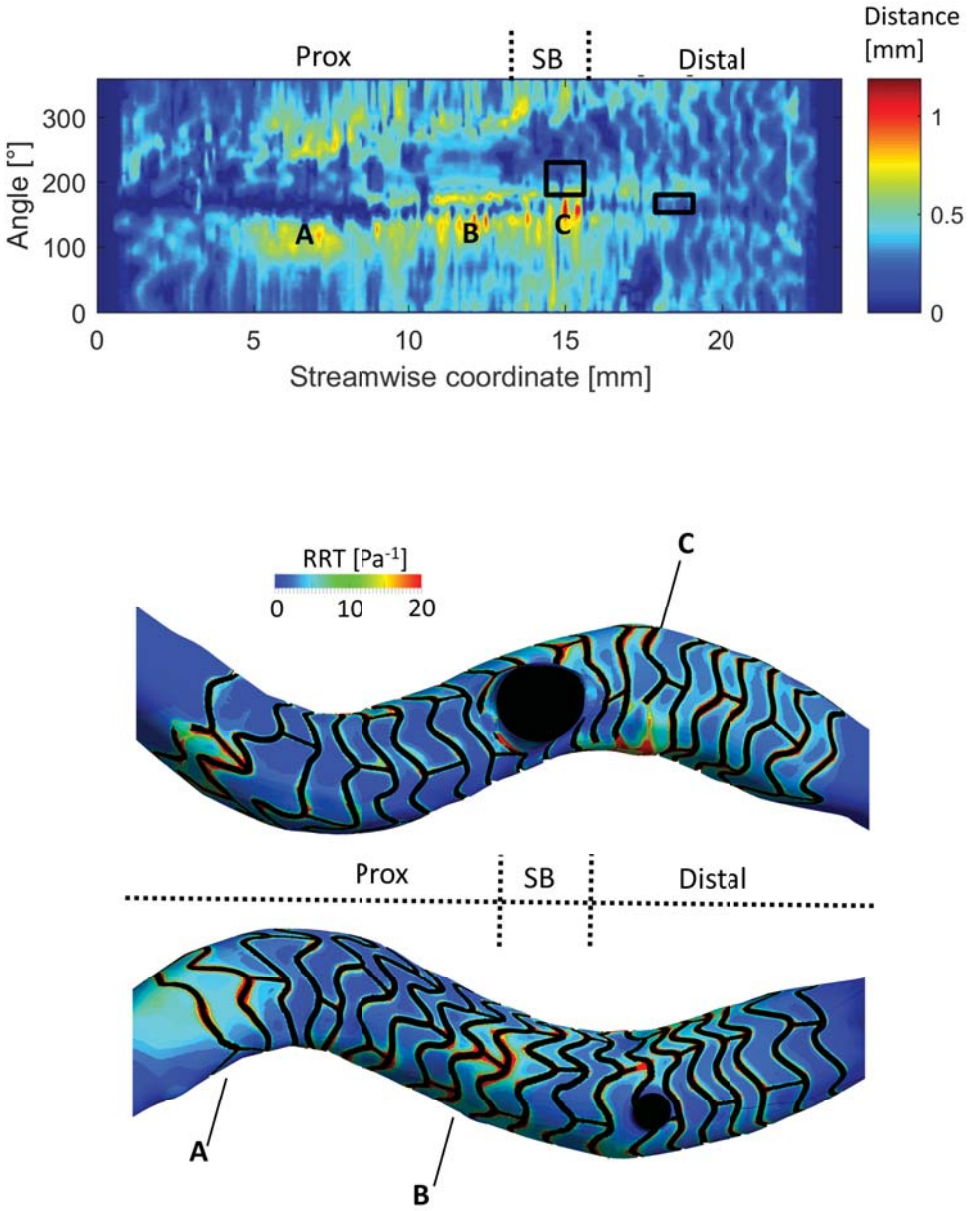

Figure 6.21 Comparison between artery wall remodelling and superficial hemodynamic quantity of Case 8. Distance between 9-months follow-up and baseline lumen contours at the scaffolded segment, regions with high neo-intimal thickening were recognised along the acquisition (A,B,C), and the rectangles defined the position of the bifurcations and the dotted line divides the front side and the back side of the vessel (Top map). Contour map of the residual residence time (RRT) that was computed over the simulated cardiac circle, both at the front and back sides of the vessel. Three regions with high RRT were recognised along the stented blood vessel (A,B,C) (Bottom map).

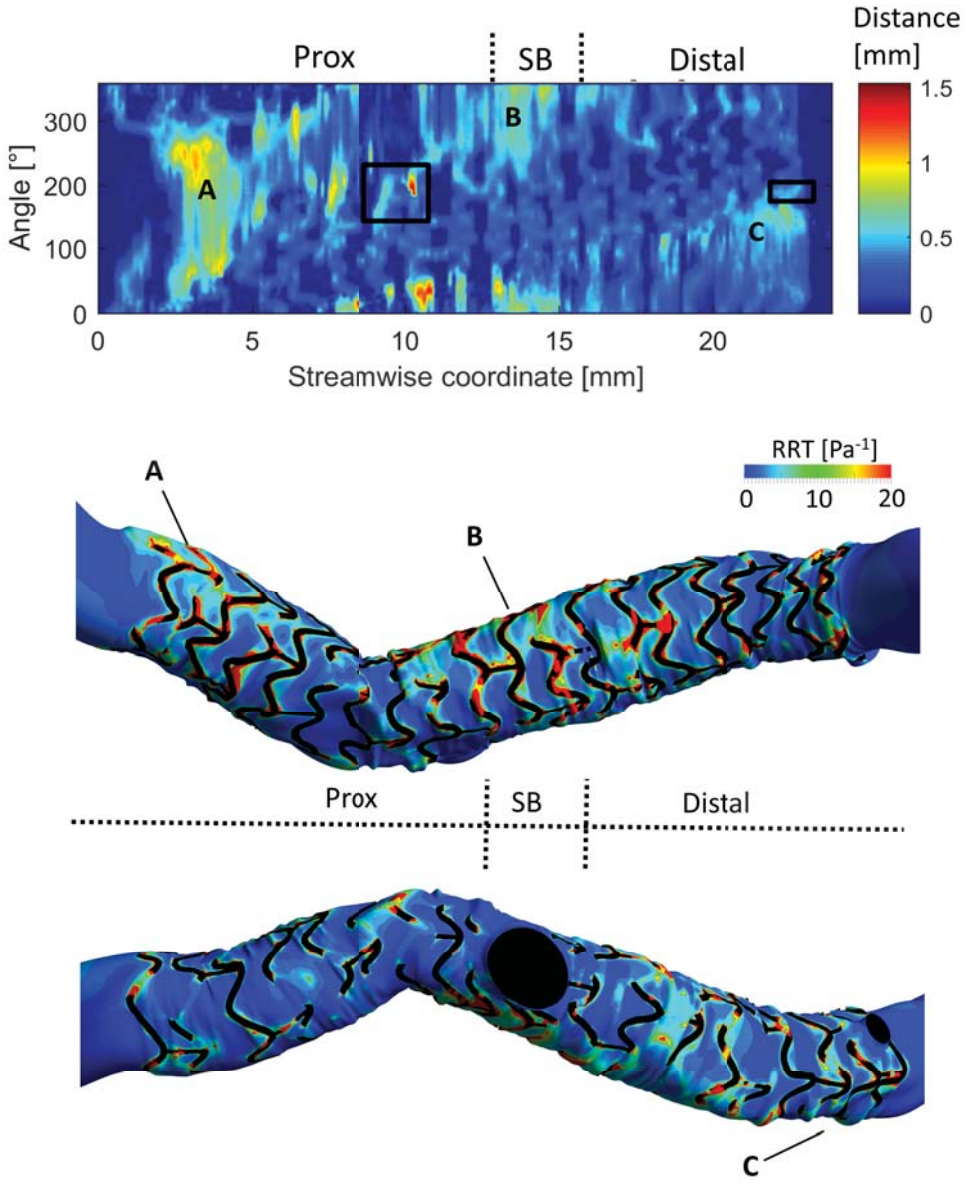

Figure 6.22 Comparison between artery wall remodelling and superficial hemodynamic quantity of Case 9. Distance between 9-months follow-up and baseline lumen contours at the scaffolded segment, regions with high neo-intimal thickening were recognised along the acquisition (A,B,C), and the rectangles defined the position of the bifurcations and the dotted line divides the front side and the back side of the vessel (Top map). Contour map of the residual residence time (RRT) that was computed over the simulated cardiac circle, both at the front and back sides of the vessel. Three regions with high RRT were recognised along the stented blood vessel (A,B,C) (Bottom map).

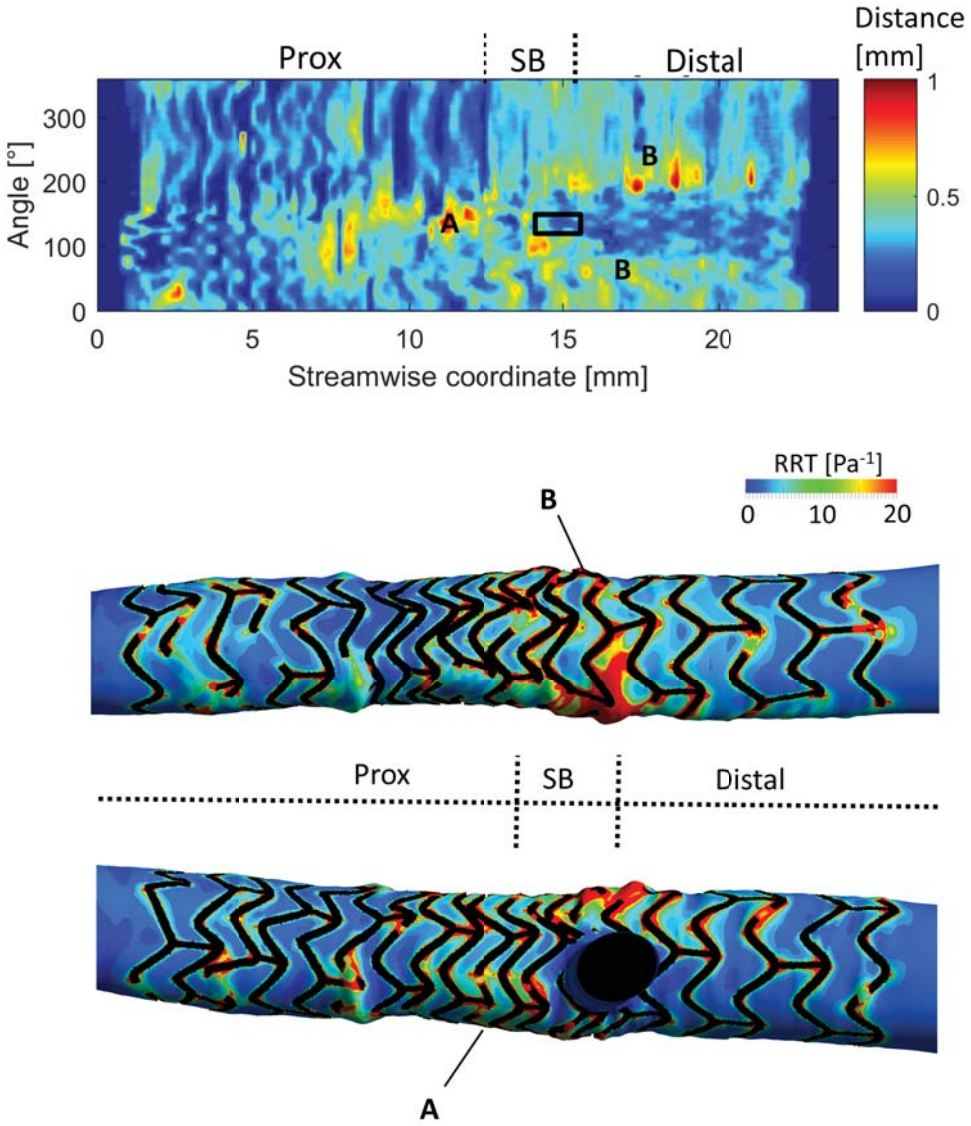

Figure 6.23 Comparison between artery wall remodelling and superficial hemodynamic quantity of Case 10. Distance between 9-months follow-up and baseline lumen contours at the scaffolded segment, regions with high neo-intimal thickening were recognised along the acquisition (A,B), and the rectangles defined the position of the bifurcations and the dotted line divides the front side and the back side of the vessel (Top map). Contour map of the residual residence time (RRT) that was computed over the simulated cardiac circle, both at the front and back sides of the vessel. Two regions with high RRT were recognised along the stented blood vessel (A,B) (Bottom map).

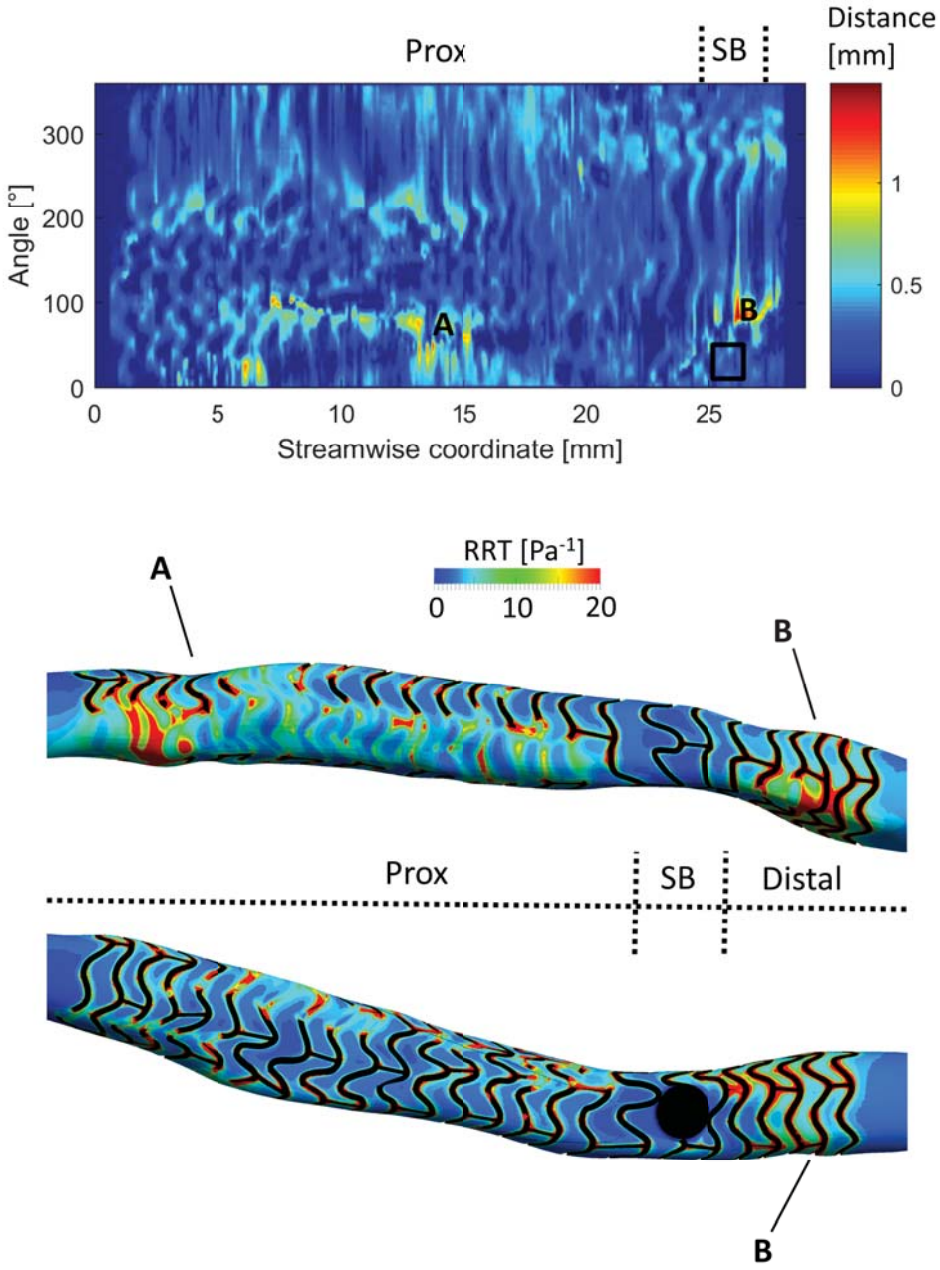

Figure 6.24 Comparison between artery wall remodelling and superficial hemodynamic quantity of Case 11. Distance between 9-months follow-up and baseline lumen contours at the scaffolded segment, regions with high neo-intimal thickening were recognised along the acquisition (A,B), and the rectangles defined the position of the bifurcations and the dotted line divides the front side and the back side of the vessel (Top map). Contour map of the residual residence time (RRT) that was computed over the simulated cardiac circle, both at the front and back sides of the vessel. Two regions with high RRT were recognised along the stented blood vessel (A,B) (Bottom map).

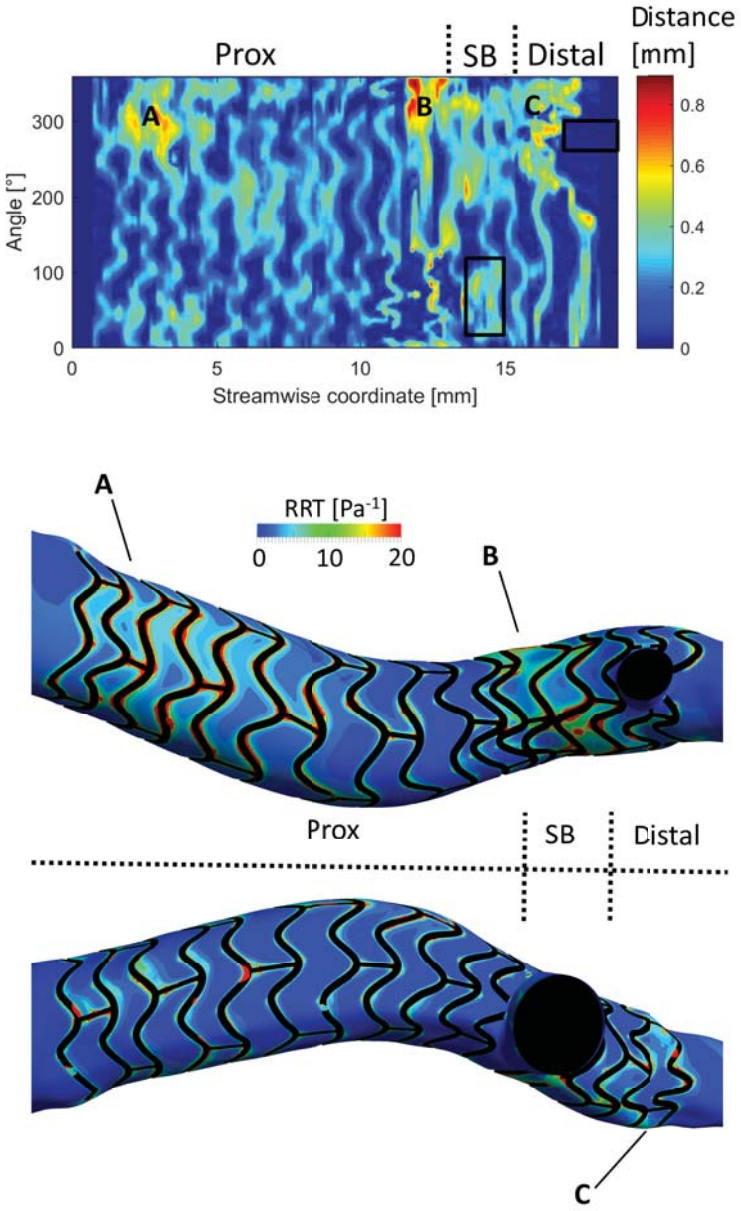

Figure 6.25 Comparison between artery wall remodelling and superficial hemodynamic quantity of Case 12. Distance between 9-months follow-up and baseline lumen contours at the scaffolded segment, regions with high neo-intimal thickening were recognised along the acquisition (A,B,C), and the rectangles defined the position of the bifurcations and the dotted line divides the front side and the back side of the vessel (Top map). Contour map of the residual residence time (RRT) that was computed over the simulated cardiac circle, both at the front and back sides of the vessel. Three regions with high RRT were recognised along the stented blood vessel (A,B,C) (Bottom map).

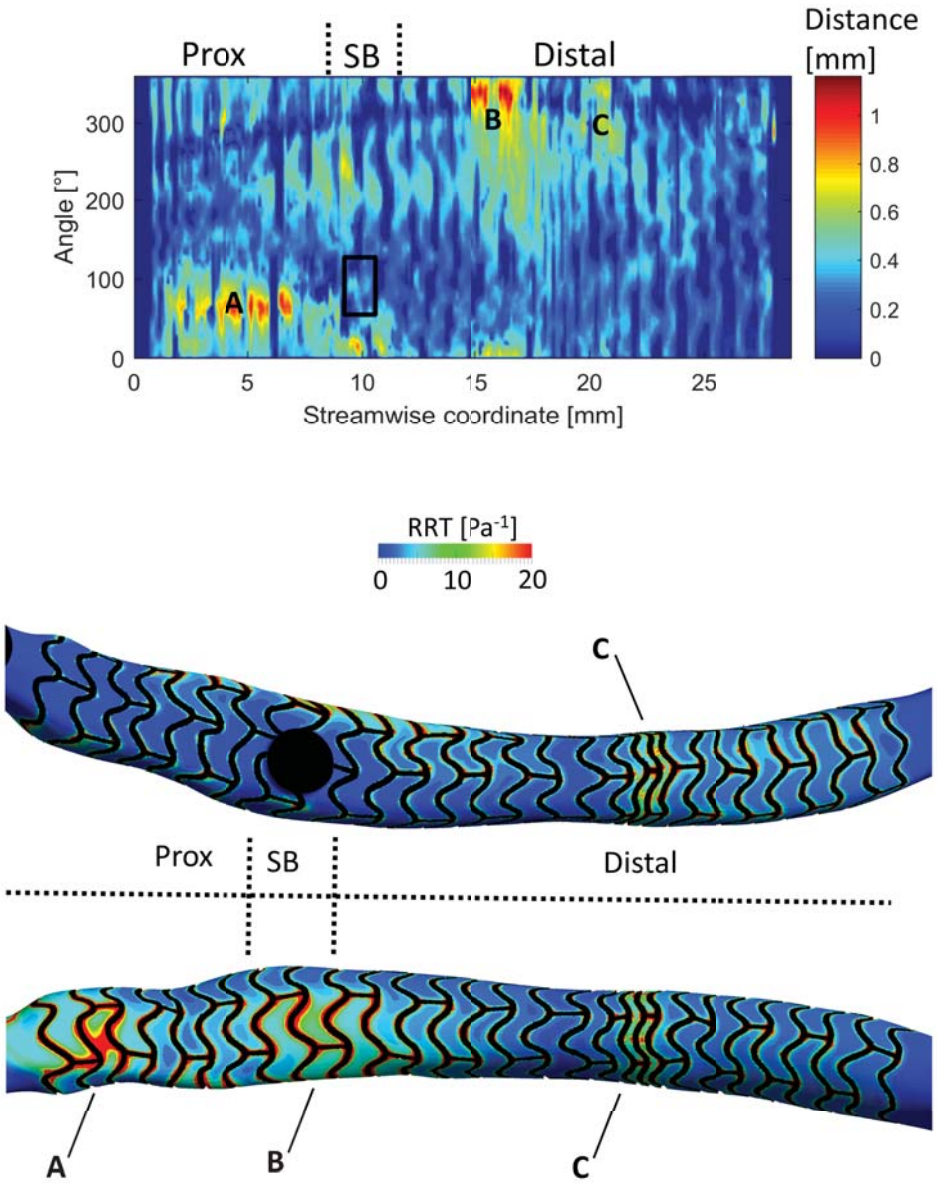

Figure 6.26 Comparison between artery wall remodelling and superficial hemodynamic quantity of Case 13. Distance between 9-months follow-up and baseline lumen contours at the scaffolded segment, regions with high neo-intimal thickening were recognised along the acquisition (A,B,C), and the rectangles defined the position of the bifurcations and the dotted line divides the front side and the back side of the vessel (Top map). Contour map of the residual residence time (RRT) that was computed over the simulated cardiac circle, both at the front and back sides of the vessel. Three regions with high RRT were recognised along the stented blood vessel (A,B,C) (Bottom map).

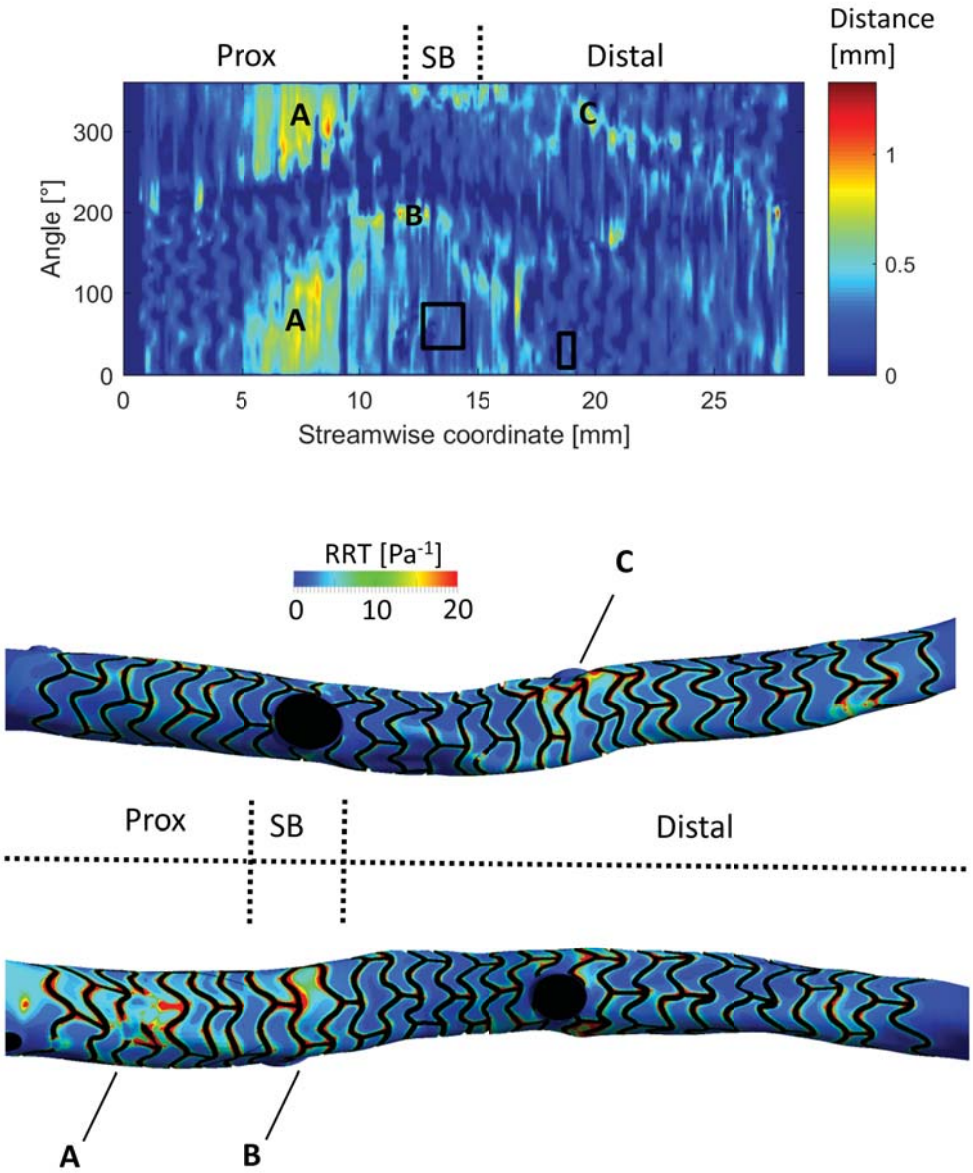

Figure 6.27 Comparison between artery wall remodelling and superficial hemodynamic quantity of Case 14. Distance between 9-months follow-up and baseline lumen contours at the scaffolded segment, regions with high neo-intimal thickening were recognised along the acquisition (A,B,C), and the rectangles defined the position of the bifurcations and the dotted line divides the front side and the back side of the vessel (Top map). Contour map of the residual residence time (RRT) that was computed over the simulated cardiac circle, both at the front and back sides of the vessel. Three regions with high RRT were recognised along the stented blood vessel (A,B,C) (Bottom map).

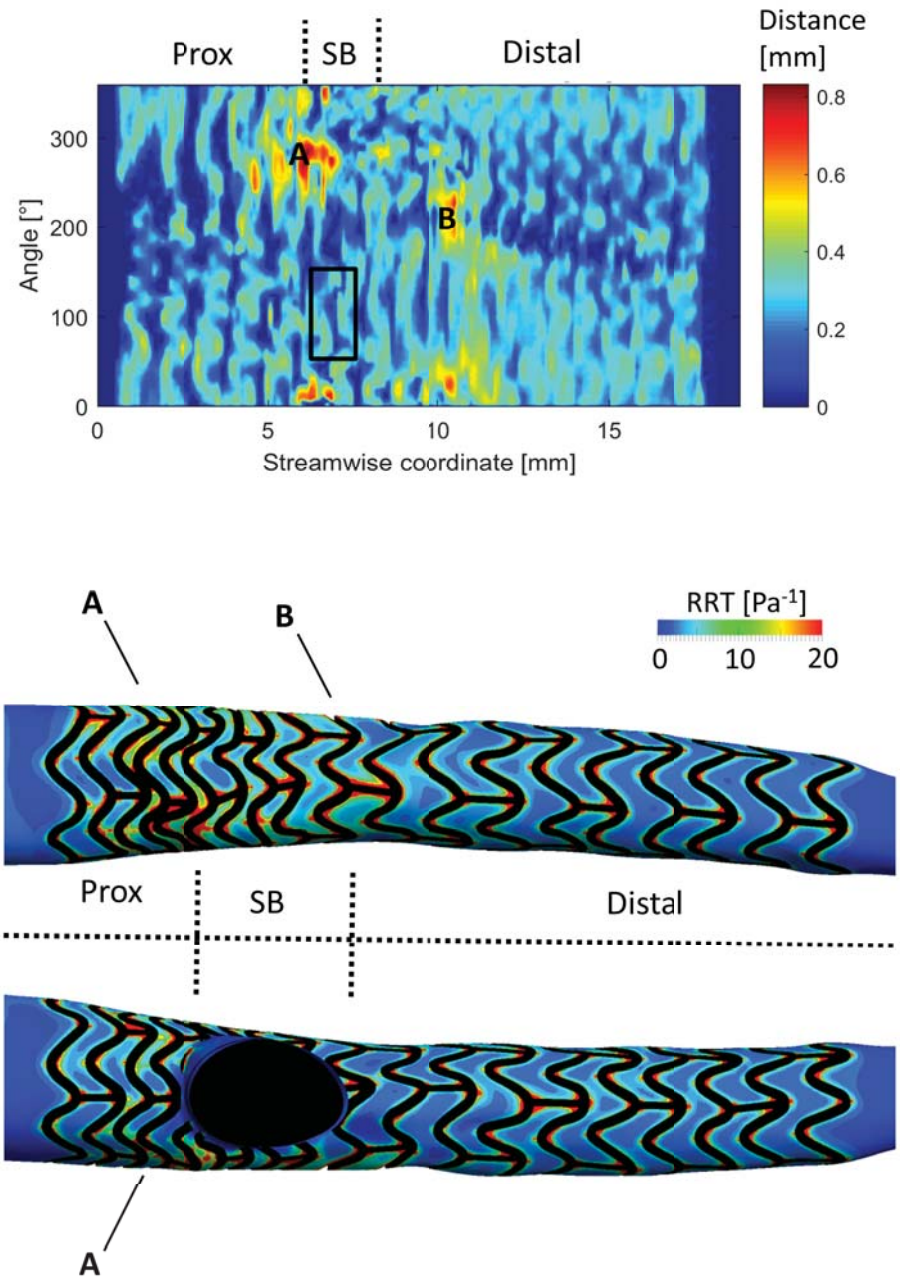

Figure 6.28 Comparison between artery wall remodelling and superficial hemodynamic quantity of Case 15. Distance between 9-months follow-up and baseline lumen contours at the scaffolded segment, regions with high neo-intimal thickening were recognised along the acquisition (A,B), and the rectangles defined the position of the bifurcations and the dotted line divides the front side and the back side of the vessel (Top map). Contour map of the residual residence time (RRT) that was computed over the simulated cardiac circle, both at the front and back sides of the vessel. Two regions with high RRT were recognised along the stented blood vessel (A,B) (Bottom map).

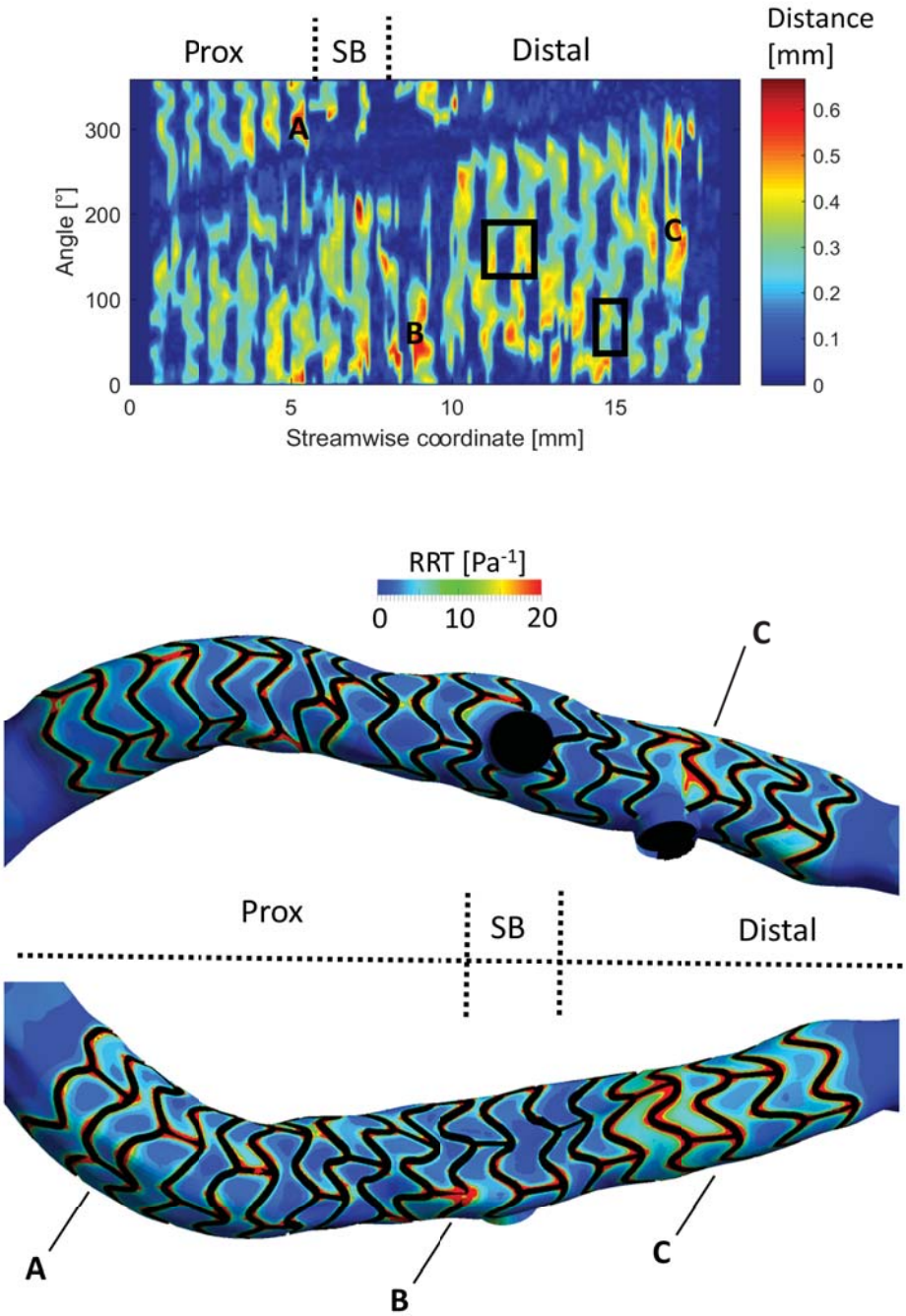

Figure 6.29 Comparison between artery wall remodelling and superficial hemodynamic quantity of Case 16. Distance between 9-months follow-up and baseline lumen contours at the scaffolded segment, regions with high neo-intimal thickening were recognised along the acquisition (A,B,C), and the rectangles defined the position of the bifurcations and the dotted line divides the front side and the back side of the vessel (Top map). Contour map of the residual residence time (RRT) that was computed over the simulated cardiac circle, both at the front and back sides of the vessel. Three regions with high RRT were recognised along the stented blood vessel (A,B,C) (Bottom map).

Chapter 7

Final remarks

THE influence of coronary artery anatomy on PCI outcomes is widely confirmed (Chatzizisis et al., 2014; Lassen et al., 2016). The application of medical imaging techniques, alongside the most advanced computational tools, can indicate possible disturbed hemodynamics that features a specific clinical case. The occurrence of ISR is mainly related to hemodynamics, such as altered distribution of wall shear stress and regions of flow recirculation or stagnation due to stent deployment. This dissertation described a framework for the simulation of patient-specific hemodynamics in stented coronary bifurcations. It comprised a semi-automatic method to reconstruct a stented coronary artery from OCT images in order to carry out CFD analyses. The reconstruction methodology was validated by means of a rigid phantom that resembled a segment of LAD coronary artery with multiple bifurcations. The accuracy of this method was evaluated from the fully-automatic image segmentation algorithm to the semi-automatic 3D geometry reconstruction of the coronary phantom with an implanted stent.

Several works in the literature propose methods that use intravascular imaging techniques to automatically reconstruct the lumen geometry, such as in (Bezerra et al., 2009; Bourantas et al., 2013; Chatzizisis et al., 2014; Ellwein et al., 2011; Nammas et al., 2013; Papafaklis et al., 2015; Slager et al., 2000; Toutouzas et al., 2015; Wentzel et al., 2012; Zaromytidou et al., 2016). However, the literature lacks of exhaustive analyses about coherence with actual lumen and stent geometries. This work as well as the studies by Chiastra et al. (Chiastra et al., 2013a) and OBrien et al. (OBrien et al., 2016) propose a framework for the reconstruction of 3D artery geometries including the implanted stent starting from OCT images for the execution of CFD simulations. Specifically, in this study the stent geometry was preserved through the usage of the implanted device centerline for the morphing procedure, where the position of stent struts was unknown due to light reflection on the OCT guidewire. The proposed methodology is featured by a quantitative validation that proved satisfactory accuracy. Therefore, this dissertation represents an important contribution for the development of a reliable reconstruction tool for the evaluation of altered hemodynamics following stent deployment.

The medical images that were acquired in-vivo after three PCI procedures were elaborated to obtain high fidelity coronary artery reconstructions and to simulate the blood flow. Then, patients' hemodynamics was simulated by taking into account the peculiar blood flow rate, estimated from the angiography acquisitions, and the geometrical features of the specific coronary anatomic dimensions, such as MB cross-section area and outlets diameters. The employed framework enabled to obtain distribution of TAWSS that were strongly patient-specific, as

both patients' coronary anatomies and flow features were resembled. According to the most recent works about the application of polymeric bioresorbable scaffolds, such as the work of Thondapu and co-authors (Thondapu et al., 2018), and the review presented by Chiastra and colleagues (Chiastra et al., 2017a), the work described in this dissertation was the first that included the reconstruction of coronary bifurcations with the implanted scaffold, which actual deployed configuration was included in the model (Migliori et al., 2017).

The developed OCT-based reconstruction methodology was successfully employed to study the effect an plaque ulceration on the local hemodynamics. Results revealed a high degree of flow recirculation both at the ulceration and at the interface with the normal lumen. The lack of clinical practice guidelines makes the treatment of non-occlusive plaques an open question. Therefore, the application of advanced intra-coronary images, high fidelity reconstructions and CFD simulations might guide the management of such pathology. The achieved findings proved the applicability of the developed framework for CFD analyses on complicated patient-specific anatomies, such as ulcerated plaques. A potential application is the prediction of the diffusion of ulceration though intra-mural space, as WSS might provide indexes of local wall failure. For instance, similar analyses were performed in the literature to predict the failure of aneurysms. Steinman and colleagues (Steinman et al., 2003) simulated the blood flow in a intracranial aneurysm reconstructed from computed rotational angiography. The prediction of WSS associated to the anatomy of the disease could assist the assessment of wall growth and rapture, as well as the clinical decision making.

A validated OCT-based reconstruction methodology was employed to analyse the blood flow pattern in 12 patients that underwent PCI and the implantation of an Absorb BVS at a coronary artery bifurcation. The actual configuration of the implanted scaffold was part of the physical domain and patients' hemodynamics was simulated with a commercial CFD software. Then, it was demonstrated: *i)* the possibility of calculating the WSS distribution and blood flow patterns in bifurcation segments treated with an Absorb BVS; *ii)* the potential application of such simulations in the clinical setting by matching the numerical methods with imaging and clinical outcomes in patients. The proposed approach might improve the understanding of the hemodynamic impact of any scaffold design at coronary bifurcations. The additional 9-months follow-up intravascular images enabled the quantification of vessel remodeling after the implantation of a bioresorbable scaffold when treating non-complex bifurcations with a provisional strategy.

Moreover, the dissertation illustrated the use of a patient-specific technique to model blood flow in a stented left main coronary artery bifurcation. The con-

sistency that was found in the literature (Morris et al., 2018) between the computed hemodynamics and the main clinical findings at follow-up confirmed the potentiality of computational simulations as valuable predictors for procedure outcomes. The described approach provided valuable complementary information for support the management of occluded left main coronary artery.

Although results supported the reliability of the presented framework, there were limitations. The developed reconstruction method was validated on a rigid phantom made of a polymeric material. Therefore, the OCT acquisition was not performed in nominal conditions and the images were featured by a higher brightness as compared to in vivo acquisitions. However, the image segmentation outcomes are not influenced because the automatic algorithm is based on grayscale gradients in each OCT frame. Second, the assumption made to sample the MB centerline according to the distance between OCT frames might compromise the accuracy when a vessel with significant tortuosity is reconstructed. Indeed, in those cases the alignment should be performed along the path followed by the OCT catheter during pull-back.

Furthermore, there were limitations related to the periodic deformation of the coronary artery that affected the change of lumen cross-section area during the OCT pull-back. Then, rigid wall conditions, with the coronary artery model fixed in the space domain, were assumed for the CFD simulation. Although it has been shown that the assumption of rigid walls is acceptable in case of stented geometries (Chiastra et al., 2014), it is still unclear whether the coronary motion due to heart contraction can be neglected (Chiastra et al., 2017a). The performed CFD simulation resembled the flow condition at baseline and the scaffold degradation was not modeled. Intuitively, the progressive reduction of scaffold struts cross-section area could influence the local flow conditions. However, it could be argued that flow condition at baseline played an important role in the initiation of scaffold degradation and vessel wall remodeling (Bourantas et al., 2014a). Finally, it was not possible to associate each baseline and follow-up OCT images to compute the neo-intima thickening. Hence, we defined the baseline lumen contour from the follow-up OCT image dataset, as done in a previous study (Bourantas et al., 2014a).

Bibliography

Bezerra, H. G., Costa, M. A., Guagliumi, G., Rollins, A. M., and Simon, D. I. (2009). Intracoronary optical coherence tomography: a comprehensive review: clinical and research applications. *JACC: Cardiovascular Interventions*, 2(11):1035–1046.

Bland, J. M. and Altman, D. G. (2010). Statistical methods for assessing agreement between two methods of clinical measurement. *International Journal of Nursing Studies*, 47(8):931–936.

Blazek, J. (2015). *Computational fluid dynamics: principles and applications*. Butterworth-Heinemann.

Borges, N., Kapadia, S. R., and Ellis, S. G. (2017). Unprotected left main coronary artery disease: Management in the post noble and excel era. *Interventional Cardiology Review*, 12(2):92.

Bourantas, C., Fotiadis, D. I., Kourtis, I., Michalis, L. K., and Plissiti, M. (2003). Three-dimensional coronary artery reconstruction using fusion of intravascular ultrasound and biplane angiography. In *International Congress Series*, volume 1256, pages 1133–1138. Elsevier.

Bourantas, C. V., Kourtis, I. C., Plissiti, M. E., Fotiadis, D. I., Katsouras, C. S., Papafaklis, M. I., and Michalis, L. K. (2005). A method for 3d reconstruction of coronary arteries using biplane angiography and intravascular ultrasound images. *Computerized Medical Imaging and Graphics*, 29(8):597–606.

Bourantas, C. V., Papafaklis, M. I., Athanasiou, L., Kalatzis, F. G., Naka, K. K., Siogkas, P. K., Takahashi, S., Saito, S., Fotiadis, D. I., Feldman, C. L., et al. (2013). A new methodology for accurate 3-dimensional coronary artery reconstruction using routine intravascular ultrasound and angiographic data: implications for widespread assessment of endothelial shear stress in humans. *EuroIntervention*, 9(5):582–93.

Bourantas, C. V., Papafaklis, M. I., Kotsia, A., Farooq, V., Muramatsu, T., Gomez-Lara, J., Zhang, Y.-J., Iqbal, J., Kalatzis, F. G., Naka, K. K., et al. (2014a). Effect of the endothelial shear stress patterns on neointimal proliferation following drug-eluting bioresorbable vascular scaffold implantation: an optical coherence tomography study. *JACC: Cardiovascular Interventions*, 7(3):315–324.

Bourantas, C. V., Papafaklis, M. I., Lakkas, L., Sakellarios, A., Onuma, Y., Zhang, Y.-J., Muramatsu, T., Diletti, R., Bizopoulos, P., Kalatzis, F., et al. (2014b). Fusion of optical coherence tomographic and angiographic data for more accurate evaluation of the endothelial shear stress patterns and neointimal distribution after bioresorbable scaffold implantation: comparison with intravascular ultrasound-derived reconstructions. *The international journal of cardiovascular imaging*, 30(3):485–494.

Brezinski, M. E., Tearney, G. J., Bouma, B. E., Izatt, J. A., Hee, M. R., Swanson, E. A., Southern, J. F., and Fujimoto, J. G. (1996). Optical coherence tomography for optical biopsy: properties and demonstration of vascular pathology. *Circulation*, 93(6):1206–1213.

Brost, A., Strobel, N., Yatziv, L., Gilson, W., Meyer, B., Hornegger, J., Lewin, J., and Wacker, F. (2009). Geometric accuracy of 3-d x-ray image-based localization from two c-arm views. In *Workshop on Geometric Accuracy In Image Guided Interventions-Medical Image Computing and Computer Assisted Interventions 2009*, pages 12–19. Citeseer.

Brown, J. R., Pearlman, D. M., Marshall, E. J., Alam, S. S., MacKenzie, T. A., Recio-Mayoral, A., Gomes, V. O., Kim, B., Jensen, L. O., Mueller, C., et al. (2016). Meta-analysis of individual patient data of sodium bicarbonate and sodium chloride for all-cause mortality after coronary angiography. *The American journal of cardiology*, 118(10):1473–1479.

Byrne, R. A., Stone, G. W., Ormiston, J., and Kastrati, A. (2017). Coronary balloon angioplasty, stents, and scaffolds. *The Lancet*, 390(10096):781–792.

Caputo, M., Chiastra, C., Cianciolo, C., Cutrì, E., Dubini, G., Gunn, J., Keller, B., Migliavacca, F., and Zunino, P. (2013). Simulation of oxygen transfer in stented arteries and correlation with in-stent restenosis. *International journal for numerical methods in biomedical engineering*, 29(12):1373–1387.

Carreau, P. J. (1972). Rheological equations from molecular network theories. *Transactions of the Society of Rheology*, 16(1):99–127.

Celi, S. and Berti, S. (2014). In-vivo segmentation and quantification of coronary lesions by optical coherence tomography images for a lesion type definition and stenosis grading. *Medical image analysis*, 18(7):1157–1168.

Chatzizisis, Y. S., Koutkias, V. G., Toutouzas, K., Giannopoulos, A., Chouvarda, I., Riga, M., Antoniadis, A. P., Cheimariotis, G., Doulaverakis, C., Tsampoulatidis, I., et al. (2014). Clinical validation of an algorithm for rapid and accurate automated segmentation of intracoronary optical coherence tomography images. *International journal of cardiology*, 172(3):568–580.

Cheng, C., Helderman, F., Tempel, D., Segers, D., Hierck, B., Poelmann, R., van Tol, A., Duncker, D. J., Robbers-Visser, D., Ursem, N. T., et al. (2007). Large variations in absolute wall shear stress levels within one species and between species. *Atherosclerosis*, 195(2):225–235.

Chiastra, C., Migliavacca, F., Martínez, M. Á., and Malve, M. (2014). On the necessity of modelling fluid–structure interaction for stented coronary arteries. *Journal of the mechanical behavior of biomedical materials*, 34:217–230.

Chiastra, C., Migliori, S., Burzotta, F., Dubini, G., and Migliavacca, F. (2017a). Patient-specific modeling of stented coronary arteries reconstructed from optical coherence tomography: Towards a widespread clinical use of fluid dynamics analyses. *Journal of cardiovascular translational research*, pages 1–17.

Chiastra, C., Montin, E., Bologna, M., Migliori, S., Aurigemma, C., Burzotta, F., Celi, S., Dubini, G., Migliavacca, F., and Mainardi, L. (2017b). Reconstruction of stented coronary arteries from optical coherence tomography images: Feasibility, validation, and repeatability of a segmentation method. *PloS one*, 12(6):e0177495.

Chiastra, C., Montin, E., Burzotta, F., Mainardi, L., and Migliavacca, F. (2013a). Coronary stenting: From optical coherence tomography to fluid dynamic simulations. In *Bioinformatics and Bioengineering (BIBE), 2013 IEEE 13th International Conference on*, pages 1–4. IEEE.

Chiastra, C., Morlacchi, S., Gallo, D., Morbiducci, U., Cárdenes, R., Larrabide, I., and Migliavacca, F. (2013b). Computational fluid dynamic simulations of image-based stented coronary bifurcation models. *Journal of The Royal Society Interface*, 10(84):20130193.

Chiastra, C., Wu, W., Dickerhoff, B., Aleiou, A., Dubini, G., Otake, H., Migliavacca, F., and LaDisa, J. F. (2016). Computational replication of the patient-specific stenting procedure for coronary artery bifurcations: From oct and ct imaging to structural and hemodynamics analyses. *Journal of biomechanics*, 49(11):2102–2111.

Çimen, S., Gooya, A., Grass, M., and Frangi, A. F. (2016). Reconstruction of coronary arteries from x-ray angiography: A review. *Medical image analysis*, 32:46–68.

Cohen, D. J., Osnabrugge, R. L., Magnuson, E. A., Wang, K., Li, H., Chinnakondepalli, K., Pinto, D., Abdallah, M. S., Vilain, K. A., Morice, M.-C., et al. (2014). Cost-effectiveness of percutaneous coronary intervention with drug-eluting stents vs. bypass surgery for patients with 3-vessel or left main coronary artery disease: final results from the syntax trial. *Circulation*, pages CIRCULATIONAHA–114.

Davies, J. E., Whinnett, Z. I., Francis, D. P., Manisty, C. H., Aguado-Sierra, J., Willson, K., Foale, R. A., Malik, I. S., Hughes, A. D., Parker, K. H., et al. (2006). Evidence of a dominant backward-propagating suction wave responsible for diastolic coronary filling in humans, attenuated in left ventricular hypertrophy. *Circulation*, 113(14):1768–1778.

DeMaio Jr, S. J., Kinsella, S. H., and Silverman, M. E. (1989). Clinical course and long-term prognosis of spontaneous coronary artery dissection. *The American journal of cardiology*, 64(8):471–474.

Dodge, J. T., Brown, B. G., Bolson, E. L., and Dodge, H. T. (1992). Lumen diameter of normal human coronary arteries. influence of age, sex, anatomic variation, and left ventricular hypertrophy or dilation. *Circulation*, 86(1):232–246.

Doran, B. P., Judnitch, R. T., and Kveen, G. L. (2000). Helical stent design. US Patent 6,042,597.

Doriot, P.-A., Dorsaz, P.-A., Dorsaz, L., De Benedetti, E., Chatelain, P., and Delafontaine, P. (2000). In-vivo measurements of wall shear stress in human coronary arteries. *Coronary artery disease*, 11(6):495–502.

Drake, R., Vogl, A. W., and Mitchell, A. W. (2012). *Gray's Basic Anatomy E-Book: with STUDENT CONSULT Online Access*. Elsevier Health Sciences.

Dvir, D., Assali, A., and Kornowski, R. (2008). Percutaneous coronary intervention for chronic total occlusion: Novel 3-dimensional imaging and quantitative analysis. *Catheterization and Cardiovascular Interventions*, 71(6):784–789.

Ellwein, L. M., Otake, H., Gundert, T. J., Koo, B.-K., Shinke, T., Honda, Y., Shite, J., and LaDisa, J. F. (2011). Optical coherence tomography for patient-specific 3d artery reconstruction and evaluation of wall shear stress in a left circumflex coronary artery. *Cardiovascular Engineering and Technology*, 2(3):212.

Fedele, R., Ciani, A., and Fiori, F. (2014). X-ray microtomography under loading and 3d-volume digital image correlation. a review. *Fundamenta Informaticae*, 135(1-2):171–197.

Fedele, R., Ciani, A., Galantucci, L., Bettuzzi, M., and Andena, L. (2013a). A regularized, pyramidal multi-grid approach to global 3d-volume digital image correlation based on x-ray micro-tomography. *Fundamenta Informaticae*, 125(3-4):361–376.

Fedele, R., Galantucci, L., and Ciani, A. (2013b). Global 2d digital image correlation for motion estimation in a finite element framework: a variational formulation and a regularized, pyramidal, multi-grid implementation. *International Journal for Numerical Methods in Engineering*, 96(12):739–762.

Feher, J. J. (2017). *Quantitative human physiology: an introduction*. Academic press.

Finet, G., Gilard, M., Perrenot, B., Rioufol, G., Motreff, P., Gavit, L., and Prost, R. (2008). Fractal geometry of arterial coronary bifurcations: a quantitative coronary angiography and intravascular ultrasound analysis. *EuroIntervention: journal of EuroPCR in collaboration with the Working Group on Interventional Cardiology of the European Society of Cardiology*, 3(4):490–498.

Food, P. H. S. and Administration, D. (2016). *FDA Executive Summary*.

Gamage, P. P., Khalili, F., and Mansy, H. A. (2018). Numerical modeling of pulse wave propagation in a stenosed artery using two-way coupled fluid structure interaction (fsi). *arXiv preprint arXiv:1803.03554*.

Garcia, J. A., Movassaghi, B., Casserly, I. P., Klein, A. J., Chen, S.-Y. J., Messenger, J. C., Hansgen, A., Wink, O., Groves, B. M., and Carroll, J. D. (2009). Determination of optimal viewing regions for x-ray coronary angiography

based on a quantitative analysis of 3d reconstructed models. *The international journal of cardiovascular imaging*, 25(5):455–462.

Giacoppo, D., Capodanno, D., Dangas, G., and Tamburino, C. (2014). Spontaneous coronary artery dissection. *International journal of cardiology*, 175(1):8–20.

Giannopoulos, A. A., Antoniadis, A. P., Croce, K. J., and Chatzizisis, Y. S. (2015). Advanced anatomical and functional imaging guides management of coronary artery ulcerated plaque. *European Heart Journal-Cardiovascular Imaging*, 16(9):1042–1042.

Giavarina, D. (2015). Understanding bland altman analysis. *Biochemia medica: Biochemia medica*, 25(2):141–151.

Gogas, B. D., Garcia-Garcia, H. M., Onuma, Y., Muramatsu, T., Farooq, V., Bourantas, C. V., and Serruys, P. W. (2013). Edge vascular response after percutaneous coronary intervention: an intracoronary ultrasound and optical coherence tomography appraisal: from radioactive platforms to first-and second-generation drug-eluting stents and bioresorbable scaffolds. *JACC: Cardiovascular Interventions*, 6(3):211–221.

Gonzalez, R. C., Woods, R. E., and Eddins, S. L. (2009). *Digital Image Processing Using MATLAB®*. Gatesmark Publishing.

Hadjiloizou, N., Davies, J. E., Malik, I. S., Aguado-Sierra, J., Willson, K., Foale, R. A., Parker, K. H., Hughes, A. D., Francis, D. P., and Mayet, J. (2008). Differences in cardiac microcirculatory wave patterns between the proximal left mainstem and proximal right coronary artery. *American Journal of Physiology-Heart and Circulatory Physiology*, 295(3):H1198–H1205.

Hall, J. E. (2015). *Guyton and Hall Textbook of Medical Physiology E-Book*. Elsevier Health Sciences.

Himburg, H. A., Grzybowski, D. M., Hazel, A. L., LaMack, J. A., Li, X.-M., and Friedman, M. H. (2004). Spatial comparison between wall shear stress measures and porcine arterial endothelial permeability. *American Journal of Physiology-Heart and Circulatory Physiology*, 286(5):H1916–H1922.

Huo, Y., Choy, J. S., Svendsen, M., Sinha, A. K., and Kassab, G. S. (2009). Effects of vessel compliance on flow pattern in porcine epicardial right coronary arterial tree. *Journal of biomechanics*, 42(5):594–602.

Isayama, H., Nakai, Y., Toyokawa, Y., Togawa, O., Gon, C., Ito, Y., Yashima, Y., Yagioka, H., Kogure, H., Sasaki, T., et al. (2009). Measurement of radial and axial forces of biliary self-expandable metallic stents. *Gastrointestinal endoscopy*, 70(1):37–44.

Jang, I.-K., Bouma, B. E., Kang, D.-H., Park, S.-J., Park, S.-W., Seung, K.-B., Choi, K.-B., Shishkov, M., Schlendorf, K., Pomerantsev, E., et al. (2002). Visualization of coronary atherosclerotic plaques in patients using optical coherence tomography: comparison with intravascular ultrasound. *Journal of the American College of Cardiology*, 39(4):604–609.

Jang, I.-K., Tearney, G., and Bouma, B. (2001). Visualization of tissue prolapse between coronary stent struts by optical coherence tomography: comparison with intravascular ultrasound. *Circulation*, 104(22):2754–2754.

Kafi, O., El Khatib, N., Tiago, J., and Sequeira, A. (2017). Numerical simulations of a 3d fluid-structure interaction model for blood flow in an atherosclerotic artery. *Mathematical Biosciences & Engineering*, 14(1):179–193.

Karanasos, A., Schuurbiers, J. C., Garcia-Garcia, H. M., Simsek, C., Onuma, Y., Serruys, P. W., Zijlstra, F., van Geuns, R.-J., Regar, E., and Wentzel, J. J. (2015). Association of wall shear stress with long-term vascular healing response following bioresorbable vascular scaffold implantation. *International journal of cardiology*, 191:279–283.

Kessler, W., Moshage, W., Galland, A., Zink, D., Achenbach, S., Nitz, W., Laub, G., and Bachmann, K. (1998). Assessment of coronary blood flow in humans using phase difference mr imaging. comparison with intracoronary doppler flow measurement. *International journal of cardiac imaging*, 14(3):179–86.

Kim, M. S. and Dean, L. S. (2011). In-stent restenosis. *Cardiovascular therapeutics*, 29(3):190–198.

Ku, D. N., Giddens, D. P., Zarins, C. K., and Glagov, S. (1985). Pulsatile flow and atherosclerosis in the human carotid bifurcation. positive correlation between plaque location and low oscillating shear stress. *Arteriosclerosis, thrombosis, and vascular biology*, 5(3):293–302.

Lassen, J. F., Holm, N. R., Banning, A., Burzotta, F., Lefèvre, T., Chieffo, A., Hildick-Smith, D., Louvard, Y., and Stankovic, G. (2016). Percutaneous coronary intervention for coronary bifurcation disease: 11th consensus document from the european bifurcation club. *EuroIntervention*, 12(1):38–46.

Louvard, Y., Medina, A., and Stankovic, G. (2010). Definition and classification of bifurcation lesions and treatments. *EuroIntervention: journal of EuroPCR in collaboration with the Working Group on Interventional Cardiology of the European Society of Cardiology*, 6:J31.

Macedo, M. M. G. d., Takimura, C. K., Lemos, P. A., and Gutierrez, M. A. (2016). A robust fully automatic lumen segmentation method for in vivo intracoronary optical coherence tomography. *Research on Biomedical Engineering*, 32(1):35–43.

Madhavan, M. V., Tarigopula, M., Mintz, G. S., Maehara, A., Stone, G. W., and Généreux, P. (2014). Coronary artery calcification: pathogenesis and prognostic implications. *Journal of the American College of Cardiology*, 63(17):1703–1714.

Magnuson, E. A., Farkouh, M. E., Fuster, V., Wang, K., Vilain, K., Li, H., Appelwick, J., Muratov, V., Sleeper, L. A., Boineau, R., et al. (2012). Cost-effectiveness of percutaneous coronary intervention with drug eluting stents versus bypass surgery for patients with diabetes and multivessel coronary artery disease: results from the freedom trial. *Circulation*, pages CIRCULATIONAHA–112.

Malek, A. M., Alper, S. L., and Izumo, S. (1999). Hemodynamic shear stress and its role in atherosclerosis. *Jama*, 282(21):2035–2042.

Malek, A. M. and Izumo, S. (1996). Mechanism of endothelial cell shape change and cytoskeletal remodeling in response to fluid shear stress. *Journal of cell science*, 109(4):713–726.

Mann, J. and Truswell, S. (2017). *Essentials of human nutrition*. Oxford University Press.

McCance, K. L. and Huether, S. E. (2015). *Pathophysiology-E-Book: The Biologic Basis for Disease in Adults and Children*. Elsevier Health Sciences.

Medina, A., de Lezo, J. S., and Pan, M. (2006). A new classification of coronary bifurcation lesions. *Revista espanola de cardiologia*, 59(02):183–183.

Migliori, S., Chiastra, C., Bologna, M., Montin, E., Dubini, G., Aurigemma, C., Fedele, R., Burzotta, F., Mainardi, L., and Migliavacca, F. (2017). A framework for computational fluid dynamic analyses of patient-specific stented coronary arteries from optical coherence tomography images. *Medical Engineering & Physics*, 47:105–116.

Migliori, S., Rampat, R., Bologna, M., Montin, E., Burzotta, F., Hildick-Smith, D., Dubini, G., Mainardi, L., Migliavacca, F., Cockburn, J., et al. (2018). A patient-specific study investigating the relation between coronary hemodynamics and neo-intimal thickening after bifurcation stenting with a polymeric bioresorbable scaffold. *Applied Sciences*, 8(9):1510.

Mintz, G. S. (2015). Intravascular imaging of coronary calcification and its clinical implications. *JACC: Cardiovascular Imaging*, 8(4):461–471.

Montin, E., Migliori, S., Chiastra, C., Credi, C., Fedele, R., Aurigemma, C., Levi, M., Burzotta, F., Migliavacca, F., and Mainardi, L. T. (2016). A method for coronary bifurcation centerline reconstruction from angiographic images based on focalization optimization. In *Engineering in Medicine and Biology Society (EMBC), 2016 IEEE 38th Annual International Conference of the*, pages 4165–4168. IEEE.

Morice, M., Serruys, P., Kappetein, A., et al. (2010). Outcomes in patients with de novo left main disease treated with in the synergy between percutaneous coronary intervention with taxus and cardiac surgery (syntax) trial. *Circulation*, 121:2645–53.

Morlacchi, S., Chiastra, C., Cutrì, E., Zunino, P., Burzotta, F., Formaggia, L., Dubini, G., and Migliavacca, F. (2014). Stent deformation, physical stress, and drug elution obtained with provisional stenting, conventional culotte and tryton-based culotte to treat bifurcations: a virtual simulation study. *EuroIntervention: journal of EuroPCR in collaboration with the Working Group on Interventional Cardiology of the European Society of Cardiology*, 9(12):1441–1453.

Morris, P. D., Iqbal, J., Chiastra, C., Wu, W., Migliavacca, F., and Gunn, J. P. (2018). Simultaneous kissing stents to treat unprotected left main stem coronary artery bifurcation disease; stent expansion, vessel injury, hemodynamics, tissue healing, restenosis, and repeat revascularization. *Catheterization and Cardiovascular Interventions*.

Mortensen, K. H., Thuesen, L., Kristensen, I., and Christiansen, E. H. (2009). Spontaneous coronary artery dissection: a western denmark heart registry study. *Catheterization and Cardiovascular Interventions*, 74(5):710–717.

Mozaffarian, D., Benjamin, E. J., Go, A. S., Arnett, D. K., Blaha, M. J., Cushman, M., Das, S. R., de Ferranti, S., Després, J.-P., Fullerton, H. J., et al. (2016). Heart disease and stroke statistics2016 update: a report from the american heart association. *Circulation*, 133(4):e38–e360.

Murray, C. D. (1926). The physiological principle of minimum work: I. the vascular system and the cost of blood volume. *Proceedings of the National Academy of Sciences*, 12(3):207–214.

Nammas, W., Ligthart, J. M., Karanasos, A., Witberg, K. T., and Regar, E. (2013). Optical coherence tomography for evaluation of coronary stents in vivo. *Expert review of cardiovascular therapy*, 11(5):577–588.

Nieman, K., Oudkerk, M., Rensing, B. J., van Ooijen, P., Munne, A., van Geuns, R.-J., and de Feyter, P. J. (2001). Coronary angiography with multi-slice computed tomography. *The Lancet*, 357(9256):599–603.

OBrien, C. C., Kolandaivelu, K., Brown, J., Lopes, A. C., Kunio, M., Kolachalama, V. B., and Edelman, E. R. (2016). Constraining oct with knowledge of device design enables high accuracy hemodynamic assessment of endovascular implants. *PloS one*, 11(2):e0149178.

Papafaklis, M. I., Bourantas, C. V., Yonetsu, T., Vergallo, R., Kotsia, A., Nakatani, S., Lakkas, L. S., Athanasiou, L. S., Naka, K. K., Fotiadis, D. I., et al. (2015). Anatomically correct three-dimensional coronary artery reconstruction using frequency domain optical coherence tomographic and angiographic data: head-to-head comparison with intravascular ultrasound for endothelial shear stress assessment in humans. *EuroIntervention*, 11(4):407–415.

Prati, F., Jenkins, M., Di Giorgio, A., and Rollins, A. (2011). Intracoronary optical coherence tomography, basic theory and image acquisition techniques. *The international journal of cardiovascular imaging*, 27(2):251–258.

Puddu, P. E. and Menotti, A. (2016). Coronary heart disease differences in eastern versus western europe: a demanding situation. *International journal of cardiology*, 217:S60–S63.

Rampat, R., Mayo, T., Hildick-Smith, D., and Cockburn, J. (2018). A randomised trial comparing two stent sizing strategies in coronary bifurcation treatment with bioresorbable vascular scaffolds–the absorb bifurcation coronary (abc) trial. *Cardiovascular Revascularization Medicine*.

Regar, E., Ligthart, J., Bruining, N., and van Soest, G. (2011). The diagnostic value of intracoronary optical coherence tomography. *Herz*, 36(5):417.

Rieu, R., Barragan, P., Masson, C., Fuseri, J., Garitey, V., Silvestri, M., Roquebert, P., and Sainsous, J. (1999). Radial force of coronary stents: a comparative analysis. *Catheterization and Cardiovascular Interventions*, (46):380–91.

Sakamoto, S., Takahashi, S., Coskun, A. U., Papafaklis, M. I., Takahashi, A., Saito, S., Stone, P. H., and Feldman, C. L. (2013). Relation of distribution of coronary blood flow volume to coronary artery dominance. *American Journal of cardiology*, 111(10):1420–1424.

Sankaran, S., Kim, H. J., Choi, G., and Taylor, C. A. (2016). Uncertainty quantification in coronary blood flow simulations: impact of geometry, boundary conditions and blood viscosity. *Journal of biomechanics*, 49(12):2540–2547.

Serruys, P. W., Chevalier, B., Sotomi, Y., Cequier, A., Carrié, D., Piek, J. J., Van Boven, A. J., Dominici, M., Dudek, D., McClean, D., et al. (2016). Comparison of an everolimus-eluting bioresorbable scaffold with an everolimus-eluting metallic stent for the treatment of coronary artery stenosis (absorb ii): a 3 year, randomised, controlled, single-blind, multicentre clinical trial. *The Lancet*, 388(10059):2479–2491.

Serruys, P. W., Suwannasom, P., Nakatani, S., and Onuma, Y. (2015). Snowshoe versus ice skate for scaffolding of disrupted vessel wall.

Sharma, S. K., Choudhury, A., Lee, J., Kim, M. C., Fisher, E., Steinheimer, A. M., and Kini, A. S. (2004). Simultaneous kissing stents (sks) technique for treating bifurcation lesions in medium-to-large size coronary arteries. *The American journal of cardiology*, 94(7):913–917.

Sheiban, I., Sillano, D., Biondi-Zoccai, G., Chieffo, A., Colombo, A., Vecchio, S., Margheri, M., Gunn, J. P., Raina, T., Liistro, F., et al. (2009). Incidence and management of restenosis after treatment of unprotected left main disease with drug-eluting stents: 70 restenotic cases from a cohort of 718 patients: Fails (failure in left main study). *Journal of the American College of Cardiology*, 54(13):1131–1136.

Shibeshi, S. S. and Collins, W. E. (2005). The rheology of blood flow in a branched arterial system. *Applied rheology (Lappersdorf, Germany: Online)*, 15(6):398.

Sigwart, U., Puel, J., Mirkovitch, V., Joffre, F., and Kappenberger, L. (1987). Intravascular stents to prevent occlusion and re-stenosis after transluminal angioplasty. *New England Journal of Medicine*, 316(12):701–706.

Slager, C. J., Wentzel, J. J., Schuurbiers, J. C., Oomen, J. A., Kloet, J., Krams, R., Von Birgelen, C., Van Der Giessen, W. J., Serruys, P. W., and De Feyter, P. J. (2000). True 3-dimensional reconstruction of coronary arteries in patients by fusion of angiography and ivus (angus) and its quantitative validation. *Circulation*, 102(5):511–516.

Sotomi, Y., Onuma, Y., Collet, C., Tenekecioglu, E., Virmani, R., Kleiman, N. S., and Serruys, P. W. (2017). Bioresorbable scaffold: the emerging reality and future directions. *Circulation research*, 120(8):1341–1352.

Steinman, D. A., Milner, J. S., Norley, C. J., Lownie, S. P., and Holdsworth, D. W. (2003). Image-based computational simulation of flow dynamics in a giant intracranial aneurysm. *American Journal of Neuroradiology*, 24(4):559–566.

Stoeckel, D., Bonsignore, C., and Duda, S. (2002). A survey of stent designs. *Minimally Invasive Therapy & Allied Technologies*, 11(4):137–147.

Stone, G. W., Sabik, J. F., Serruys, P. W., Simonton, C. A., Généreux, P., Puskas, J., Kandzari, D. E., Morice, M.-C., Lembo, N., Brown III, W. M., et al. (2016). Everolimus-eluting stents or bypass surgery for left main coronary artery disease. *New England Journal of Medicine*, 375(23):2223–2235.

Stone, G. W. and St. Goar, F. G. (1996). Spontaneous coronary dissection resulting in acute myocardial infarction: successful treatment with primary angioplasty. *Catheterization and cardiovascular diagnosis*, 38(1):62–66.

Tabas, I. (2010). Macrophage death and defective inflammation resolution in atherosclerosis. *Nature Reviews Immunology*, 10(1):36.

Tearney, G. J., Brezinski, M. E., Bouma, B. E., Boppart, S. A., Pitris, C., Southern, J. F., and Fujimoto, J. G. (1997). In vivo endoscopic optical biopsy with optical coherence tomography. *Science*, 276(5321):2037–2039.

Tearney, G. J., Regar, E., Akasaka, T., Adriaenssens, T., Barlis, P., Bezerra, H. G., Bouma, B., Bruining, N., Cho, J.-m., Chowdhary, S., et al. (2012). Consensus standards for acquisition, measurement, and reporting of intravascular optical coherence tomography studies: a report from the international working group for intravascular optical coherence tomography standardization and validation. *Journal of the American College of Cardiology*, 59(12):1058–1072.

Tenekecioglu, E., Albuquerque, F. N., Sotomi, Y., Zeng, Y., Suwannasom, P., Tateishi, H., Cavalcante, R., Ishibashi, Y., Nakatani, S., Abdelghani, M., et al. (2017a). Intracoronary optical coherence tomography: Clinical and research applications and intravascular imaging software overview. *Catheterization and Cardiovascular Interventions*, 89(4):679–689.

Tenekecioglu, E., Torii, R., Bourantas, C., Abdelghani, M., Cavalcante, R., Sotomi, Y., Crake, T., Su, S., Santoso, T., Onuma, Y., et al. (2017b). Assessment of the hemodynamic characteristics of absorb bvs in a porcine coronary artery model. *International journal of cardiology*, 227:467–473.

Thondapu, V., Tenekecioglu, E., Poon, E. K., Collet, C., Torii, R., Bourantas, C. V., Chin, C., Sotomi, Y., Jonker, H., Dijkstra, J., et al. (2018). Endothelial shear stress 5 years after implantation of a coronary bioresorbable scaffold. *European heart journal*, 39(18):1602–1609.

Torii, R., Oshima, M., Kobayashi, T., Takagi, K., and Tezduyar, T. E. (2009). Fluid–structure interaction modeling of blood flow and cerebral aneurysm: significance of artery and aneurysm shapes. *Computer Methods in Applied Mechanics and Engineering*, 198(45-46):3613–3621.

Torii, R., Tenekecioglu, E., Bourantas, C., Poon, E., Thondapu, V., Gijsen, F., Sotomi, Y., Onuma, Y., Barlis, P., Ooi, A. S., et al. (2017). Five-year follow-up of underexpanded and overexpanded bioresorbable scaffolds: self-correction and impact on shear stress. *EuroIntervention*, 12(17):2158–2159.

Toutouzas, K., Chatzizisis, Y. S., Riga, M., Giannopoulos, A., Antoniadis, A. P., Tu, S., Fujino, Y., Mitsouras, D., Doulaverakis, C., Tsampoulatidis, I., et al. (2015). Accurate and reproducible reconstruction of coronary arteries and endothelial shear stress calculation using 3d oct: comparative study to 3d ivus and 3d qca. *Atherosclerosis*, 240(2):510–519.

Ughi, G. J., Adriaenssens, T., Onsea, K., Kayaert, P., Dubois, C., Sinnaeve, P., Coosemans, M., Desmet, W., and Dhooge, J. (2012). Automatic segmentation of in-vivo intra-coronary optical coherence tomography images to assess stent strut apposition and coverage. *The international journal of cardiovascular imaging*, 28(2):229–241.

Van der Giessen, A. G., Groen, H. C., Doriot, P.-A., De Feyter, P. J., Van der Steen, A. F., Van de Vosse, F. N., Wentzel, J. J., and Gijsen, F. J. (2011). The influence of boundary conditions on wall shear stress distribution in patients specific coronary trees. *Journal of biomechanics*, 44(6):1089–1095.

Van der Heiden, K., Gijsen, F. J., Narracott, A., Hsiao, S., Halliday, I., Gunn, J., Wentzel, J. J., and Evans, P. C. (2013). The effects of stenting on shear stress: relevance to endothelial injury and repair. *Cardiovascular research*, 99(2):269–275.

Wahle, A., Prause, G. P., DeJong, S. C., and Sonka, M. (1999). Geometrically correct 3-d reconstruction of intravascular ultrasound images by fusion with biplane angiography-methods and validation. *IEEE transactions on medical imaging*, 18(8):686–699.

Wang, A., Eggermont, J., Dekker, N., Garcia-Garcia, H. M., Pawar, R., Reiber, J. H., and Dijkstra, J. (2013). Automatic stent strut detection in intravascular optical coherence tomographic pullback runs. *The international journal of cardiovascular imaging*, 29(1):29–38.

Wang, A., Nakatani, S., Eggermont, J., Onuma, Y., Garcia-Garcia, H. M., Serruys, P. W., Reiber, J. H., and Dijkstra, J. (2014). Automatic detection of bioresorbable vascular scaffold struts in intravascular optical coherence tomography pullback runs. *Biomedical optics express*, 5(10):3589–3602.

Wentzel, J. J., Chatzizisis, Y. S., Gijsen, F. J., Giannoglou, G. D., Feldman, C. L., and Stone, P. H. (2012). Endothelial shear stress in the evolution of coronary atherosclerotic plaque and vascular remodelling: current understanding and remaining questions. *Cardiovascular research*, 96(2):234–243.

White, C. R. and Frangos, J. A. (2007). The shear stress of it all: the cell membrane and mechanochemical transduction. *Philosophical Transactions of the Royal Society of London B: Biological Sciences*, 362(1484):1459–1467.

Zaromytidou, M., Siasos, G., Coskun, A. U., Lucier, M., Antoniadis, A. P., Papafaklis, M. I., Koskinas, K. C., Andreou, I., Feldman, C. L., and Stone, P. H. (2016). Intravascular hemodynamics and coronary artery disease: new insights and clinical implications. *Hellenic Journal of Cardiology*, 57(6):389–400.

Publications

Papers

Migliori S., Rampat R., Bologna M., Montin E., Burzotta F., Hildick-Smith D., Dubini G., Mainardi L., Migliavacca F., Cockburn J., Chiastra C. A patient-specific study investigating the relation between coronary hemodynamics and neo-intimal thickening after bifurcation stenting with a polymeric bioresorbable scaffold. *Open Access Journal Applied Sciences*.

Chiastra C., **Migliori S.**, Burzotta F., Dubini G., Migliavacca F. Fluid dynamic performances of a new polymeric heart valve prototype (poli-valve) tested under continuous and pulsatile flow conditions. *Journal of Cardiovascular Translational Research*, 2018, 11.2: 156-172. https://doi.org/10.1007/s12265-017-9777-6.

Chiastra C., Montin E., Bologna M., **Migliori S.**, Aurigemma C., Burzotta F., Celi S., Dubini G., Migliavacca F., Mainardi L. Reconstruction of stented coronary arteries from optical coherence tomography images: Feasibility, validation, and repeatability of a segmentation method. *PLoS One*, 2017;12:e0177495. doi:10.1371/journal.pone.0177495.

Migliori S., Chiastra C., Bologna M., Montin E., Dubini G., Aurigemma C., Fedele R., Burzotta F., Mainardi L., Migliavacca F. A framework for computational fluid dynamic analyses of patient-specific stented coronary arteries from optical coherence tomography images. *Journal of Medical Engineering and Physics*, 10:400. doi:10.1016/j.medengphy.2017.06.027.

Proceedings

Bologna M., **Migliori S.**, Montin E., Rampat R., Hildick-Smith D., Cockburn J., Migliavacca F., Mainardi L., Chiastra C. An OCT-based reconstruction methodology to investigate the link between wall shear stress and neointimal coverage in patient-specific stented coronary bifurcations. *Proceedings of the 6th Italian National Congress of Bioengineering, GNB2018*, 25th-27th June 2018.

Migliori S., Chiastra C., Bologna M., Montin E., De Francesco S., Dubini G., Burzotta F., Rampar R., Cockburn J., Hildick-Smith D., Mainardi L., Migliavacca F. An OCT-based reconstruction methodology to investigate the link between wall shear stress and neointimal coverage in patient-specific stented coronary bifurcations. *Proceedings of the World Congress of Biomechanics, WCB2018*, 8th-12th July 2018.

Migliori S., Chiastra C., Bologna M., Montin E., De Francesco S., Dubini G., Burzotta F., Rampar R., Cockburn J., Hildick-Smith D., Mainardi L., Migliavacca F. A computational investigation on the influence of wall shear stress after stent deployment. *Proceedings of the Young Researchers Conference Frontiers of Simulation and Experimentation for Personalised Cardiovascular Management and Treatment, 2018*, 19th-20th July 2018.

Migliori S., Chiastra C., Bologna M., Montin E., De Francesco S., Dubini G., Burzotta F., Rampar R., Cockburn J., Hildick-Smith D., Mainardi L., Migliavacca F. A computational investigation of the link between wall shear stress after stent deployment in coronary arteries and neo-intimal coverage. *Proceedings of the Virtual Physiological Human Conference, VPH2018*, 5th-7th September 2018.

Migliori S., Chiastra C., Bologna M., Montin E., Dubini G., Aurigemma C., Burzotta F., Mainardi L., Migliavacca F. From medical images to three

dimensional CFD models of patient-specific stented coronary arteries. *Proceedings of the 12th International Symposium on Biomechanics in Vascular Biology and Cardiovascular Disease*, 4th-5th April 2017.

Migliori S., Chiastra C., Bologna M., Montin E., Dubini G., Aurigemma C., Fedele R., Burzotta F., Mainardi L., Migliavacca F. Reconstruction method of patient-specific coronary arteries with stent for CFD analyses. *Proceedings of the 23rd Congress of the European Society Biomechanics, ESB2017*, 2nd-5th July 2017.

Migliori S., Chiastra C., Bologna M., Montin E., Dubini G., Aurigemma C., Burzotta F., Mainardi L., Migliavacca F. Reconstruction of stented coronary artery for CFD analyses: from in-vitro to patient-specific models. *Proceedings of the VII Annual Meeting of the ESB Italian Chapter, ESB-ita2017*, 28nd-29th September 2017.

Montin E., Migliori S., Chiastra C., Credi C., Fedele R., Aurigemma C., Levi M., Burzotta F., Migliavacca F., Mainardi L. A method for coronary bifurcation reconstruction from angiographic images. *Proceedings of the 38th Annual International Conference of the IEEE Engineering in Medicine and Biology Society, EMBC'2016, p. 4165-4168.*, 14th-17th August 2016.

Migliori S., Chiastra C., Bologna M., Montin E., Dubini G., Aurigemma C., Fedele R., Burzotta F., Mainardi L., Migliavacca F. A robust OCT-based reconstruction method for coronary arteries. *Proceedings of the Frontier Biomechanical Challenges in Cardiovascular Physiopathology, ESB-ita 2016*, 8th-9th September 2016.

Migliori S., Chiastra C., Bologna M., Montin E., Dubini G., Aurigemma C., Fedele R., Burzotta F., Mainardi L., Migliavacca F. Stented coronary arteries: a semi-automatic segmentation method for OCT-based reconstruction. *Proceedings of the Virtual Physiological Human Conference, VPH2016*, 26th-28th September 2016.